Effect of Annealing Atmosphere on the GI Behaviour of a DP Steel

McMaster University

Inspiring Innovation and Discovery

Effect of Annealing Atmosphere on the Galvanizing Behaviour of a Dual Phase Steel

By

Rubaiyat Khondker

(M.Sc. in Metallurgical Engineering)

A Thesis

Submitted to the School of Graduate Studies

in Partial Fulfillment of the Requirements

for the Degree of

Master of Applied Science

McMaster University

MASTER OF APPLIED SCIENCE (2006) McMaster University

(Materials Science & Engineering) Hamilton, Ontario

TITLE Effect of Annealing Atmosphere on the Galvanizing Behaviour of a Dual Phase Steel

AUTHOR Rubaiyat Khondker.

B.Sc. in Metallurgical Engineering, (BUET, Dhaka, Bangladesh), 1991.

M.Sc. in Metallurgical Engineering, (BUET, Dhaka, Bangladesh), 1995.

SUPERVISOR Dr. Joseph R McDermid

NUMBER OF PAGES: xiv, 107

ABSTRACT

The selective surface oxidation of alloying elements such as Mn can cause dual phase (DP) steel wettability problems by liquid Zn during continuous galvanizing. It is well known that process parameters, such as the annealing atmosphere $\%H_2$ and dew point, can affect surface and subsurface oxidation. The purpose of this research was to study the effect of the annealing atmosphere to determine the optimum DP steel surface that would result in better reactive wetting by zinc. In particular, the evolution of the surface phases and structures during the continuous galvanizing annealing cycle were studied. It was shown that the internal / external oxidation behavior of the alloying elements of DP steel (e.g. Mn and Mo) at the surface and subsurface can be controlled by changing process parameters (dew point and H_2/N_2 ratio) and that some segregation of elements is unavoidable but can result in good reactive wetting by liquid galvanizing alloys. A transition from external to internal oxidation was observed when the oxidation potential (pH_2O/pH_2) of the annealing atmosphere was increased from 0.00844 to 0.03451. Despite the presence of 9-19 wt% Mn as MnO in the pre-dipped steel surface, the coatings exhibited good adhesion and a well developed Fe_2Al_5 inhibition layer at the coating / substrate interface for all experimental annealing atmospheres as a result of reactive wetting. This is attributed to aluminothermic reduction of manganese oxide by aluminum present in the liquid galvanizing alloy.

ACKNOWLEDGEMENT

The author wishes to thank Stelco Inc., the Natural Sciences and Engineering Research Council of Canada (NSERC) and the members of the McMaster Steel Research Centre for their financial support of this research through their funding of the Stelco/NSERC Industrial Research Chair in Steel Product Application. The author would also like to thank Mr. Jason Lavallée (galvanizing simulator), Mr. John Rodda, Mr. Doug Culley, Mr. Rob Lemon, Mr. Steve Koprich and Mr. Fred Pearson for their technical support, Dr. Li Sun (Dofasco Inc.) for her assistance with the XPS analysis and Dr. Carmen Andrei for her assistance with the HRTEM analysis. Author wishes to thank Dr. M.H. Kaye (RMC, Kingston, ON) for providing the results of thermodynamic calculations regarding Al activity in the Zn bath. Author wishes to thank all members of the research group, specifically, Dr. A.I.M. Mertens and Erika Bellhouse for their valuable comments and co-operation. Above all, the author wishes to express heartiest gratitude to his supervisor Dr. Joseph R. McDermid for his all kind of support, encouragement and direction to complete this research work.

TABLE OF CONTENTS

LIST OF FIGURES

Page No.

LIST OF TABLES

Page No.

1. Introduction

Dual Phase (DP) steels are members of the family of advanced high strength steels (AHSS) which have recently attracted auto industry for the manufacturing of lighter weight vehicles due to their excellent combination of strength and formability [1, 2]. DP steels are essentially a two phase microstructure which consists of a soft ferrite matrix and hard martensite. This microstructure enables DP steels to achieve the desired mechanical properties. The automotive industry is also demanding the contradictory requirements of lighter weight, more fuel efficient vehicles without sacrificing safety. DP steels can readily meet these demands. More importantly, DP steels are less expensive and could be processed in the existing industrial process windows only if the galvanizing problem were solved. Hot dip galvanizing (HDG) in a continuous galvanizing line (CGL) is amongst the cheapest and industrially viable corrosion protection system for DP steels.

DP steels require special alloying elements and processing routes to obtain the desired microstructure and mechanical properties. DP steels generally contain low carbon along with alloying element additions such as Mn and Mo to increase the hardenability and help to provide a high UTS to YS ratio [3, 4]. During annealing in the CGL, some of the alloying elements can selectively diffuse to the external surface to form oxides, which is of particular concern because the existing industrial CGL annealing atmosphere can not reduce MnO or other alloying element oxides (e.g., Al_2O_3 or SiO_2). At the same time, an oxide-free steel surface is required for reactive wetting by liquid Zn during galvanizing [5]. Any oxides that present on the steel surface could prevent reactive wetting, which is

of primary importance for the formation of a well developed Fe_2Al_5 inhibition layer at the coating / substrate surface to provide good coating adhesion.

In the present research work, the influence of the annealing atmosphere (i.e. pH_2O/pH_2 ratio) on the preferential surface oxidation of an industrial DP steel alloyed with 2 wt% Mn and 0.33 wt% Mo has been studied. It will be seen in this work that by changing the oxidation potential of the annealing atmosphere the surface enrichment of some alloying element oxides can be controlled but can not be completely avoided. The evolution of the steel surface at various annealing atmospheres at different stages of the thermal cycle has been studied and the relation between the evolved surfaces and reactive wetting has been established by means of galvanizing simulations.

2. Literature Review

This literature review consists of four sections. In the first section, the properties of DP steels will be discussed with an emphasis on their potential in the automobile industry. The reason behind the increased demand for DP steels are their relatively low cost and improved mechanical properties, which are suitable for producing lighter, more fuel efficient cars [1]. There is a common understanding in the literature that the most economical way to protect DP steels from corrosion is to galvanize (GI) the steel in a continuous galvanizing line (CGL). The present research work is directed towards understanding the process parameters related to the continuous galvanizing of DP steels. In the second section, the galvanizing (GI) process with special attention to the CGL, the bath chemistry of the CGL and the structure and properties of high quality coated steels will be discussed. Unfortunately, reactive elements added for increasing hardenability and improving mechanical properties in DP steels are susceptible to selective oxidization at the external surface during processing, which may deteriorate reactive wetting and the resultant coating properties. In the third section, the oxidation theories of metals and alloys with special attention to Carl Wagner's selective oxidation theory [6-8] will be discussed with the objective of finding a solution for the processing of oxide free DP steel surfaces. In the last section, the problems and probable solutions for galvanizing DP steels will be discussed. It can be seen from the work done in the past, that the internal selective oxidation of reactive elements by increasing the oxidation potential of the

annealing atmosphere may be a feasible solution to this problem. It was again anticipated from the literature that a certain amount of external oxidation will be unavoidable in industrial practice [9] and therefore the literature review will be focused on the reactive wetting [10,11] to explain the observation of good wetting despite the presence of oxides.

2.1 Dual Phase Steels

2.1.1 The Potential Uses of Dual Phase Steels in the Automotive Industry

Members of the AHSS family of steels include dual phase (DP), transformation induced plasticity (TRIP), complex phase (CP), and martensite (MART) steels. Among the members of AHSS, DP steels are the most exciting because they are relatively less expensive, easier to fabricate and are a very good absorber of energy. The use of galvanized (GI) and galvannealed (GA) coated DP steels have accelerated the replacement of High Strength Low Alloy (HSLA) steels in North America from 1999 onwards [12, 13]. Currently, all major North American steel companies are producing DP steels. The true prospects for DP steel can be imagined if one considers the next generation of automobiles. For example, the ULSAB-AVC (Advanced Vehicle Concepts) is one of the latest initiatives which offer an all steel solutions for safe, fuel efficient, environmentally responsible vehicles [2]. Compared to other competing materials, such as aluminum, magnesium or plastics and composites, DP steels can be processed using similar processes to mild steel. This is the added advantage beside the benefit of weight

saving [14]. Compared with the mild steels, for example, DP steels can be fabricated into much lighter and more versatile structures [15].

The demand for DP steels arises from their excellent combination of formability and strength compared to other steel grades which are shown in Figure 2.1 [2].

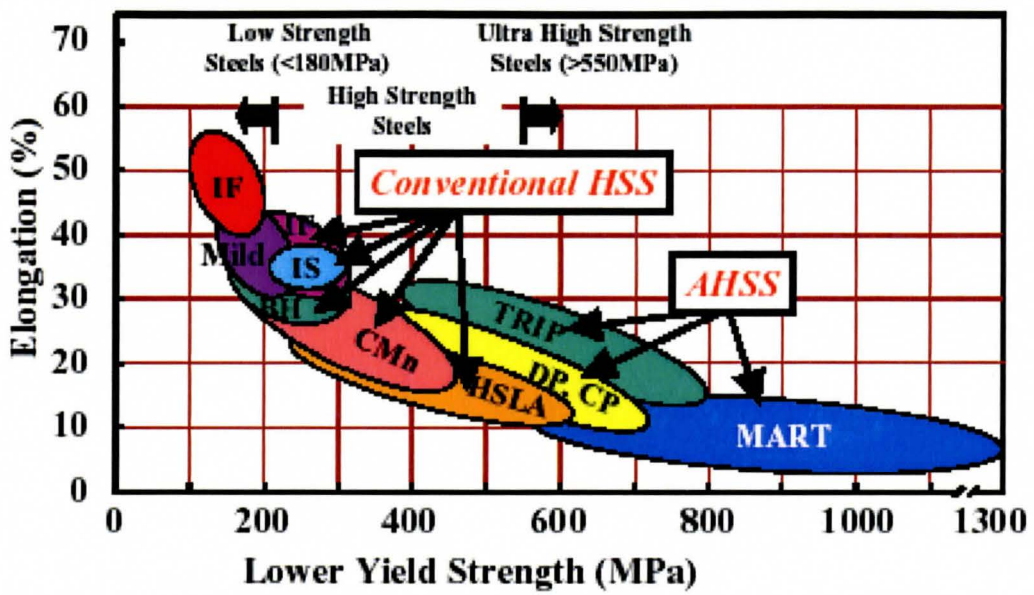

Figure 2.1: Elongation as a function of yield strength for various steel grades [2].

It is already established in the literature that DP steels possess a high UTS to YS ratio and do not exhibit any sharp yield point [2]. This kind of deformation behaviour is advantageous for forming operations as the fabrication of steels for automotive applications usually requires pressing operation and welding. A sharp yield point can cause phenomenon like stretcher strains. The strain associated with the formation of

martensite introduces free dislocations in the adjacent ferrite, thereby eliminating the sharp yield point [16, 17]. The mixture of hard martensite and soft ferrite also gives a better average strength without sacrificing formability [2].

2.1.2 Thermal Cycle and Alloying for the DP Microstructure

Typical DP steel microstructures are usually obtained by the annealing of a ferrite - pearlite steel in the intercritical temperature range followed by the appropriate rapid cooling to obtain martensite. Figure 2.2 shows a characteristic thermal cycle in a continuous line and the obtained DP microstructure [18]. The microstructure consists of ferrite and martensite with small fractions of other phases e.g. bainite and carbides depending on the annealing process parameters [18].

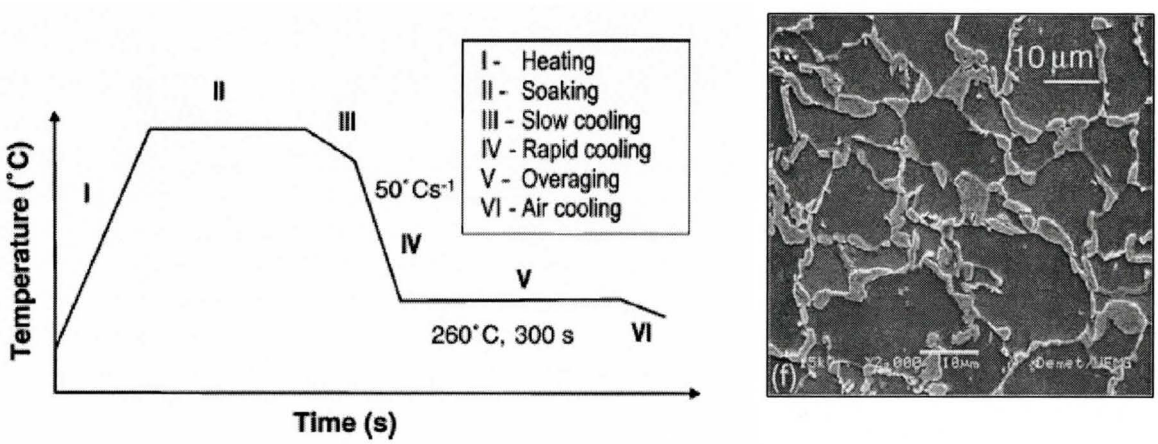

Figure 2.2: (a) Schematic diagram of the continuous annealing process (b) obtained DP steel microstructure [18]

The annealing temperature is controlled within the ferrite-austenite two phase regions in such a way that most of the room temperature ferrite phase remains in the microstructure while the resident pearlite is transformed to carbon rich austenite. When this steel is quenched at an appropriate rate from the annealing temperature, the austenite phase transforms into martensite to form the desired DP steel microstructure.

Alloying elements such as Mn and Mo are used in DP steels in order to control the hardenability. Their composition in the steel should be adjusted in such a way that for the cooling rates obtainable in the industrial lines, the intercritical austenite transforms to martensite upon cooling. To determine the chemistry and annealing condition of the DP steels applied to the automotive industry, various properties should be considered. Optimum strength to ductility ratio is the most important one amongst them. Good weldability and phosphatability should also be considered while designing these steels [3].

In general the highest strength-ductility balance is obtained by the two phase microstructure that consists of a small amount of carbon enriched martensite and fully ductile ferrite [3]. In DP steels, the carbon content is kept lower than 0.2% partly because higher amounts of carbon in steel deteriorate the welding properties [19]. Carbon is the most common alloying element that increases strength of steel and it is well known that martensite hardness increases with the increase in the carbon content. Lowering the carbon content increases the ductility of the steel but at the same time decreases the strength of the steel. So strengthening of ferrite by solute atoms is required [3]. Solid

solution hardening can be performed by the addition of Mn. In addition to high hardenability, Mo produces finely recrystallized grains [4]. Strengthening is also attained by precipitation hardening in steels containing Nb and V.

It is largely agreed in the literature that DP steels have the desired strength and formability that could provide thinner gauge steels for automotive application without sacrificing strength or crash worthiness. Thinner gauge steels require better corrosion protection to maintain structural strength and to meet consumer durability expectations. Corrosion protection can be done in several ways, amongst which continuous galvanizing is the most cost effective corrosion protection process. The following section will consist of a literature review of the continuous galvanizing line and its bath chemistry.

2.2 Continuous Galvanizing

2.2.1 The Continuous Galvanizing Process

Most sheet products are galvanized in Sendzimir-type process continuous galvanizing lines (CGL) [20]. The Sendzimir process combines continuous annealing with the zinc coating process. Thus, the furnace performs; two functions (1) recrystallization / intercritical annealing for mechanical properties and (2) hot gas de-oxidation of the surface via $FeO + H_2 = Fe + H_2O$, to provide a surface suitable for galvanizing. A schematic of a Sendzimir-type CGL line is shown in Figure 2.3 [5] which illustrates the basic continuous galvanizing process.

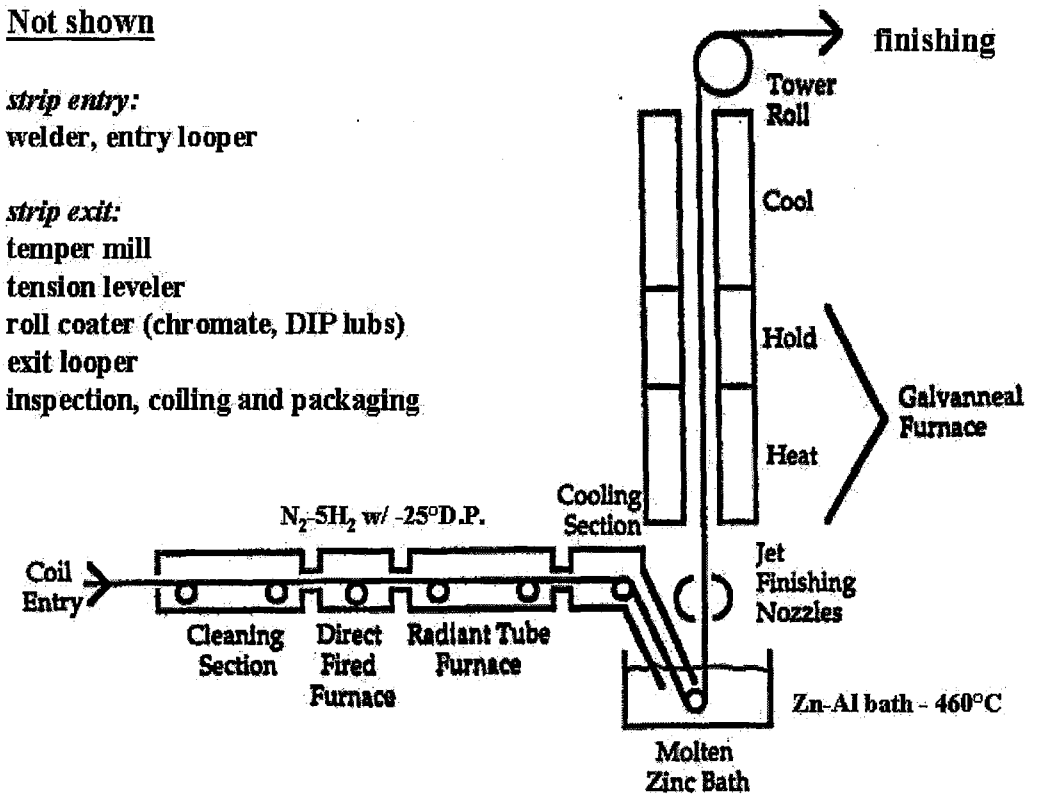

Figure 2.3: Schematic diagram of a typical Sendzimir type continuous hot dip galvanizing line [5].

Continuous hot-dip galvanizing lines generally consist of several sections. First of all, there is usually a coil entry welder capable of joining successive coils so that the process is continuous. The second section usually comprises a cleaning section to remove oils, dirt, rolling fines and loose oxides. The third section consists of an annealing furnace to anneal the full-hard strip and impart the desired mechanical properties and microstructure to the steel. In the annealing furnace, the strip is maintained under a

reducing gas atmosphere to reduce any oxides on the steel surface. The gas atmosphere is usually composed of 5-20 vol. % hydrogen and nitrogen. The gas atmosphere is also controlled by the dew point which is a measure of the water vapour content (really, p_{O_2}) of the atmosphere at temperature.

Commercial CGL furnaces commonly operate at a dew point of -30 °C and 5% H_2 but the operation range can be varied between -30 °C to + 10 °C dew point and 5 to 20 vol. % H_2. This oxide reduction step is very important to obtain complete wetting of the steel surface by the liquid Zn alloy. The exit end of the furnace is submerged in a molten Zn coating bath by a "snout" to prevent any re-oxidation of the annealed sheet. In the fourth section, there is a molten Zn coating bath. The strip passes around a submerged or sink roll and then exits the bath in the vertical direction. The bath chemistry, bath temperature and dipping time in the bath will determine the microstructure of the coated products. At the exit point of the bath, a set of gas knives (usually high pressure air or nitrogen) wipe off any excess molten metal and thus control the thickness of the zinc coating. The coating is then cooled to allow the metal to freeze on the steel surface. Subsequent sections of a typical CGL consists of a temper mill for surface finish and yield point elongation control, a tension leveler to flatten the strip and a treatment section to prevent storage stains. Finally there should be a recoiler to rewind the finished coil of steel.

2.2.2 Role of Al in the Zinc Bath

The invention of Al addition in Zn bath has enabled continuous hot dip galvanizing to be economically viable compared to other processes. Al additions to the zinc bath were discovered 50 years ago [5] and since then the addition of Al to the CGL bath is a routine practice. The addition of Al to the Zn bath is not intended to enhance the corrosion properties of the coating but to enhance coating adhesion, which is important for formability [21].

When the steel strip enters the molten zinc bath (without Al) a series of brittle Fe-Zn intermetallic compounds are formed at the interface between steel and zinc, as per the schematic diagram of Fe-Zn intermetallics produced in a galvanizing bath without Al [22] shown in Figure 2.4(a). This layer lacks ductility and will fracture and flake off at the substrate / coating interface during forming. Additions of Al to the CGL bath temporarily suppress the formation of the Fe-Zn phases by forming Fe_2Al_5 at the interface. A schematic diagram of Fe-Zn intermetallics phase layer formation with the 0.20 wt% Al in the bath [23] is shown in Figure 2.4 (b). In both cases, t_0 corresponds to zero time, and development proceeds with time such that $t_1<t_2<t_3<t_4$. It is seen from Figure 2.4 (b) that this Fe_2Al_5 layer inhibits or suppresses the formation of Fe-Zn intermetallics, and it is commonly referred as the "inhibition layer" and allows the production of pure Zn coatings [24].

This delayed reaction makes the final coating thin and the microstructure is composed of thin ternary alloy layer of Al, Fe and Zn at the interface and pure zinc on the

outside. It should be mentioned that this inhibition layer is not exactly composed of Fe_2Al_5, but also incorporate Zn in its structure and can be seen in the phase diagram as $Fe_2Al_{5-x}Zn_x$. [25, 26]

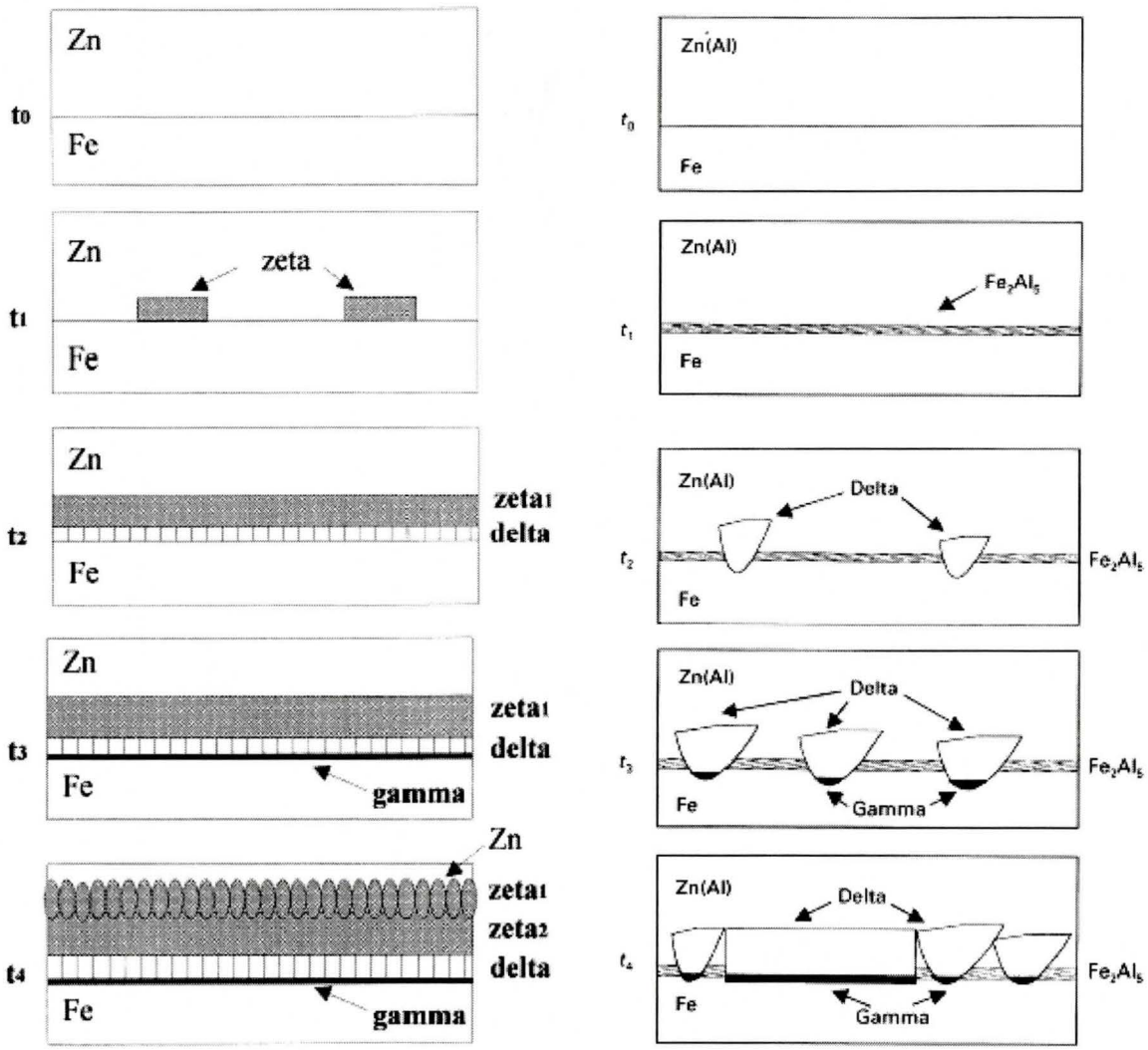

Figure 2.4: (a) A schematic representation of Fe-Zn phase layer formation in a 0.00 wt% Al-Zn galvanizing bath [22]. (b) A schematic representation of Fe-Zn phase layer formation in a 0.20 wt% Al-Zn galvanizing bath [23].

Thermodynamically, Al has a greater affinity for iron than zinc and immediately (i.e., <1 sec) [24, 27] forms a thin (100-250 nm) Fe_2Al_5 layer after the strip enters the bath. However, this effect is always temporary and continuing exposure of the Zn / Fe_2Al_5 / Fe coupled with high temperatures and long times will result in the destruction of the Fe_2Al_5 layer and the formation of Fe-Zn intermetallics. This phenomenon is commonly referred to as "inhibition breakdown" and is controlled by the diffusion of Zn into the substrate through the Fe_2Al_5 inhibition layer.

2.2.3 Structure and Properties of High Quality Galvanizing Coatings

Coating properties are largely dependent on their microstructure. To predict and control the microstructure of galvanized coating, it is essential to understand the liquid zinc / steel substrate interfacial reactions. The inhibition layer is required to be adherent and continuous in order to form a good bond with the substrate. The Fe_2Al_5 layer is a consequence of reactive wetting. In other words, a fully–formed Fe_2Al_5 layer indicates that reactive wetting has occurred. The characteristic of the inhibition layer depends mostly of the process parameters and the steel surface composition and its thickness varies between 60 nm to roughly 300 nm [5].

Tang [28] reported that Al enrichment in the interface is a function of the bath Al content, the bath temperature, the strip entry temperature, the strip thickness, the immersion time and the coating weight. For a typical galvanizing operation, the bath Al

content is kept below 0.3%Al and the bath temperature is generally 460 °C. In the CGL, the strip entry temperature and dipping time also depends on the line speed. Typical dipping time ranges between 4-8 seconds for line speeds in excess of 175 m/min [5].

The morphology of the inhibition layer also depends on bath Al content and dipping time. Baril et al. [29] observed two types of inhibition layer morphology when a commercial ultra low carbon steel was dipped for 3.5 seconds into a Zn bath containing 0.18 wt% Al. Figure 2.5 (a) shows small and equiaxed Fe_2Al_5 crystals (average size of 90 nm) and Figure 2.5 (b) shows coarse and elongated Fe_2Al_5 crystals (average size ranges from 100 to 1000 nm). The ratio between Fe / Al mass content in the inhibition layer is a measure of inhibition layer formation which is constant (0.828) for bath Al contents above 0.15 wt % in a 1-6 second dipping time range [30]. Interruption of the inhibition layer formation or breakdown of the inhibition layer deteriorates the coating quality and formability.

However, with the addition of Al, the interfacial reactions are more complex and according to Guttmann, [24] the complexities are related to three factors: first, several reactions take place at the interface, second, the speed of the reactions are very fast and in some cases, happen in less than a second and third, the transformation front is often unstable and is not governed by simple equilibrium thermodynamics. In the interface study, the Fe-Zn-Al ternary phase diagram and the bath chemistry is required to understand the applicable equilibrium. Kaye et al. [31] modeled (Figure 2.6) the Zn rich corner of Zn-Fe-Al ternary phase diagram where it can be seen that when the Al content

is more than 0.14 wt %, the phase in equilibrium with the liquid is the $Fe_2Al_5Zn_x$ (η) phase. It also shows that the solubility of Fe is dependent on bath Al content.

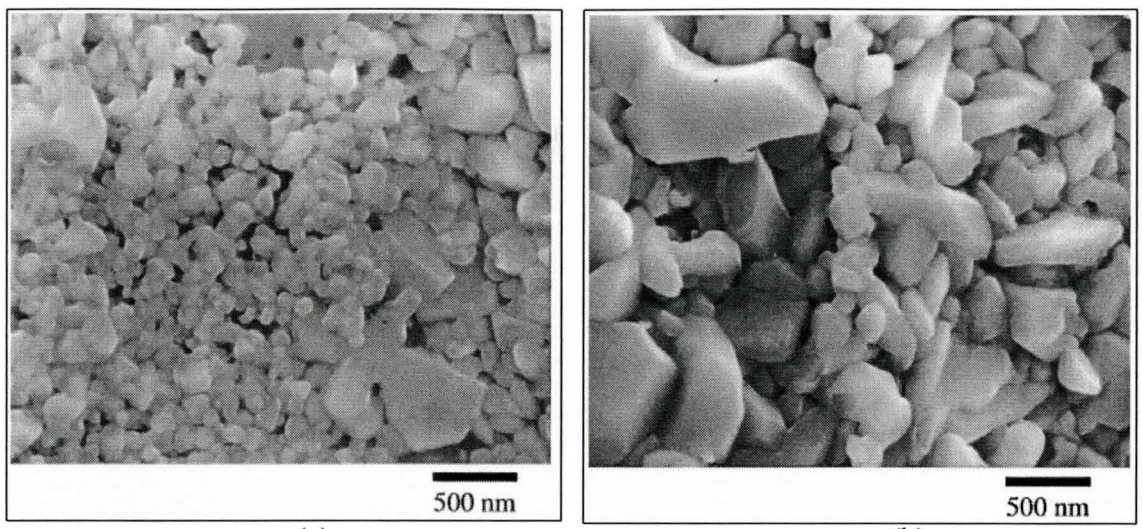

(a) (b)

Figure 2.5: Morphology of the Al-rich inhibition layer observed in a Zn bath with 0.18 wt% Al and immersion time of 3.5 s: (a) small equiaxed crystal (b) coarse elongated crystal [29]

The thermodynamic modelling of molten Zn rich corner of Zn-Al-Fe ternary was expressed by activity coefficient expressions for each solute component and are shown in equations (2.1) and (2.2) [31]:

$$\log[\gamma_{Al}]_{liq} \cong \left(\frac{2053.8}{T} - 2.074\right) + \left(\frac{-10828.8}{T} + 13.854\right)X_{Al} + \left(\frac{16122}{T} - 1.395\right)X_{Fe} \quad (2.1)$$

$$\log[\gamma_{Fe}]_{liq} \cong \left(\frac{-1628.36}{T} + 3.008\right) + \left(\frac{5266.6}{T} - 7.377\right)X_{Fe} + \left(\frac{16122}{T} - 1.395\right)X_{Al} \quad (2.2)$$

Where, γ_i are the activity coefficients of the solute species i, T is the absolute temperature (K) and X_i are the mole fraction of the solute species. The slope of the iso-activity lines in Figure 2.6 shows the effect of the Fe–Al interactions along with Zn bath temperature which is presented by the final term of the equations (2.1) and (2.2).

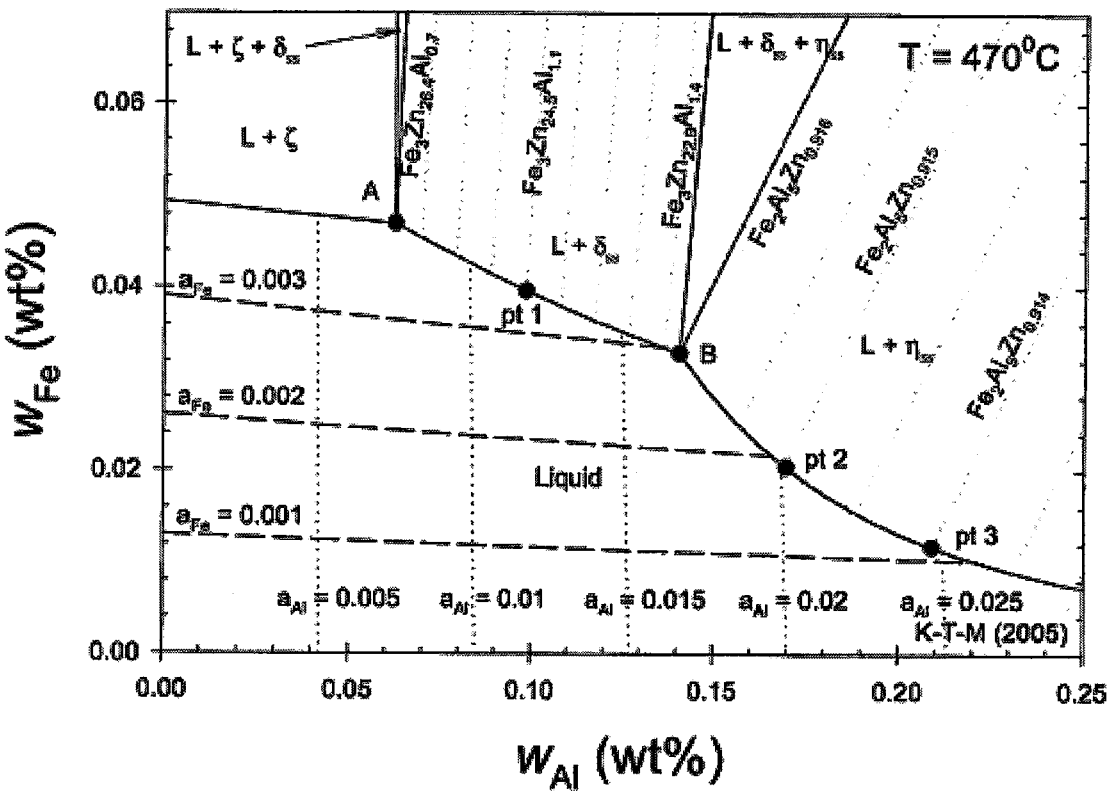

Figure 2.6: metastable Zn-rich Zn-Al-Fe phase diagrams [31].

It is understood from the above discussions that for better wetting it is essential to form a complete and uniform inhibition layer. Selective oxidation at the external surface during annealing may prohibit reactive wetting and disrupt the formation of the inhibition layer. In the following section the oxidation theories of metal and alloys will be reviewed with the objective of better understanding and controlling the selective oxidation of the reactive elements.

2.3 Oxidation of Metal and Alloys

2.3.1 External Oxidation of Simple Binary Alloys-Wagner's Law

Selective oxidation is a process in which a less noble element in an alloy is selectively oxidized at the outer layer surface and can provide protection from further oxidation. If there is a large difference in the stabilities of the oxides of the component elements in an alloy and if the alloy contains a sufficient amount of less noble elements then complete coverage of the surface by a protective layer may occur. The temperature and the partial pressure of oxygen also have a significant influence on selective oxidation. It is important to mention that most of the research work was done to find a suitable alloy composition or process parameter that would allow external selective oxidation for the better protection of the substrate steel. However, for galvanizing, the aim is to remove the external surface oxide and promote reactive wetting. Conditions which promote external selective oxidation should be avoided. In the following discussion, DP steels will be considered to be dilute Fe-Mn alloys where Mn is the solute and is less noble than Fe.

The selective oxidation behaviour of Mn processed under different annealing atmospheres will be discussed with reference to Wagner's oxidation model [6-8].

Kofstad [32] described Wagner's mathematical expression [6-8] for a binary A-B alloys (B is less noble) and showed that under any set of conditions, selective oxidation of B will take place only when the concentration of B in the alloy is above a critical concentration. Assuming a pore free compact scale, Wagner described three possible cases of oxidation as shown in Figure 2.7.

In case 1, i.e. at low concentrations of B, only A oxide will form and B will diffuse away from the alloy - oxide interface to the bulk alloy (Figure 2.7a.). If oxidation continues then the alloy will continue to enrich with B and after attaining a certain critical enrichment, B oxide can form. At this stage, the concentration of B at the interface will be in equilibrium with the three phase mixture of the alloy, A oxide and B oxide. In the second case, when the alloy contains a sufficient concentration of B, only B oxide is formed and A will diffuse away from the alloy - oxide interface into the alloy (Figure 2.7b). Oxide A will form only when the concentration of A of the interface reaches the critical concentration that corresponds to three phase equilibrium of the mixture of the alloy + A oxide + B oxide. In the third case, when the concentration of B is in between N'_B and N''_B (i.e., more concentration of B in the alloy than case 1 but less concentration than case 2), both the oxides will form simultaneously (Figure. 2.7c).

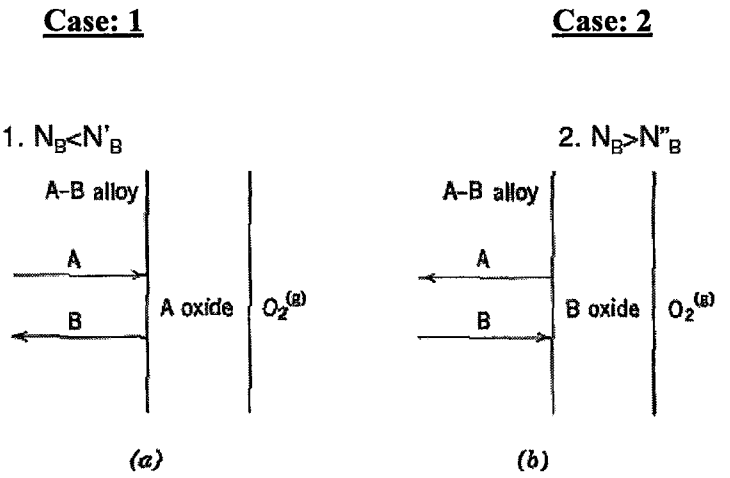

Case: 3 Concentration of B ranging in between N'_B and N''_B

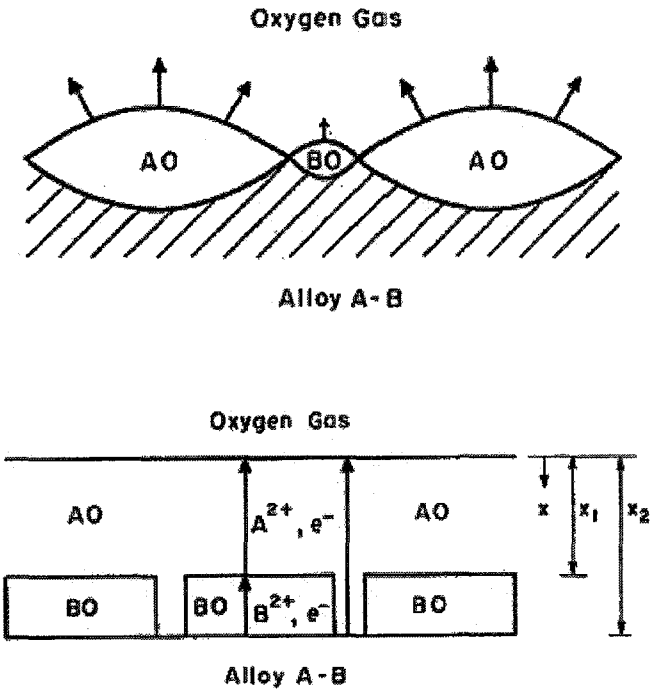

Figure 2.7: Diffusion process during oxidation of A-B alloys (a) Exclusive A oxide formation (bulk alloy concentration N'_B) [32], (b) selective oxidation of B oxide (bulk alloy concentration N''_B) [32] and (c) simultaneous formation of A oxide and B oxide [7]. N_B is the equilibrium concentration of B in the three phase mixture (alloy + A oxide + B oxide).

In this analysis, Wagner [7] assumed that diffusion was normal and parallel to the surface. Other assumptions in the analysis were that only cations are the migrating species and AO grows faster than BO and predicted that after some time AO oxide would bury BO. Oxide B had no direct contact with oxygen but could grow depending upon stability differences between AO and BO.

2.3.2 Internal Oxidation

Internal oxidation is the process by which oxygen dissolves on the surface and then diffuses into the alloy and causes subsurface precipitation of the alloying elements [7]. The essential conditions for internal oxidation have been described by Rapp [33].

- The free energy of formation of the solute oxide must be more negative than solvent oxide.
- The solvent must exhibit solubility and diffusivity to oxygen.
- The critical solute concentration must be lower than that required for external oxidation.
- Surface oxide layers must not prevent oxygen diffusion to the substrate.

Both internal and external oxidation is diffusion controlled process. After exceeding a certain level of solute content in the alloy, the occurrence of internal oxidation of the solute is replaced by the formation of external oxidation of the solute

[33]. Rapp used the Wagner oxidation model to find transition compositions for internal to external oxidation in his experimental Ag-In alloys. Rapp [33] proposed schematic concentration profile for the internal oxidation of A-B alloy (Figure 2.8) based on the diffusion behavior of oxygen.

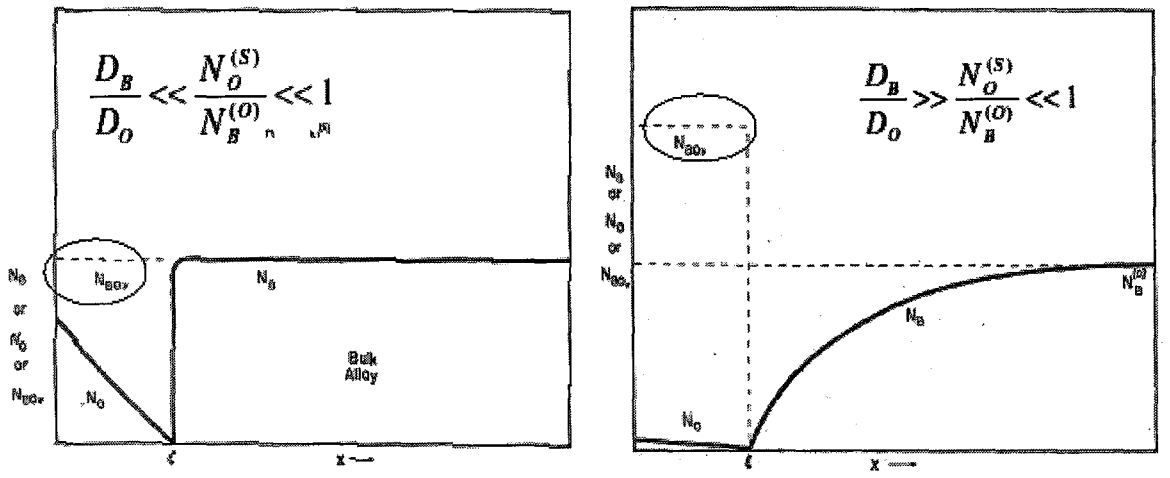

Figure 2.8: Schematic concentration profiles for internal oxidation when (a) Movement of the oxidation front is based on the diffusion of oxygen in the base metal only and (b) Outward diffusion of the solute as well as inward diffusion of the oxygen is important in determining the oxidation kinetics [33].

The equation for internal oxide thickness, ξ, is given by [33]

$$\xi = \left[\frac{2N_O^{(S)} D_O t}{\upsilon N_B^{(O)}}\right]^{1/2} \qquad (2.3)$$

and the criterion of external oxidation is given by [33]

$$N_B^{(O)} > \frac{\pi g^*}{2\upsilon} N_{(O)}^{(S)} \frac{D_O V_m}{D_B V_{ox}} \qquad (2.4)$$

Where, D_O = diffusivity of oxygen in the base metal,

D_B = diffusivity of solute B in the base metal,

N_O = mole fraction of oxygen in the base metal,

$N_O^{(S)}$ = mole fraction of oxygen at the external surface,

$N_B^{(O)}$ = mole fraction of B in the bulk alloy,

N_B = mole fraction of B arriving at the precipitation front from the bulk alloy,

υ = the number of oxygen ions per B ion in the oxide BO_υ.

Where the enrichment factor, $g^* = f\frac{V_{OX}}{V_M}$ and for Ag-In alloy its value is 0.3 [33].

Equation (2.3) describes the change in internal oxidation penetration thickness with changing atmosphere and equation (2.4) describes how the changing exposure could affect the bulk concentration of the solute required to produce external oxidation. Favourable conditions for the transition to external oxidation mentioned by Birks and Meier [34] are:

(a) decreasing the inward flux of oxygen $N_O^{(S)}$ i.e. lowering the value of pO_2

(b) increasing the outward flux of B (e.g., increase D_B by short circuit diffusion through grain boundaries or through dislocation cores)

Rapp [33] found (which is shown in Figure 2.9) that the critical solute content of Indium in a Ag-In alloy to shift the oxidation mode from internal to external was 0.15 when the pressure of oxygen is 1 atmosphere. Rapp showed that calculated critical bulk alloy concentration decreased from 0.15 at 1 atmosphere to 0.11 at 1 Torr and 0.05 at 10^{-2} Torr and 0.02 at 10^{-4} Torr oxygen pressure. Clearly the oxygen pressure has an effect on the critical solute content that is required for external solute oxidation.

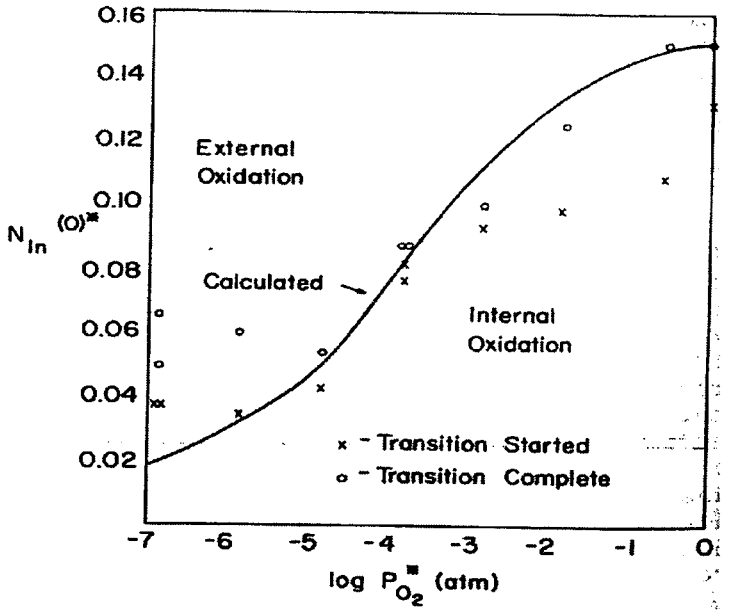

Figure 2.9: Transition from internal to external oxidation for Ag-In alloys at 550 °C [33].

From the above discussion of DP steels, the CGL and Wagner's oxidation theory it is understood that some of the alloying elements used in DP steels can have oxides which are more stable (less noble) than iron oxides and since the conventional CGL annealing atmospheres are not reducing to them, they preferentially oxidize at the surface. The amount, shape and morphology of these oxides have an effect on DP steel

wetting. The following section will review the literature about the effects of oxides on wetting and explore the possible solution of galvanizing DP steels by changing the oxygen potential of the annealing atmosphere.

2.4 Galvanizing of DP Steel

The galvanizing process for coating steels is a very old process and the principles of galvanizing have remained unchanged for the last 200 years [5]. However, because of the demand in the automotive and construction industries, recently a considerable amount of research has been carried out on all aspects of the galvanizing processes [5]. In the galvanizing operation, the zinc coating on the steel surface acts as a barrier between the iron and the environment. In addition to providing a physical barrier, zinc acts as a sacrificial anode and corrodes preferentially to protect the steel substrate. The essential requirement of good galvanizing is an oxide free steel surface. However, it is extremely difficult to obtain an oxide free DP steel surface. As mentioned earlier, DP steel requires alloying elements and special processing to obtain its characteristics properties. During processing, these alloying elements preferentially oxidize at the surface, which causes dewetting of the steel by zinc. This problem is inherent for DP steel and earlier it was believed that due to this preferential oxidation of the alloying elements, new grades of high strength steels would not be suitable for galvanizing. But recent advancements in galvanizing technology are promising enough to overcome this problem.

The selective oxidation behaviour of each element is different and depends on several factors. The most important among them are the amount and kind of alloying elements in the steels and the processing conditions. It is very important to select the proper DP steel alloy composition which requires subsequent galvanizing.

2.4.1 Selective Oxidation of Alloying Elements in DP Steel

In the above text, the purposes of the alloying elements in commonly found DP steels were reviewed. The most commonly used alloying elements in DP steels are Mn, Mo, Nb and Ti. The relative stabilities of the oxides of these alloying elements are shown in Table 2.1 [35].

Table 2.1: Oxygen affinity of common alloying elements for DP steel [35], '+' denotes the atmosphere is reducing and '-' denotes the atmosphere is oxidizing to the element.

Element	**Free Energy of Formation at 800°C (kJ/mol O_2)**	**Typical content of AHSS %**	**Reduction Atmosphere 5-8% H_2, N_2, Dew point -30°C, 800°C**
Ti	-720 (TiO_2)	Up to 0.10	_
Mn	-610 (MnO)	0.5-2	_
Mo	-370 (MoO_2)	Up to 0.30	+
Fe	-375 (FeO)	-	+

Table 2.1 shows that many of the alloying elements oxides are more stable than iron oxide at the peak annealing temperature of 800 °C in a typical CGL atmosphere. It also shows that a normal industrial CGL annealing atmosphere is reducing to iron but the same atmosphere is oxidizing to Mn. It is observed from Table 2.1 that there exists small difference between the thermodynamic free energies of formation of FeO and MoO_2. This is the reason that Mo does not internally oxidize in a dilute Fe-Mo alloy [36].

Olejford [9] showed (Figure: 2.10) the equilibrium partial pressure of water vapour for the reduction of iron, manganese and vanadium oxides in a 15% H_2-N_2 atmosphere from which it can be deduced that FeO / Fe_3O_4 will be reduced above 150 °C at a dew point -20 to -30 °C, while the other alloying elements (V and Mn) will be oxidizing over the entire temperature range [5].

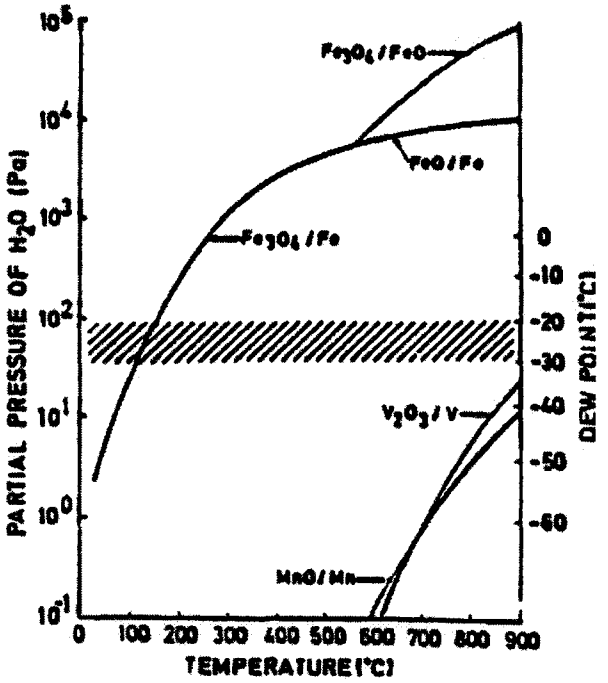

Figure 2.10: Equilibrium partial pressure of water pH_2O for reactions of the type:

$$\frac{x}{y}M + H_2O = y^{-1}M_xO_y + H_2$$

M is the cation forming element. The shaded area in the figure represents the range of temperature and dew point investigated [9].

By increasing the H_2 content in the N_2-H_2 atmosphere it is possible to make the atmosphere more reducing but it will be insufficient to reduce Mn oxides at the above dew points. Figure 2.10 indicates that MnO can be reduced using a -50 °C dew point but this dew point is not commercially viable. It is clear that for steels contains elements such as Mn or V; it is industrially difficult to have an atmosphere that is reducing to all alloying elements. When segregated to the steel surface Mn will be preferentially oxidized and thus can lead to bare spots [37]. It is reported that P and Mo do not create wetting problem and no oxide forms in the case of Mo [10] which is indicated in the Table 2.1.

2.4.2 Effect of Surface Oxides on DP Steel Wetting

The influence of alloying elements on the surface state has been studied in various conditions and steel grades by many researchers [38, 39, 40, 41]. The amount of external oxidation has thus been shown to depend on the affinity for oxygen, concentration and diffusion coefficient of the alloying elements considered. More importantly, the galvanizing behaviour can be directly related to the amount of external oxidation and the surface oxide morphology [42, 43]. The amount, uniformity, nature, distribution and morphology all have different effects on reactive wetting. DP steel is sensitive steel and the intense external selective oxidation of manganese disrupts the desired Fe-Al reactions in the liquid zinc bath and can results in bare areas [44].

Not only does the oxides chemistry create bare spots but also the distribution and continuous nature of the oxides creates wetting problems. Drillet et al. [45] argued that the continuous layer is more problematic than sporadic nodules of oxides. The chemical nature and distribution of oxides influences the wettability of the steel surfaces [46]. For example, despite the presence of some MnO_2 particles, CMnP TRIP steel, which is compositionally close to DP steels, showed excellent coatability [46].

2.4.3 Promoting Internal Oxidation by Increasing Dew point

There are two ways to overcome this wetting problem situation. Firstly, to alter elements which are more susceptible to external oxidation [10] or secondly, changing the oxidation potential of the annealing atmosphere so that reactive elements are obstructed to appear at the surface. In this present research, the steel composition is fixed so it is required to think about the controlling process atmosphere. According to Bode et al. [10], it is possible to exert a strong influence on the surface enrichments by modifying the annealing conditions. Selective oxidation goes from external to internal in nature at higher dew point i.e., corresponding to a higher level of moisture in the gas [10]. The authors also concluded that better galvanizing result is expected through greater internal oxidation [10]. Figure 2.11 shows less Cr accumulation at the surface at higher dew point.

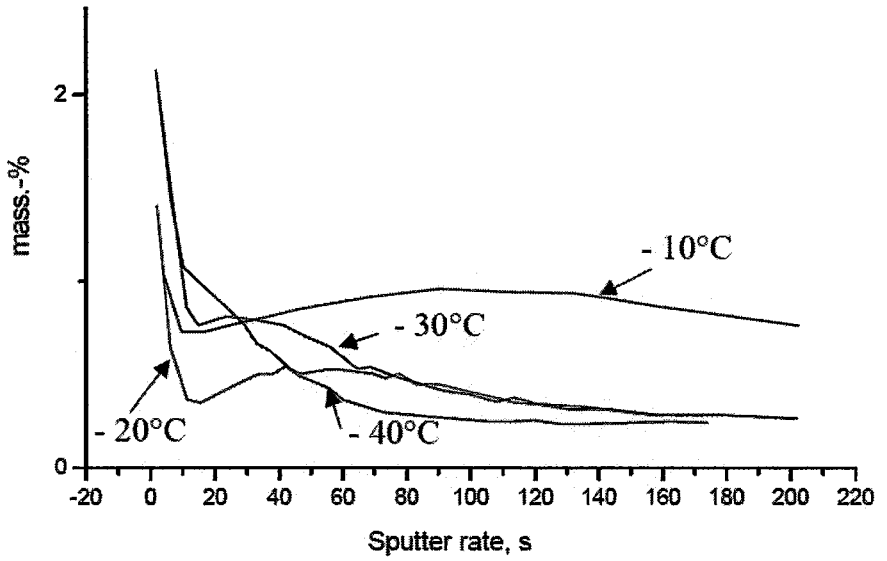

Figure 2.11: Effect of dew point on the Cr accumulation at steel surface [10].

Besides increasing dew point, three are three other reported techniques that could be beneficial for galvanizing; but the basic object of all these techniques are the same i.e., favours internal oxidation of reactive elements and make external surface clean. These are (1) Oxidation and reduction technique [38], (2) Oxidation-maturation-reduction technique [44] and (3) Annealing in a reactive atmosphere (CO, H_2+N_2) [47]. In the oxidation-reduction technique [38], emphasis is given to increase oxidation potential by increasing dew point at the initial stage of the annealing cycle. So that reactive elements are blocked to appear at the surface by iron oxide and in the later stage of annealing, surface iron oxides are reduced. Eynde et al. [44] proposed oxidation-maturation-reduction technique. It consists in pre-oxidizing the strip in the pre-heating zone of the

line, before an intercritical soaking in a hydrogen-free nitrogen atmosphere. Under such conditions, iron oxide is thermodynamically stable, thus preserving the thin iron oxide layer. The atmosphere is switched from oxidizing to reducing during rapid cooling, to remove all residual traces of iron oxide. Black et al. [47] used ($CO+H_2+N_2$ or $NH_3+H_2+N_2$) annealing atmosphere for modifying the chemical composition of the steel surface and thus provided an additional tool for improving wetting condition. The idea is that similar to carburizing or nitriding process. Here C or N penetrate to the surface and prevents Si or Mn to reach at the surface.

2.4.4 Risk of Manganese Oxide Formation during CGL Processing

It is clear from the literature that Mn is a key element for DP steel strengthening. The strengthening of DP steels can be "tuned" for different strength levels and processing methods. The future of higher strength DP steel in the automobile industry partially depends on the ability of higher %Mn steels to be continuously galvanized. That is why the selective oxidation behaviour of Mn in DP steel deserves special attention. There is some risk of manganese oxide formation during continuous galvanizing (CGL) and this issue will be discussed in this section.

Some controversy has arisen surrounding the question of how much Mn in steels is suitable for galvanizing. The 'suitability of Mn' question arises from the selective oxidation of Mn. Zheng and Bensinger [48] have found bare spots (unwetted surface) in

IF steels having 1.62 wt% Mn, from which the authors argued that the composition is not suitable for galvanizing. Yoon and Jang [49] recommended that Mn level should not exceed 1.5 wt% for the steels required galvanizing. Common industrial wisdom also supports the idea that steels with a Mn content greater than 1.5 wt %, are not suitable for galvanizing [1].

To pursue the study of Mn diffusion in steel, there arises another problem and that is from the similarities between Mn and Fe atoms. Similarities between Fe and Mn atoms and those between the oxides (FeO and MnO) are reported by Shi [50]. Preferential growth of one oxide over the others depends on the difference in their intrinsic growth rates and Shi [50] argued that since the growth rate of MnO does not differ greatly from that of FeO, internal oxidation may not be seen in dilute Fe-Mn alloy. Contrary to this, the oxidation-reduction method was reported successful in galvanizing a high Si-Mn-P-Ti containing steel [38] which implies that internal oxidation of Mn is possible. Several authors [51, 52] reported different enrichment behaviour of individual alloying elements that includes Mn variation with chemical composition and other alloys present in the steel. All those factors create confusion about the segregation of Mn in DP steels. There is a common agreement in the literature that a certain amount of manganese oxide is unavoidable at the external surface. However, there is a significant disagreement concerning the role of these oxides in the Zn bath. These disagreements are in terms of the amount and the reactive nature of these oxides in the Zn bath to provide better wetting.

2.5 Reactive Wetting

Several authors have reported [10, 11, 53, 54] that despite the presence of oxides wetting can be possible by means of reactive wetting. Basically all the above mentioned authors argued that in contrast to the thermodynamic equilibrium nature of wetting between inert interfaces (such as water on gold) the covering of steel surfaces with liquid zinc is a complex reactive wetting system. Bode et al. [10] worked with different grades of DP and TRIP steel containing 1.42 to 1.50 wt% Mn and after annealing the steel, the surfaces were enriched with 10-45 wt% Mn. The presence of Mn at the surface must be in the form of oxides under the experimental conditions used. The ways these oxides would behave in the Zn bath is of great interest in the present research area. According to the Bode et al [10], in DP steel, enrichments of Mn up to 17 wt% at the surface was able to produce very good galvanizing. Frenznick et al. [11] showed a very similar transition from poor wetting to wetting for silicon and manganese oxides. According to the Frenznick et al. [11], the presence of manganese oxide appears disadvantageous for wetting.

If the steel surface is enriched with a significant amount of oxides and yet the steel is able to be wet by zinc then this would imply that some dynamic wetting mechanism between the substrate steel and the Zn bath exist and can be measured by the Welhelmy plate method [54]. The oxidized steel surface when entering the Zn bath, the initial contact angle is usually large because of the surface oxides resist spreading. But if deoxidation of the surface occurs due to chemical reaction in the bath then the dynamic

wetting angle, θ, drops, and high spreading rates are achieved. Asthana et al. [53] argued that basically, three types of interactions can promote wettability in the high-temperature solid-liquid systems. Those are dissociation of surface oxides in liquid metal (oxide scavenging), chemical dissolution of the solid in the melt and formation of a wettable interfacial compound.

2.6 Objective

In the present research, Dual phase 600 steels have been studied to observe the effect of various annealing atmospheres on the segregation behavior of alloying elements as a function of time and temperature. Variations in the annealing atmosphere will be made by changing the dew point and hydrogen content of the process gas. The evolved surface will then be studied with respect to the reactive wetting in the molten Zn-Al-Fe galvanizing bath by studying the interfacial reactions during simulated galvanizing trials. The segregation of the solutes present in the DP 600 steel will be analyzed with reference to the Wagner oxidation kinetics model. Evolution of the surface chemistry and structure during the annealing cycle will be analyzed by interrupting the annealing cycle and gas quenching the sample. The mode of external / internal oxidation will be determined using depth profiling by glow discharge optical emission spectrometry (GDOES). The oxidation state of elements at the external surface before dipping in the zinc bath will be analyzed using X-ray photoelectron spectroscopy (XPS) technique. An analysis of the structure and chemistry of the surfaces and galvanizing interfacial will be accomplished through scanning and transmission electron microscopy. Reactive wetting during the

galvanizing processes will be assessed by comparing the substrate surface before and after dipping the samples into the zinc bath. The coating thickness, adhesion behaviour, coating uniformity, and population of bare spots present on the coatings will be analyzed to determine the coating quality. The results from this present research will provide useful information about the wetting behavior of DP 600 steel during the continuous galvanizing process and will assist in establishing suitable process parameters for the galvanizing DP steels via the continuous galvanizing process.

3. Experimental Procedure

The experimental chapter consists of three sections. In the first section, the as received DP 600 steel has been characterized in terms of chemistry, surface microstructure and phase diagram. The second section describes the galvanizing simulation operation; the McMaster galvanizing simulator, sample geometry and details concerning the process control of the atmosphere has been covered in this section. The final section describes the sample characterization techniques and instruments used in this research.

3.1 Experimental Dual Phase 600 steel

3.1.1 Chemistry of As Received Experimental Steel

The dual phase steel used for the present research work was supplied by Stelco Inc. (Hamilton, ON, Canada) in the form of cold rolled sheet of 1.57mm thickness. The composition of the experimental dual phase steel is shown in the Table 3.1. The table indicates that the major alloying elements in this steel are approximately 1.97% Mn, 0.07%C and 0.33% Mo. It has been indicated by several authors that Mn increases the strength of the dual phase steel and this is reflected in the high Mn content of the experimental steel. Mo was added to the experimental steel to increase hardenability and grain refinement [4]. The combination of the low carbon content, grain refinement, and precipitation hardening are reported to provide a high yield ratio in the products [3, 55].

Table 3.1 Composition (wt %) of the as received DP 600 steel.

Material	C	Mn	P	S	Si	Cu	Ni	Cr	Mo	V	Nb	Ti	N	Other
DP600	**0.07**	**1.97**	0.012	0.004	0.01	0.026	0.02	0.021	**0.33**	0.001	0.001	0.002	0.007	0.037

3.1.2 Microstructure of the As Received DP 600 Steel

X-ray spot analysis was carried out on the surface of the as received samples. The Figure 3.1 shows a SEM micrograph of a typical area of the sample surface. On the micrograph the black arrow indicates the area where the spot analysis was carried out.

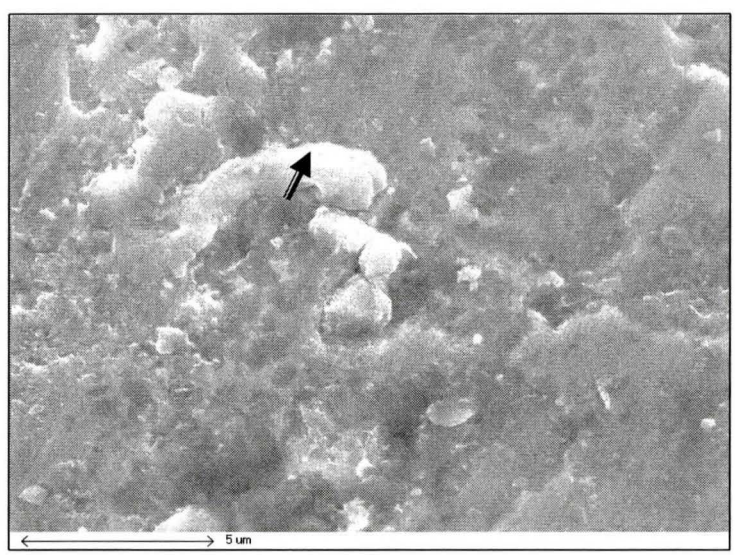

Figure 3.1: SEM micrograph of the surface of the as received sample.

The Table 3.2 lists the results of the spot analysis, which indicates the surface is significantly oxidized and contains contaminants such as chlorine. Figure 3.1 also indicates the rough nature of the sheet.

Table 3.2 EDS analysis of the as received sample.

Element	O	Cl	Mn	Fe	Total
Wt%	65.25	0.78	0.71	33.51	100.00

The sample was then sectioned, polished, etched and examined in cross-section using light optical microscopy. Figure 3.2 shows a micrograph of the polished sample. The figure indicates the microstructure of the steel was composed of a mixture of pearlite and ferrite. To obtain the desired DP microstructure, the pearlite portion of the microstructure is required to revert to carbon rich austenite during annealing which will then be subsequently quenched and transform into martensite.

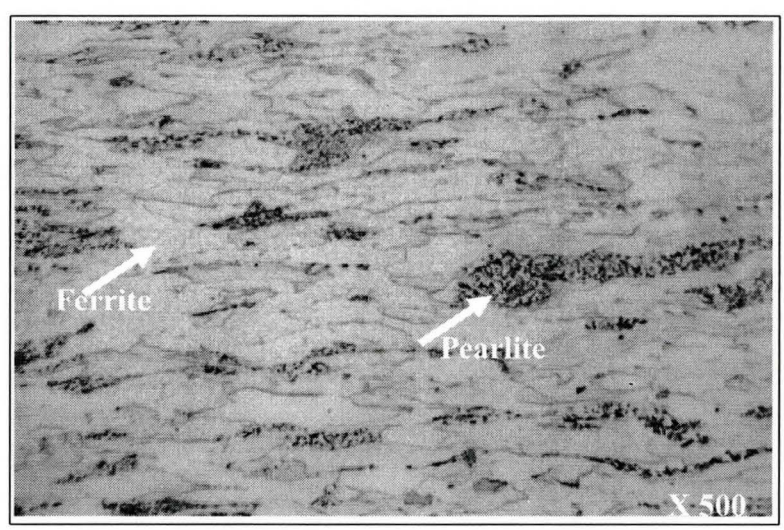

Figure 3.2: Optical micrograph of the surface of the as received sample.

3.1.3 Phase diagram of the Experimental DP 600 Steel

A phase diagram for the experimental steel was generated using the Thermocalc database (TCFE 2000), the results of which are shown in Figure3.3.

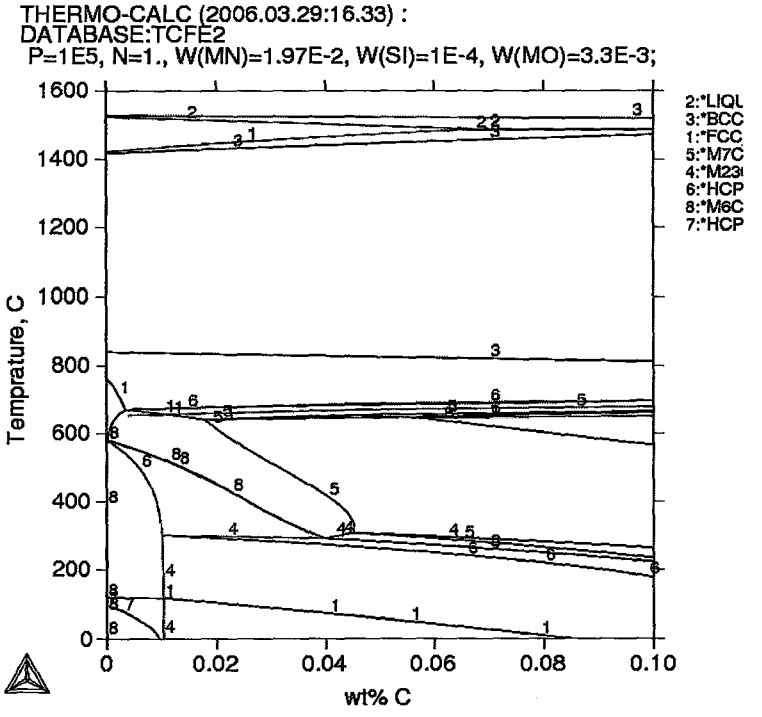

Figure 3.3: Phase diagram of DP 600 steel prepared using the Thermocalc database.

The purpose of generating this diagram was to locate the two phase regions in order to select the temperature range for the subsequent intercritical heat treatment. The selection of the intercritical annealing temperature is critical with respect to obtaining the proper partioning of ferrite and austenite such that the desired dual phase microstructure (ferrite-martensite) is obtained after galvanizing. Based on the phase diagram and the annealing parameters provided by the supplier (Stelco), the peak annealing temperature of the experimental DP 600 steel was selected to be 800 ^{0}C. The volume fraction of the

ferrite and austenite phases at the peak annealing temperature for the steel used in the present experiments is shown in Table 3.3.

Table 3.3: Volume fraction of ferrite and austenite phases for the experimental steel at the peak annealing temperature.

Total volume of phases	Volume Fraction of Austenite	Volume Fraction of ferrite
1	0.7128	0.2871

3.2 Galvanizing Simulator Trials

3.2.1 Description of the McMaster Galvanizing Simulator

The McMaster Galvanizing Simulator (MGS) pictured in Figure. 3.4 was used for the annealing and coating of the experimental samples. This apparatus is capable of fully simulating the industrial continuous galvanizing process. The simulator is fully automated and can manage complex thermal cycles in variable atmospheres. The MGS consists of an atmosphere controlled column where the samples are loaded in the upper most portion of the column. Sample heating was performed in the next bottom portion of the column. In the present experiments, the infrared furnace radiant tube heating was used to anneal the samples. This type of heating is suitable to avoid contamination resulting from direct contact of the sample the heating source. Rapid cooling was accomplished by a flowing jet composed of a mixture of N_2+H_2 in the cooling chamber

positioned at the upper portion of the simulator column. The oxygen potential of the experimental annealing atmosphere was controlled by controlling the pH_2O/pH_2 ratio. The sample temperature was measured by a K-type thermocouple welded to the panel before the panel entered the simulator.

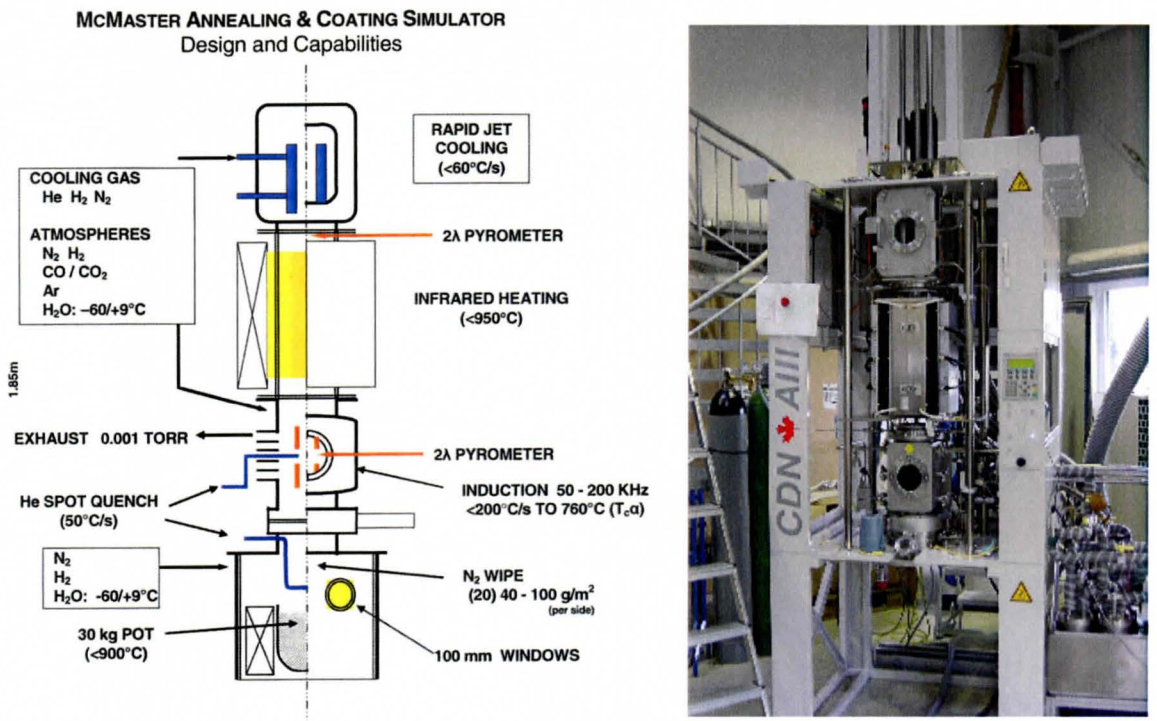

Figure 3.4: (a) Schematic view of the McMaster Galvanizing simulator (b) View of the actual simulator.

An Easydew transmitter equipped with a Michell advanced ceramic sensor was used to measure the water vapour content in the experimental gas mixture via an online hygrometer process. The Michell advanced ceramic moisture sensor was coupled with microprocessor based circuitry to produce a fully calibrated and interchangeable sensor

transmitter. All dew point sensor calibration data is stored within the transmitter flash memory and hence, calibration exchange can be completed in seconds. This transmitter was calibrated over the range of -100 ^{0}C to + 20 ^{0}C dew point to an accuracy of ± 2 ^{0}C and has a very fast dynamic response.

A 50 kg graphite crucible containing molten zinc and aluminum is situated at the bottom of the simulator column. The coating thickness is controlled by flowing N_2 gas through gas jet knives which are situated at the top of the crucible. N_2 gas jet wiping with a flow rate 500 L/min provided an average coating weight of 69g/m^2. Distance of the air knives from the panels, flow rate of the gas and wiping speed were the parameters adjusted to control the coating thickness.

3.2.2 Sample Geometry

The steel panels used in the galvanizing simulator were of the dimensions 200 mm X 120 mm and the thickness of the panel was 1.57 mm. The longitudinal axis of the sample was parallel to the rolling direction. A 'usable area' of 90 mm X 90 mm of uniform coating and temperature, as defined on the sample and is shown in Figure 3.5.

This effective area avoids the edge effect and has a uniform heating and coating zone. The panel thermocouple was welded outside of the coated area, but within the uniform temperature zone, as shown in Figure. 3.5. The bottom edges were trimmed for easier access of the panels to the zinc bath.

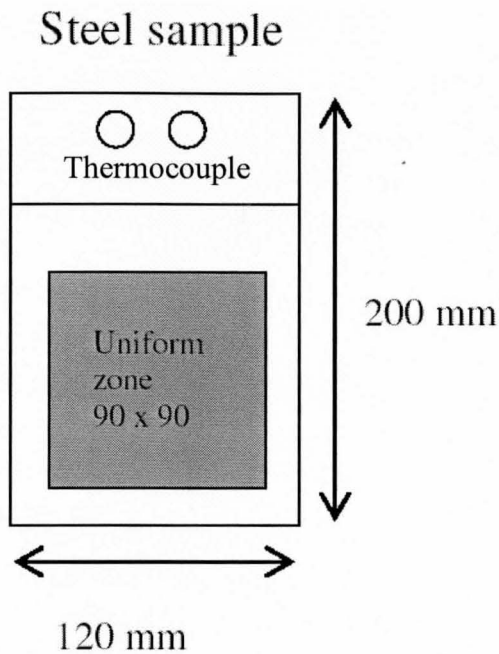

Figure 3.5: McMaster Galvanizing simulator (MGS) Panel Geometry.

3.2.3 Sample Cleaning

The surface of the sample panels was cleaned using a soap water solution and brushed and polished by abrasive papers to eliminate any dirt, loose oxides or organic contaminant. Samples were then rinsed with hot running water and cleaned with ethyl alcohol. Immediately before placing the sample in the simulator, ultrasonic cleaning of the samples was carried out and then they were washed with acetone. After the completion of experiments the samples were immediately stored in isopropanol to avoid further oxidation.

3.2.4 Annealing cycle, Atmosphere and Dipping Parameters

Annealing cycle:

The experimental annealing cycle is shown in Figure 3.6. The thermal cycle parameters were provided by Stelco Inc. and duplicated the industrial thermal cycle used for this material at their Z-line. The thermal cycle was interrupted at 500 ^{0}C, after the rapid heating ramp at 724 ^{0}C , before intercritical annealing at 790 ^{0}C , after soaking at 800 ^{0}C, after rapid quenching and holding at 492 ^{0}C and before dipping into the Zn bath at 460 ^{0}C as shown by points (1) through (7) in Figure 3.6. Thus, these samples were not Zn coated and will be referred as bare samples.

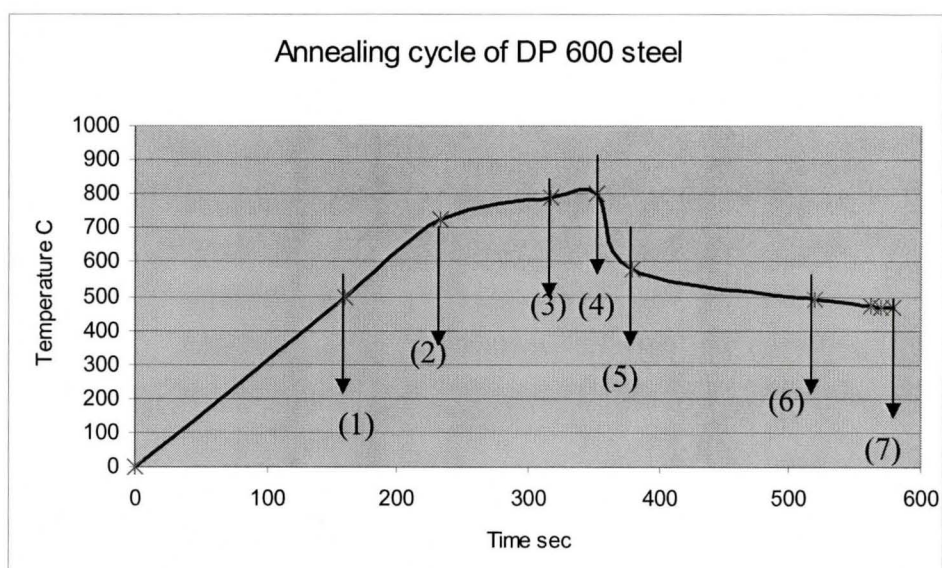

Figure 3.6: Experimental Annealing cycle.

The sample was heated at a rate of 3 °C/s in the fast heating ramp from 0 to 724 °C that was followed by relatively slower heating up to 790 °C at a rate of 0.62 °C/s. The sample was then held at 790 °C for 35 seconds. The temperature was then increased up to 800 °C which is the peak annealing temperature in this experiment. From the peak annealing temperature the sample was rapidly quenched at a rate of 8.6 °C/s to 580 °C and afterwards the sample was cooled slowly to 465 °C. The thermal cycle was interrupted by quenching the sample from the target temperature in the thermal stage to room temperature in order to evaluate evolution of surface structure as a function of time, temperature and the process atmosphere (i.e., oxygen potential). Sample quenching was accomplished by flowing N_2 in the cooling chamber. The evolved surface reactive wetting was analyzed by dipping the samples in the molten zinc bath at 460 °C after the completion of the thermal cycle. The above procedure was performed for all of the experimental annealing atmospheres.

Annealing atmosphere:

Four different annealing atmospheres were used during annealing to observe the change in selective oxidation behavior of the alloying elements, as shown in Table 3.4

The calculation of the pH_2O/pH_2 ratio was performed as follows:

$$H_2(g) + 1/2O_2(g) = H_2O(l) \ldots\ldots\ldots \Delta G_1 \qquad (3.1)$$

$$H_2(g) + 1/2O_2(g) = H_2O(g) \ldots\ldots\ldots \Delta G_2 \qquad (3.2)$$

Table 3.4 Experimental Annealing atmosphere variables.

(1) 20% H_2 , 80% N_2 and -30 ^{0}C dew point **pH_2O/pH_2=0.00211**	**(2)** 5% H_2 , 95% N_2 and -30 ^{0}C dew point **pH_2O/pH_2=0.00844**
(3) 20% H_2 , 80% N_2 and +5 ^{0}C dew point **pH_2O/pH_2=0.03451**	**(4)** 5% H_2 , 95% N_2 and +5 ^{0}C dew point **pH_2O/pH_2=0.14180**

Where, ΔG_1 and ΔG_2 are the Gibb's free energy of reactions (3.1) and (3.2) respectively.

At the dew point,

$$H_2O(g) = H_2O(l) \ldots\ldots\ldots \Delta G_3 = \Delta G_1 - \Delta G_2 \qquad (3.3)$$

Where the reaction equilibrium constant, K, is given by:

$$K = a_{H_2O}(l) / a_{H_2O}(g) \qquad (3.4)$$

At the dew point it can be considered that $a_{H_2O}(l)$ as unity since it is a pure condensed phase. Thus,

$$\Delta G_3 = -RT \ln K$$

$$K = \exp\left(\frac{-\Delta G_3}{RT}\right) \qquad (3.5)$$

$$\frac{1}{a_{H_2O}(g)} = -\exp\left(\frac{-\Delta G_3}{RT}\right) \qquad (3.6)$$

Where, R is the gas constant and T is the absolute temperature. If we assume that H_2O (g) is ideal equation (3.6) becomes:

$$\frac{1}{pH_2O(g)} = \exp\left(\frac{-\Delta G_3}{RT}\right) \qquad (3.7)$$

By evaluating reaction (3.3) at the dew point temperature of interest, we can obtain a value of K and directly obtain pH_2O. The oxidation potential can then be evaluated by using the known H_2 content of the experimental atmospheres to obtain pH_2O/pH_2. For the present case, the lower the pH_2O/pH_2 ratio, the lower the oxygen potential, as per reaction (3.2).

In practice, the oxidation potential of the experimental atmosphere was controlled by changing the dew point temperature [i.e. pH_2O (g)] or H_2 content in the N_2-H_2 atmosphere. N_2 was used as a carrier gas. By increasing either the H_2 content or decreasing pH_2O (g), the furnace annealing atmosphere was made more reducing. To increase the oxygen potential the reverse was done. Referring to Table 3.4, it can be seen that the oxygen potential increase as one moves from atmosphere 1 through 4.

Bath chemistry and Dipping parameters:

The bath chemistry and dipping parameters used in the experiments are shown in Table 3.5. The dipping parameters (time, strip entry temperature) were set to duplicate the Stelco Z-line practice.

Table 3.5 Experimental Dipping Parameters

Effective Al wt% (Fe saturated) [31]	0.19%.
Bath temperature:	460 ^{0}C
Dipping time:	5.0 second
Panel entry temperature	465 ^{0}C
Target coating weight	60g/m^2
Dipping speed	500mm/s
Wiping speed	300mm/s
Wiping gas flow rate	500 l/min

3.3 Sample Characterization

3.3.1 Metallographic Sample Preparation

Samples were cut to an appropriate size by using an abrasive wheel grinder. The sample was degreased with acetone, held upright by a steel spring clamp and cold mounted in organic epoxy resin. Grinding and polishing was performed using an automatic polisher on conventional polishing media (i.e. SiC paper and diamond suspensions). Water free diamond suspensions and lubricants were used to help avoid staining of the coating. Coated metallographic sample etching was done by using 2% HNO_3 + n-Amyl (solvent). The dipping time in the etchant was typically a few seconds and adjusted by trial and error to obtain a satisfactory sample.

3.3.2 Chemical Removal of Zinc Coating layer

In order to examine the Zn substrate interfacial structure, the zinc coating was removed by fuming Nitric acid (90 vol. % HNO_3). This procedure dissolves zinc overlay but does not affect the Fe/Al intermetallics in the galvanized coatings and thus leaves the Al-rich interfacial layer intact [29]. The galvanized sample were cut into a small piece and cleaned thoroughly with acetone. The sample was held by Fluoroware ™ pliers during immersion in the acid. A violent reaction then took place during which the Zn was dissolved. The samples were removed when they had obtained a uniform matte grey appearance. The usual total immersion time was approximately 10 seconds but the individual sample time was fixed by trial and error. The samples were then rinsed with acetone.

3.3.3 Microscopy

3.3.3.1 Optical Microscopy

A Zeiss axioplane-2 optical microscope was used for analyzing the microstructure of the uncoated steel. The micrographs were recorded using a digital camera attached to the microscope.

3.3.3.2 Scanning Electron Microscopy (SEM)

A Philips scanning electron microscope (SEM) was used for imaging and X- ray analysis of the bare sample surface and inhibition layer. Samples were mounted on aluminum studs using silver paint. To minimize surface charging, a gold coating was

applied to the specimen. An accelerating voltage of 10-20 KeV was used to minimize the interaction volume when examining the surface structures. For EDS analyses, samples were tilted 30 degrees to increase the x-ray collection efficiency. X-ray mapping was done with a larger beam diameter (100 nm) and longer exposure of the specimen to the incident electron beam to yield better results.

3.3.3.3 Focused Ion Beam (FIB) Sample Preparation Technique

The Focused Ion Beam (FIB) method was used to prepare the Transmission Electron Microscopy (TEM) samples to observe the Zn/substrate interface. TEM sample preparation was done by FIBICS Incorporated, located in Ottawa. This application is suitable for site specific specimen preparation of difficult materials. In this system, focused gallium ions are used to remove material from a specific site by sputtering, allowing precision milling of the specimen at a submicron scale. The 'Lift out' method was used to remove the sample. The sample was approximately 15 microns wide and 10 to 15 micron thick. After lift out, the sample was mounted on a copper grid and examined in a transmission electron microscope.

3.3.3.4 Transmission Electron Microscopy (TEM)

A JEOL 2010 F TEM/STEM microscope equipped with a FEG gun was used to examine the iron-zinc interface. This is a 200 KV scanning transmission electron microscope equipped with a Si detector and super atmospheric thin window (ATW) for

EDX analysis. The microscope was used in the bright field mode with a 1 nm spot size and 15 cm camera length. The data were recorded by resident INCA software.

3.4 Glow Discharge Optical Emission Spectrometry (GDOES)

GDOES was used for depth profile analysis of both uncoated and coated samples analysis. The McMaster GD PROFILER (HR) ™ manufactured by Jobin Yvon Horiba was used for this purpose. In order to perform an analysis a copper tube (anode) filled with low pressure Ar gas (600 Pa) was brought in contact with a flat sample that was cut to approximately 25 mm X 25 mm in size. 400 Volts were applied between the anode and cathode (sample). Electrons are ejected from the more negatively charged sample surface and are directed towards the anode. On the way they collide with Ar atoms and create positively charged Ar ions and high energy metastable Ar atoms. These positively charged Ar ions are attracted to the negatively charged sample surface. On the way to the sample surface, most of the positively charged Ar ions lose their energy. However, some still possess sufficient energy to strike the sample surface, disintegrate the surface bonds and eject atoms and electrons. This is also known as 'sputtering'. The sputtered atoms are attracted to the anode but the majority is removed by the resident vacuum pump. Some of the sputtered atoms collide with these metastable Ar or high energy electrons and become excited [56]. When they de-excite they emit photons which create a 'glow', the spectrum of which is then analyzed by an optical spectrometer [57].

By measuring photons of different energies (different emission lines), we obtain the relative proportion of each elements present in the sputtered sample. By measuring

the total number of atoms analyzed per second we obtain the sputtering rate. The sputtering rate tells us how much material we have removed from the sample surface. Since the sputtering rate and elemental densities are known, one can quantify the sputtered depth and elemental compositions of all analytes in a single analysis by the following equations [58].

$$Depth = \sum q.\Delta t \qquad (3.8)$$

Where, q is the sputtering rate in microns / sec at each time, Δt, in seconds. The sputtering rate is calculated as follows:

$$I_x = k_x.S_x.R_x.c_x.q + b_x \qquad (3.9)$$

$$c_x = [(I_x - b_{x)} / k_x.R_x.S_x]/q \qquad (3.10)$$

Where,

q is the sputtering rate,

$\mathbf{I_x}$ is the recorded signal from element **x** for a given emission line,

$\mathbf{k_x}$ is the instrument detection efficiency,

$\mathbf{S_x}$ is a correction for self absorption and if assumed negligible, its value is 1,

$\mathbf{R_x}$ is the emission yield i.e., number of photons emitted per supplied atom; the supply rate depends on concentration of element **x** in the sample, $\mathbf{c_x}$, and sputtering rate **q**.

$\mathbf{b_x}$ is the background signal.

In any particular depth in a depth profile, it can be assumed that the summation of concentration of all the elements is 100%. i.e., $\sum c_x = 1$, where $\mathbf{c_x}$ is in units of atomic or mass fraction and thus from equation 3.10

$$q = \Sigma(I_x - b_x)/(k_x.R_x.S_x) \qquad (3.11)$$

Graphical information on these compositional changes as a function of depth will be shown frequently. The parameters $\mathbf{k_x}$, $\mathbf{R_x}$ and $\mathbf{b_x}$ are required for each element **x** in the sample for complete quantitative depth profile of concentration versus depth. In this research, a slow sputtering method was used which optimized the $\mathbf{R_x}$ and $\mathbf{b_x}$. Calibration of the machine prior to performing the analyses was done using Certified Standard Reference (CRF) materials blocks which provides a reasonable value for $\mathbf{k_x}$.

It should be mentioned here that GDOES can be used for elemental profiles, but to obtain information about the compounds or oxidation states of elements X-ray photoelectron spectroscopy was used.

3.5 X-ray Photoelectron Spectroscopy (XPS)

XPS was used to obtain information concerning the oxidation state of elements on the surface of the bare samples and to identify any oxide or other species present. The ability to discriminate different elemental oxidation states is one of the strengths of the XPS technique. XPS is a much more surface sensitive technique than GDOES and depth profiling of the very near surface were also performed by XPS on the bare samples. An X-ray photoelectron spectrometer manufactured by Physical Electronics equipped with MultiPak software (Version 6) was used for the analysis of surface chemistry, oxidation state and depth profiling of the experimental steels. The samples were cut into 1 cm X 1 cm panels for analysis and cleaned with acetone. The X-ray source was monochromatic Al Kα. In the XPS technique, Photonic energy is used to eject electrons from the sample surface. Incident photons are first absorbed by the solid surface atom, ionizing the atom,

which then emits core electrons. The difference in energy between the ionized and core neutral atoms is called the binding energy.

$$KE = h\upsilon - BE - \varphi \qquad (3.12)$$

Where, KE is the kinetic energy of the incident electron, h is Plank's constant, υ is the photon frequency, BE is the binding energy and φ is the work function.

For each atom in a compound or elemental state there is a characteristic binding energy. The emitted photoelectrons have a very short inelastic mean free path in the solid, so this technique is highly surface sensitive. The kinetic energy of the electron is then analyzed by the resident electron energy analyzer. In the present case, the spot diameter was 100 microns and the photoelectron take off angle was 45° versus the sample normal direction. Depth profiles were obtained by ion sputtering the sample under Zalar rotation and analysis sequences. The peak energy position provides information about the elements in the material and their oxidation states. The binding energy of any electron in any orbital of an atom increases as the oxidation state of the atom increases. Peak half widths provide information concerning the lifetime of the photoemission process and the atomic oxidation state. Spectral peak areas provide information on the concentration of element in the sampled region. In the present work, depth profiling of the surfaces were obtained by sputtering at a rate of 14 nm per second.

4. Results

This chapter will present the results obtained from the experimental work and consists of five sections. In the first section, the microstructural and mechanical properties obtained after the simulated thermal cycles are reported. The second section contains the results of the selective surface enrichment of the reactive alloying elements and their oxidation behaviour. This is followed by a discussion of the evolved microstructure and distribution of elements on the surface during annealing and before dipping into the zinc bath. The fourth section contains the results of coating characterization and finally, the fifth section describes the structure of the interface with an emphasis on reactive wetting.

4.1 Microstructure and Mechanical Properties after annealing

In this section, the microstructure and mechanical properties after processing the experimental DP 600 steel through the simulated galvanizing cycle are presented. This was done to confirm the validity of the thermal cycle used in this research and the results are shown in Figure.4.1 and 4.2, respectively.

The micrograph in Figure 4.1 shows the characteristic two phase microstructure of a DP steel, which consists of martensite and ferrite where martensite islands are distributed in the sea of polygonal ferrite, was obtained using the experimental thermal cycle. The true stress-true strain curve (Figure 4.2) shows that the material has a low yield stress (378 MPa) and a high UTS (865 MPa) value without any sharp yield point,

which is also characteristic of a DP steel. The strain hardening exponent, 'n' was calculated from the stress – strain curve and was determined to be 0.193.

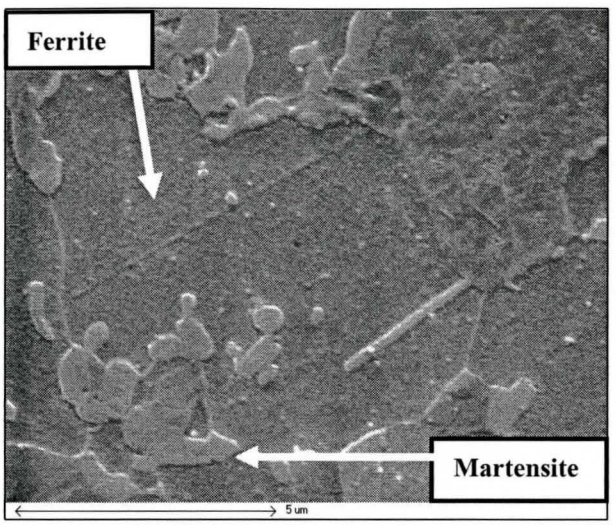

Figure 4.1: SEM Micrograph of the Dual Phase 600 steel microstructure obtained after the simulated galvanizing cycle.

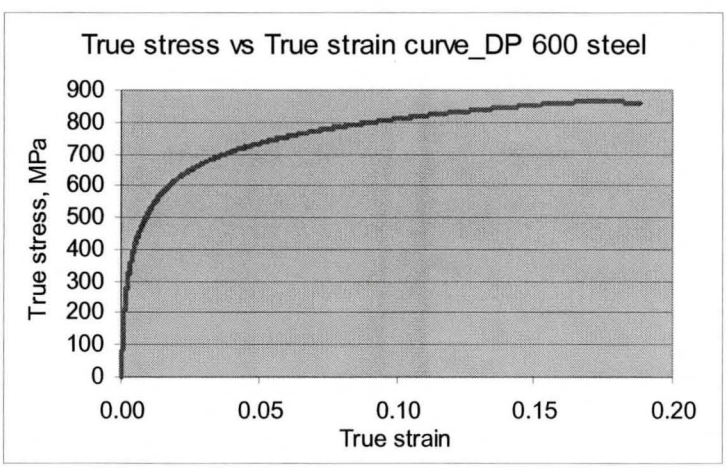

Figure 4.2: True stress-True strain diagram for the processed DP steel

Thus, the microstructural results obtained from the micrograph and tensile properties justify the thermal cycle employed in the present research work since it provided the necessary DP steel property.

4.2 Evolution of Surfaces during Annealing

4.2.1 XPS Analysis of Elemental Depth Profiles as a Function of Annealing Atmosphere

XPS analysis was performed on the as-received samples and on the samples annealed using the four different atmosphere conditions as described in section 3.2.4. Figure 4.3 (a) shows the elemental depth profile obtained from the XPS analysis of the as received sample. The profile indicates the presence of a small amount of Mn and O at the surface.

In all cases, the atmosphere was maintained reducing to iron oxide but it was oxidizing to more reactive alloying elements such as Mn, Mo and Si [9]. The oxidation potential of the annealing atmospheres was varied to observe the selective oxidation behaviour of Mn, Si and Mo as a function of the oxidation potential of the annealing atmosphere. The oxidation potential was increased from Figure 4.3 (b) to (e) by increasing either the water vapour content or reducing the H_2 content of the annealing atmosphere and the selective oxidation of Mn and Si are shown correspondingly. It should also be mentioned that at this stage of the thermal cycle, the samples were ready to dip into the zinc bath.

Figure 4.3(b) shows the most reducing experimental atmosphere (20% H_2 and -30°C dew point). It can be observed that there was significant selective oxidation of manganese to the surface under these conditions, indicating the formation of an external oxide layer. The profiles of the sample at various annealing atmospheres, as shown in Figure 4.2(b) to (e), indicate enrichment of Mn and O at the surface in all cases.

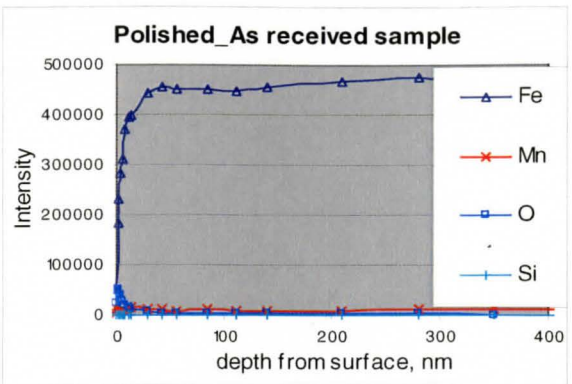

(a) As received sample

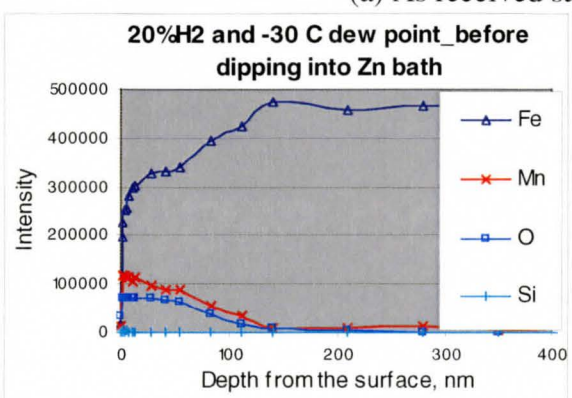

(b) pH_2O/pH_2=0.00211

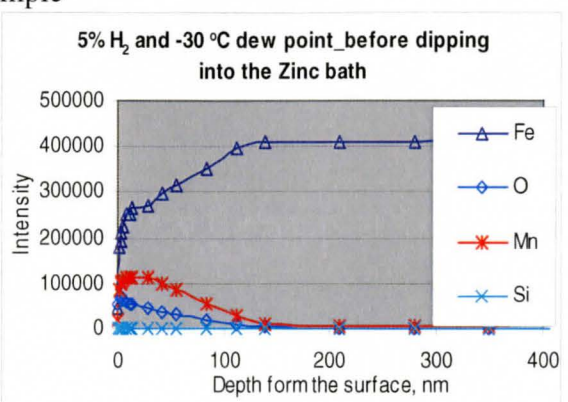

(c) pH_2O/pH_2=0.00844

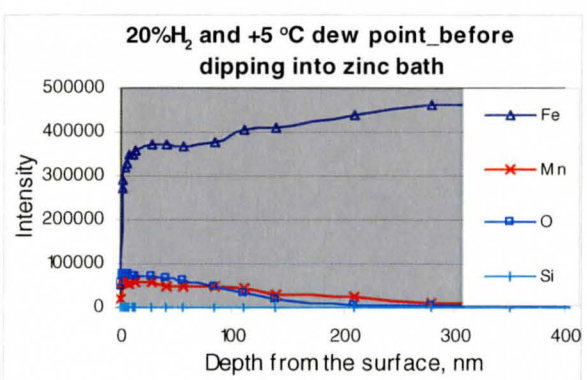

(d) $pH_2O/pH_2 = 0.03451$

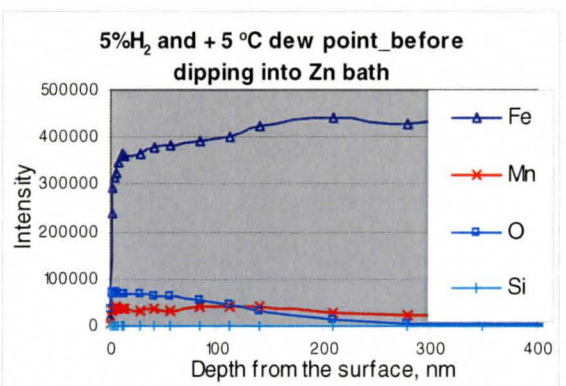

(e) $pH_2O/pH_2 = 0.14180$

Figure 4.3: XPS depth profile of the DP 600 steel; (a) as received sample, (b) - (e) shows elemental segregation with increased oxidation potential of the annealing atmosphere.

The profiles obtained form Figure 4.3 (b) to (e) did not show Si enrichment at the surface, which may be due to the fact that the experimental DP steel contains very low amount of Si (0.01 wt %). Thus, the selective oxidation of Si will not be discussed further in this thesis. The annealing atmosphere oxygen potential was increased through Figure 4.3 (b) to 4.3 (e) and it was found that amount of O and Mn at the surface decreased with the increased oxidation potential. Again, the profiles show greater penetration of oxygen into the material with increased oxidation potential, which indicates an increased tendency towards internal oxidation.

4.2.2 GDOES Observations of Elemental Distribution as a Function of Atmosphere and Time in the Thermal cycle

The selective oxidation behaviour of the alloying elements on the surface and subsurface was studied using GDOES analysis. The elemental Mn depth profiles obtained from the GDOES analysis as a function of time in the annealing cycle for all experimental atmospheres are shown in Figures 4.4 to 4.7. The oxidation potential of the annealing atmosphere was increased progressively from Figures 4.4 to 4.7. The Mn depth profiles obtained from Figures 4.4 to 4.7 show varying selective oxidation behaviour in terms of internal and external oxidation. It was also observed that the oxidation penetration thickness increased with increasing oxidation potential and the external Mn segregation decreases with increased oxidation potential.

Interruption of the thermal cycle at (a) at 500 °C, (b) at 724 °C, (c) before intercritical annealing at 790 °C, (d) after intercritical annealing at 800 °C, (e) after rapid

quenching and holding at 492 °C and (f) just before dipping into the zinc bath at 460 °C provided information concerning the selective oxidation of Mn at particular stages of the annealing cycle for a particular annealing atmosphere.

The profiles (a) through (c) in Figures 4.4 to 4.7 show that external Mn oxidation started before isothermal annealing. Results also show that below 500 °C there was no indication of selective Mn oxidation at the surface except when the oxidation potential was highest [Figure 4.7 (a)]. In this case Mn enrichment at the surface started at temperature below 500 °C and at the same time oxygen began to penetrate into the substrate. The profiles also show that the highest Mn enrichment occurred during the intercritical annealing period [Figure 4.4 to 4.7 (c) to (d)].

Figures 4.4(f) to 4.7 (f) show the Mn depth profiles for the four experimental annealing atmospheres after completion of the thermal cycle and immediately prior to dipping in the zinc bath. Thus, the surface structure and chemistry at this stage will determine the wetting behaviour. One can observe that the external Mn oxidation decreases with increasing oxidation potential and that transition from external to internal oxidation occurred between the pH_2O/pH_2 ratio of 0.00844 to a pH_2O/pH_2 ratio of 0.03451 which is shown in Figure 4.5 and 4.6.

In the present experimental steel, the other most important alloying element is Mo. Figure 4.8 shows the segregation behavior of Mo during the annealing cycle when the atmosphere oxidation potential was the most reducing i.e., (pH_2O/pH_2=0.00211). Figure 4.9 shows the segregation of Mo for the four experimental atmospheres, immediately before dipping the sample into the zinc bath.

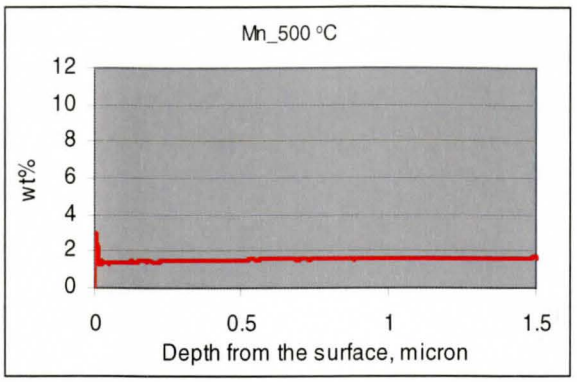

(a)

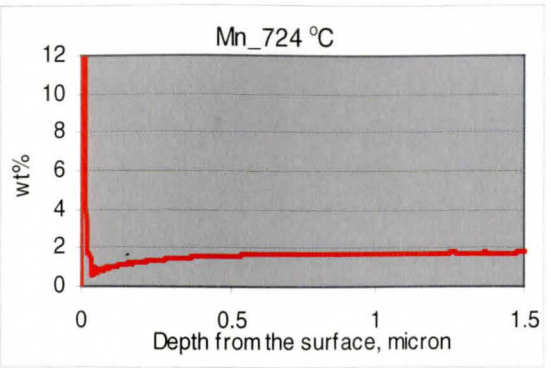

(b)

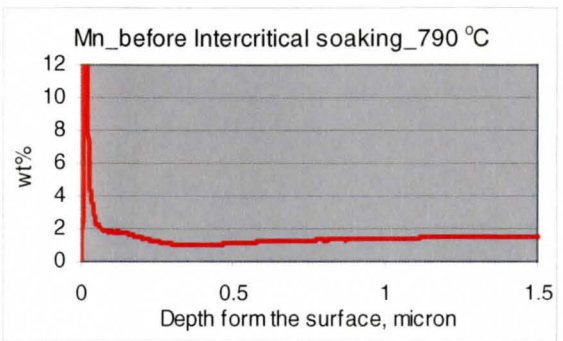

(c)

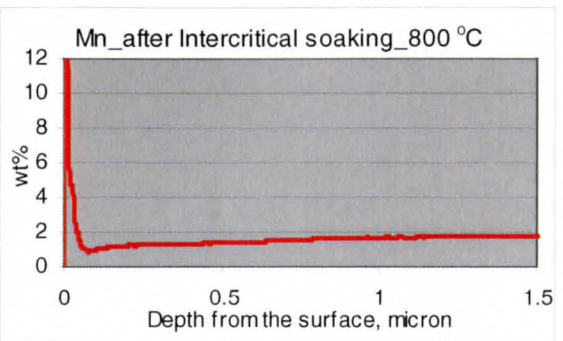

(d)

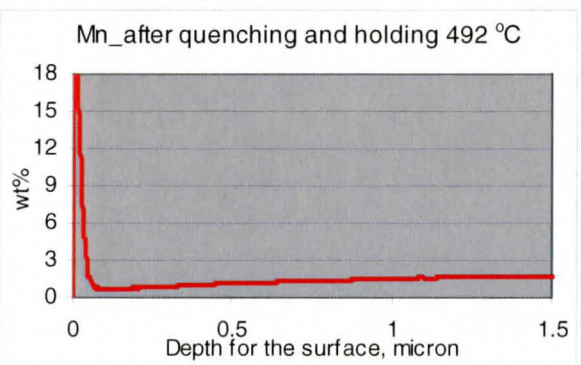

(e)

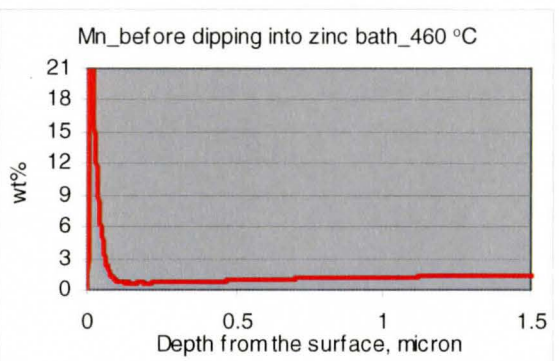

(f)

Figure 4.4: Selective oxidation behaviour of Mn for the 20% H_2 and -30 °C dew point atmosphere (pH_2O/pH_2=0.00211): (a) at 500 °C, (b) at 724 °C, (c) before intercritical annealing at 790 ° C, (d) after intercritical annealing at 800 ° C, (e) after rapid quenching and holding at 492 ° C and (f) just before dipping into the zinc bath at 460 ° C

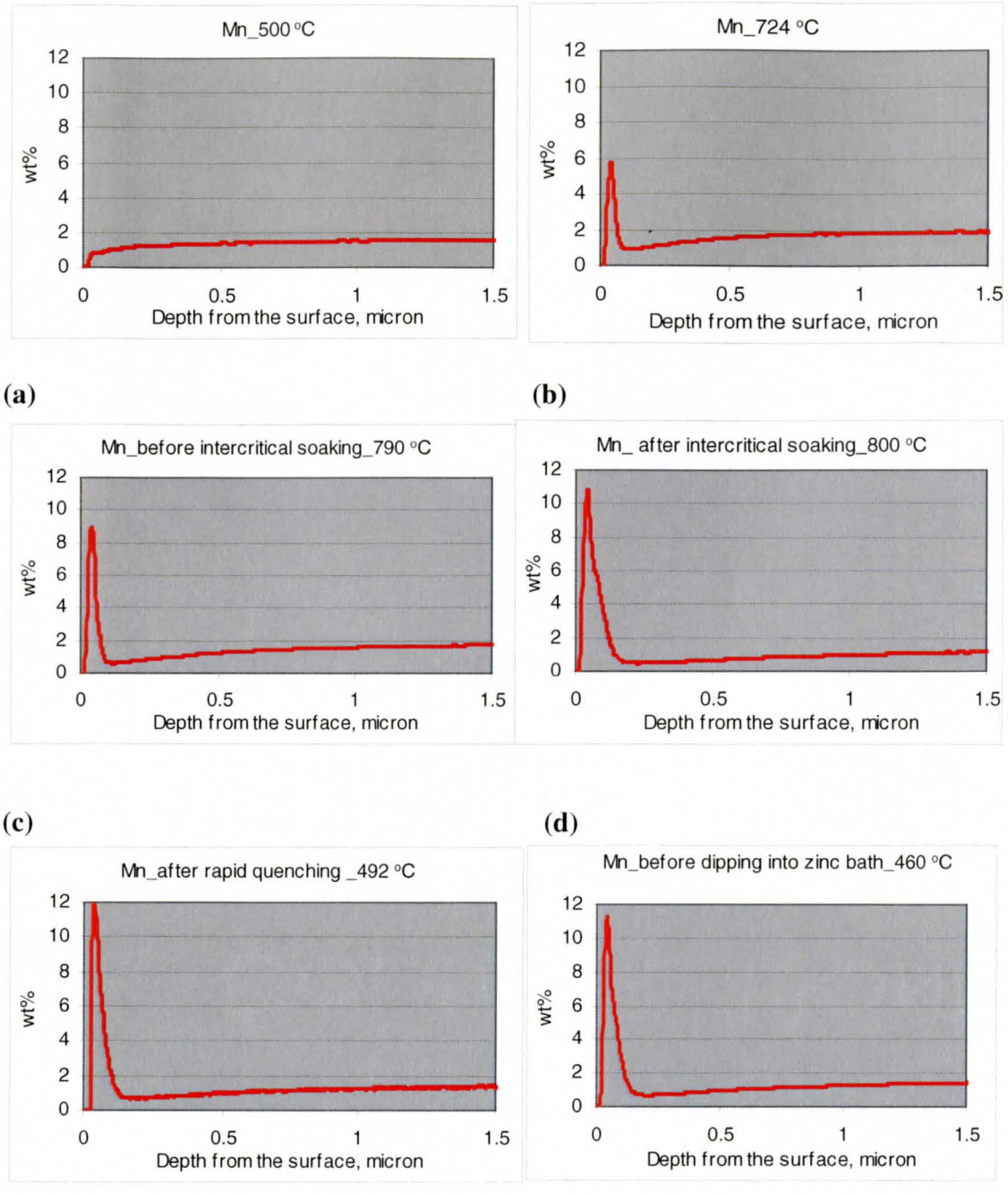

Figure 4.5: Selective oxidation behaviour of Mn for the 5% H_2 and -30 °C dew point atmosphere (pH_2O/pH_2=0.00844): (a) at 500 °C, (b) at 724 ° C, (c) before intercritical annealing at 790 °C, (d) after intercritical annealing at 800 °C, (e) after rapid quenching and holding at 492 °C and (f) just before dipping into the zinc bath at 460 °C

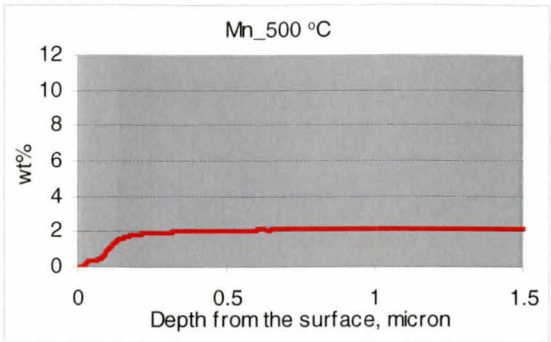

(a)

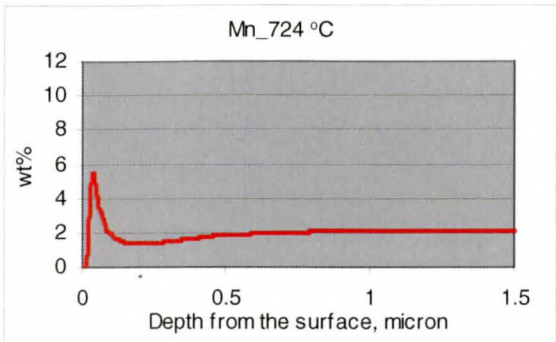

(b)

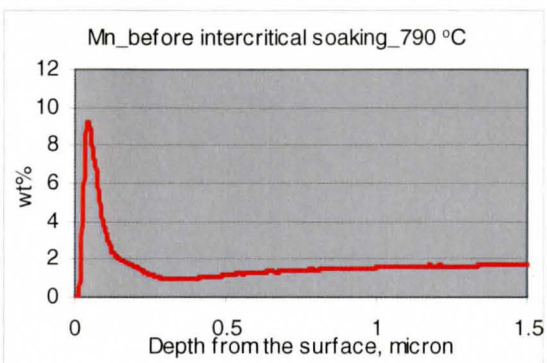

(c)

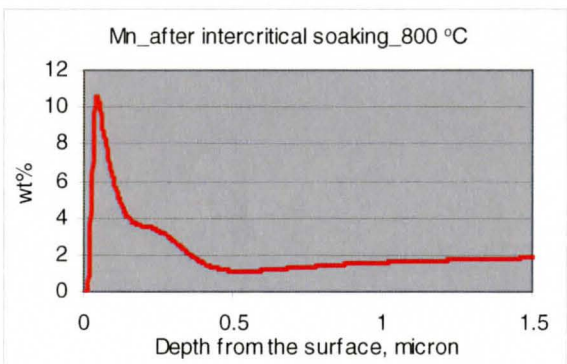

(d)

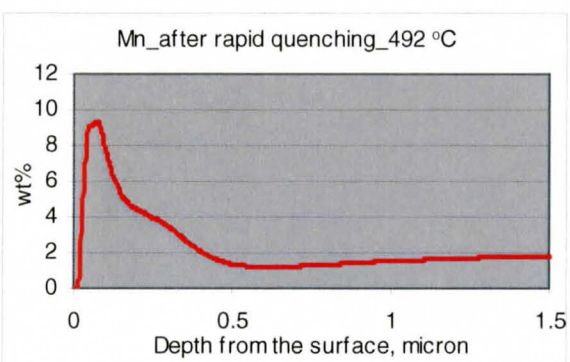

(e)

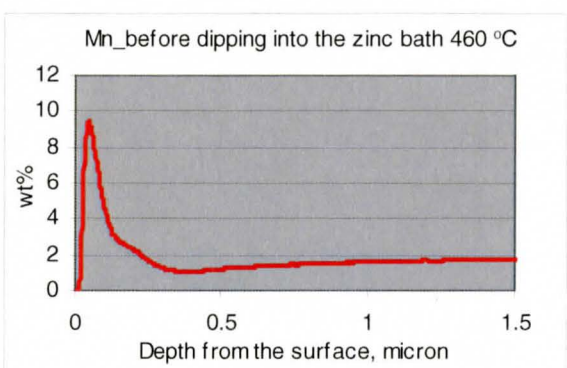

(f)

Figure 4.6: Selective oxidation behaviour of Mn for the 20%H_2 and 5°C dew point atmosphere (pH_2O/pH_2=0.034651: (a) at 500 °C, (b) at 724 °C, (c) before intercritical annealing at 790 °C, (d) after intercritical annealing at 800 °C, (e) after rapid quenching and holding at 492 °C and (f) just before dipping into the zinc bath at 460 °C

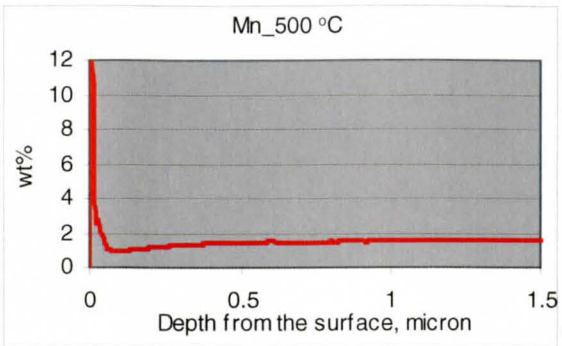

(a)

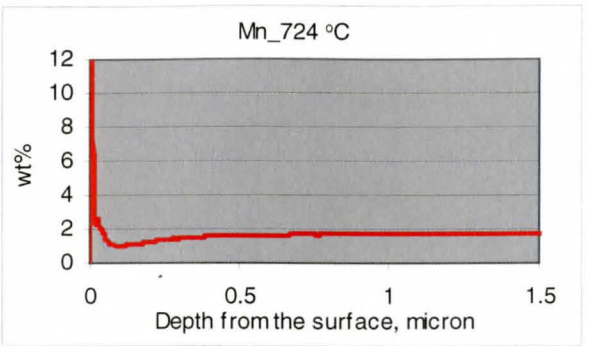

(b)

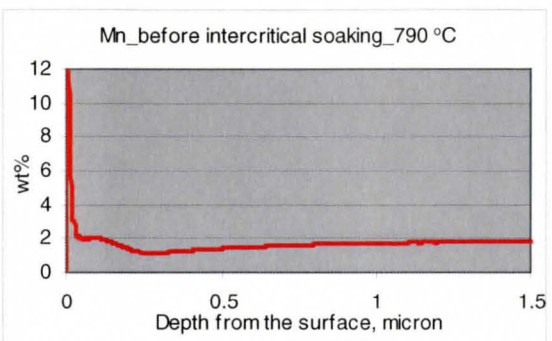

(c)

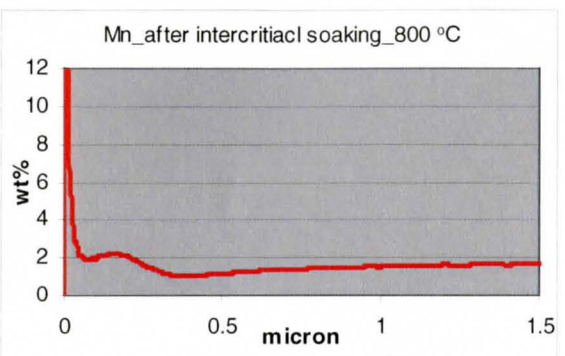

(d)

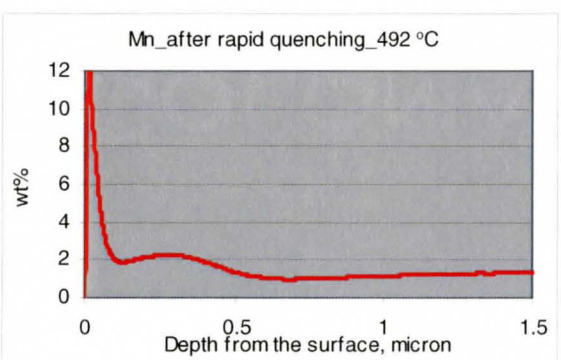

(e)

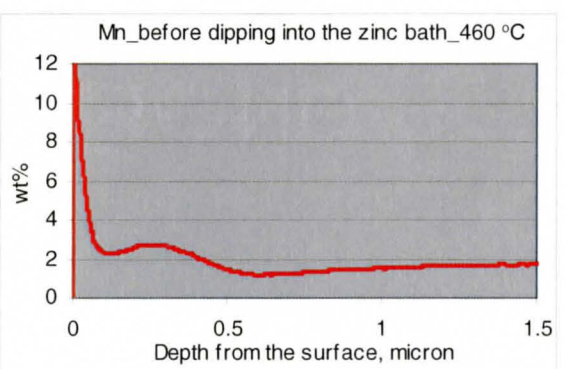

(f)

Figure 4.7: Selective oxidation behaviour of Mn for the 5% H_2 and 5 °C dew point atmosphere (pH_2O/pH_2=0.14180): (a) at 500 °C, (b) at 724 °C, (c) before intercritical annealing at 790 °C, (d) after intercritical annealing at 800 °C, (e) after rapid quenching and holding at 492 °C and (f) just before dipping into the zinc bath at 460 °C.

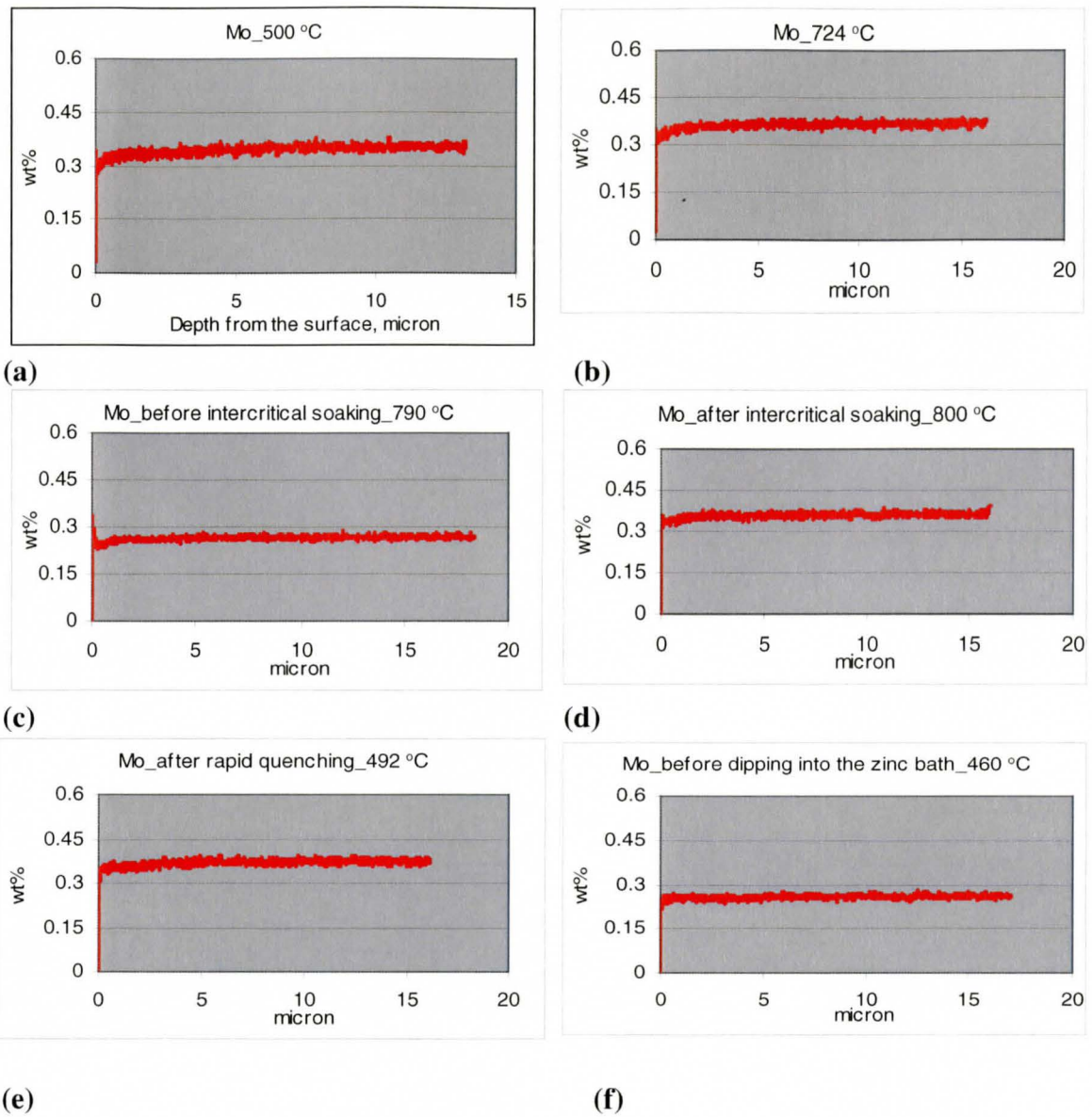

Figure 4.8: Selective oxidation behaviour of Mo for the 20% H_2 and -30 °C dew point atmosphere (pH_2O/pH_2=0.00211): (a) at 500 °C, (b) at 724 °C, (c) before intercritical annealing at 790 °C, (d) after intercritical annealing at 800 °C, (e) after rapid quenching and holding at 492 °C and (f) just before dipping into the zinc bath at 460 °C

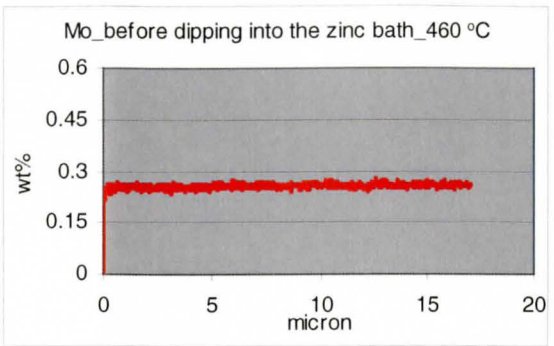

(a) $pH_2O/pH_2=0.00211$

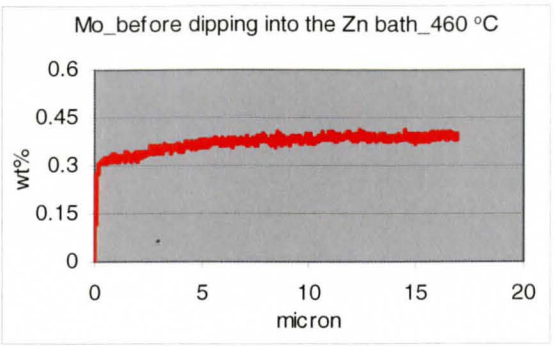

(b) $pH_2O/pH_2=0.00844$

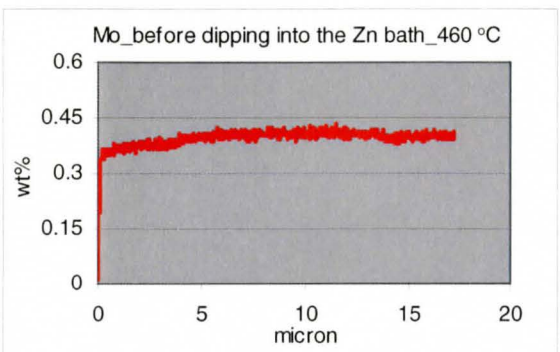

(c) $pH_2O/pH_2=0.03451$

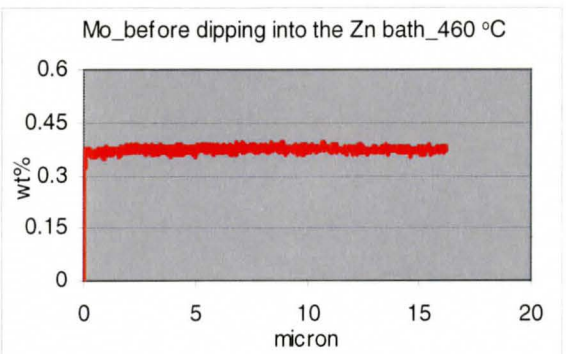

(d) $pH_2O/pH_2=0.14180$

Figure 4.9: Mo distribution before dipping in the zinc bath for all experimental annealing atmospheres immediately prior to dipping in the Zn bath. Oxidation potential of the annealing atmosphere was increased from 4.8 (a) to (d) progressively.

The results show a uniform depth profile for Mo throughout the cycle for all experimental atmospheres. These results supports the work of Rapp [36] and Chipman [59] which showed that due to a small difference in thermodynamic free energies of formation between Fe_xO and ½ MoO_2, internal oxidation of Mo did not occur in dilute Fe-Mo alloys.

4.2.3 XPS Observation of the Oxidation State of the Surface before Dipping

XPS analyses were done to determine the chemical state of the alloying elements present on the surface of the samples before dipping into the zinc bath and also to determine the thickness of the oxide layers. The oxidation states of all the elements present at the surface after the simulated CGL thermal cycle annealing was done by a total spectral analysis. Figure 4.10 shows the total spectral analysis of the before dipping sample processed in an atmosphere of pH_2O/pH_2=0.00844, which shows the presence of Fe (Fe 2p3 photoelectron lines), Mn (Mn2p3 photoelectron lines), C (C1s photoelectron lines) and O (O1s photoelectron lines) peaks at the surface. The LMM lines correspond to the Auger peaks of the respective elements. The presence of peaks at particular energies indicates the presence of specific elements in the sample and their oxidation states.

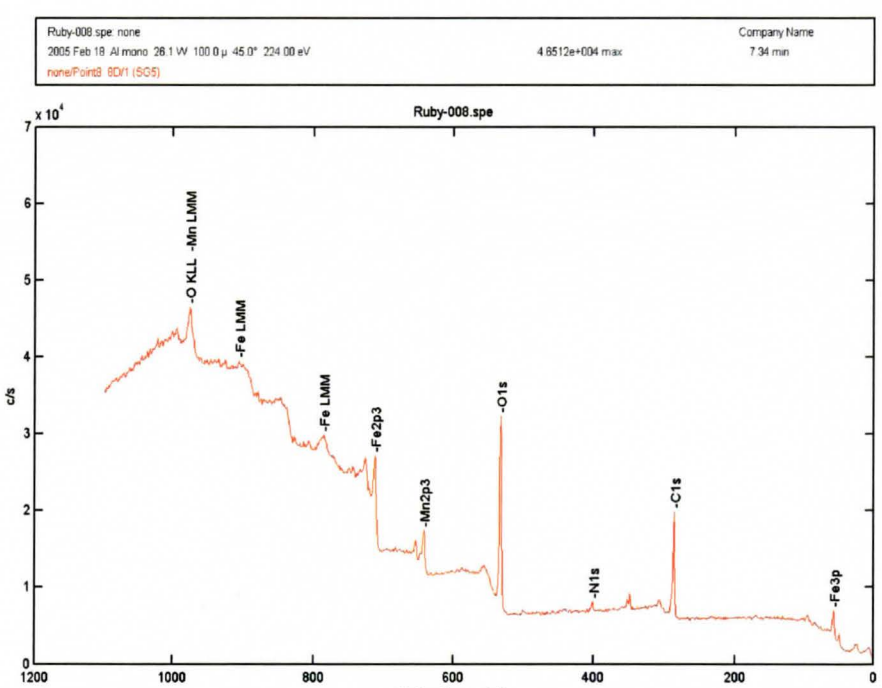

Figure 4.10: Oxidation state of all elements present at the surface before dipping when processed at 5% H_2 and -30 ^{o} C dew point (pH_2O/pH_2=0.00844).

It is worth mentioning that for the four experimental atmospheres, the total spectrum showed the same peaks for the alloying elements and the same elemental oxidation states, although the peak intensities were different for each case. Carbon is a typical artefact for almost any surface exposed to the atmosphere and can probably be discounted. The large O peak observed may come from Fe and / or Mn oxides. The presence of iron oxide is also likely an artefact of sample exposure to post-experimental storage and transportation of the sample. The Mn 2p and Fe 2p peaks have been shown separately in Figures 4.11 and 4.12 respectively.

Figure 4.11 shows the Mn 2p spectra of the processed DP steel, just before dipping into the zinc bath for all experimental annealing atmospheres. The surface was sputtered at 14 nm intervals and each new layer showed the chemical state of the exposed surface. The very first layer shows the chemical state of the outermost surface and successive layers show chemical states beneath the surface of the material. The oxygen potential of the atmosphere was increased from (a) to (d).

The peak at 639 eV represents pure metallic Mn [60]. The peaks at 641.3 eV and at 642.25 eV represents MnO and MnO_2 [61, 62], respectively. From Figure 4.11 it can be deduced that surface Mn is mainly in the form of MnO or MnO_2 in all four experimental conditions. Results also show the existence of metallic Mn after sputtering through 150-200 nm thick layers of manganese oxide.

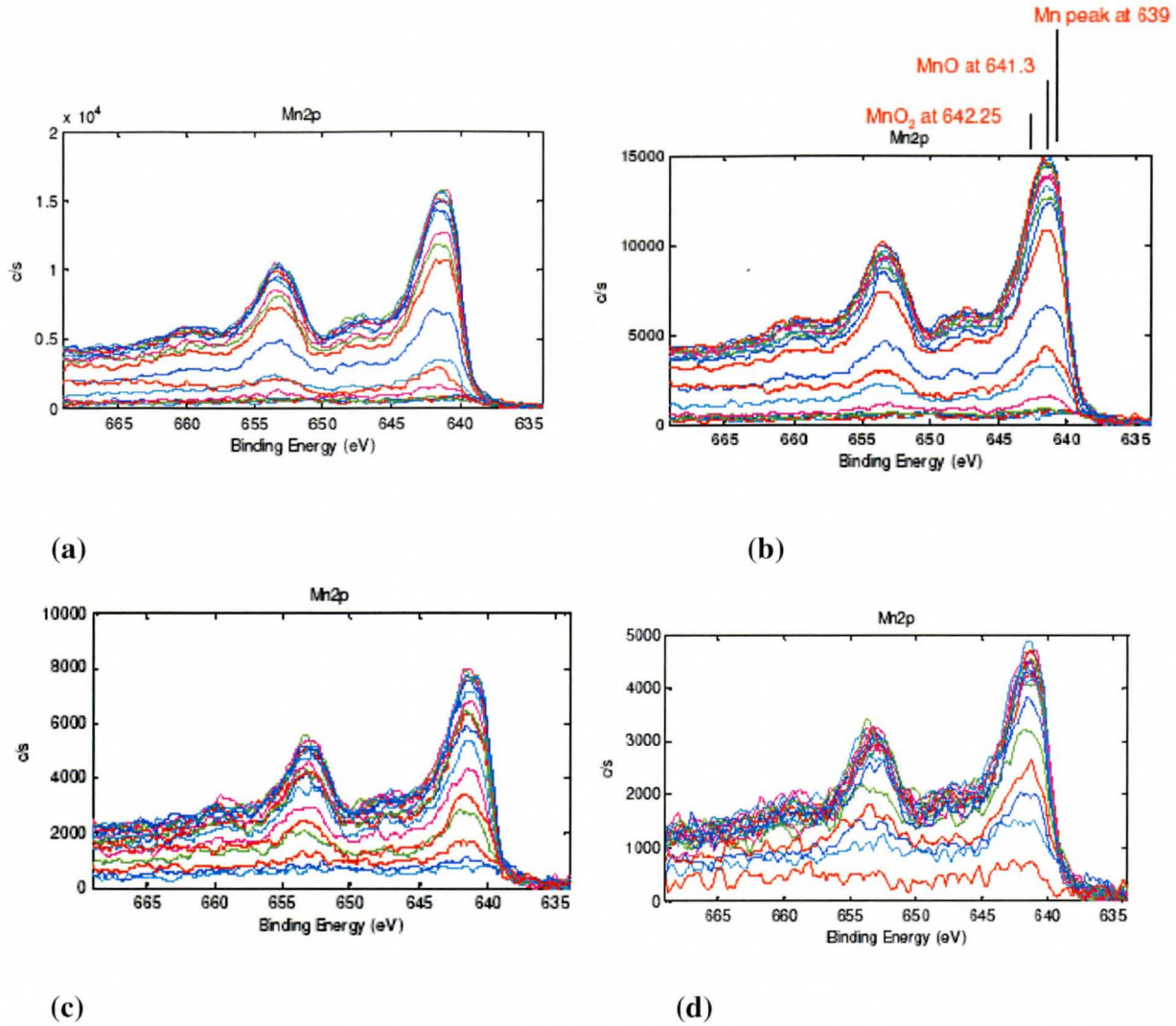

Figure 4.11: Oxidation state of Mn on the sample surface before dipping into the zinc bath at 460 °C. Experimental oxidation potential of the atmosphere was (a) pH_2O/pH_2=0.00211, (b) pH_2O/pH_2=0.00844, (c) pH_2O/pH_2=0.03451 and (d) pH_2O/pH_2=0.14180

Figure 4.12 shows the Fe 2p spectra for all experimental atmospheres from samples immediately before dipping. The results obtained from Figure 4.12 show peaks at 706 eV, 711 eV and a several intermediate peaks at 709-710 eV in all four

atmospheres. The peak at 706 eV represents pure metallic iron [63] and the peak at 710 eV represents iron in the Fe^{3+} valence state [64]. The intermediate peaks shown in the spectra are due to partially oxidized iron. The low binding energy shoulder represents metallic iron beneath the oxides. After removing the first couple of oxide layers (60nm) of Fe_2O_3 and Fe_3O_4, the metallic Fe peak was observed that suggests that these low temperature iron oxides occurred during storage and transportation of the sample after annealing.

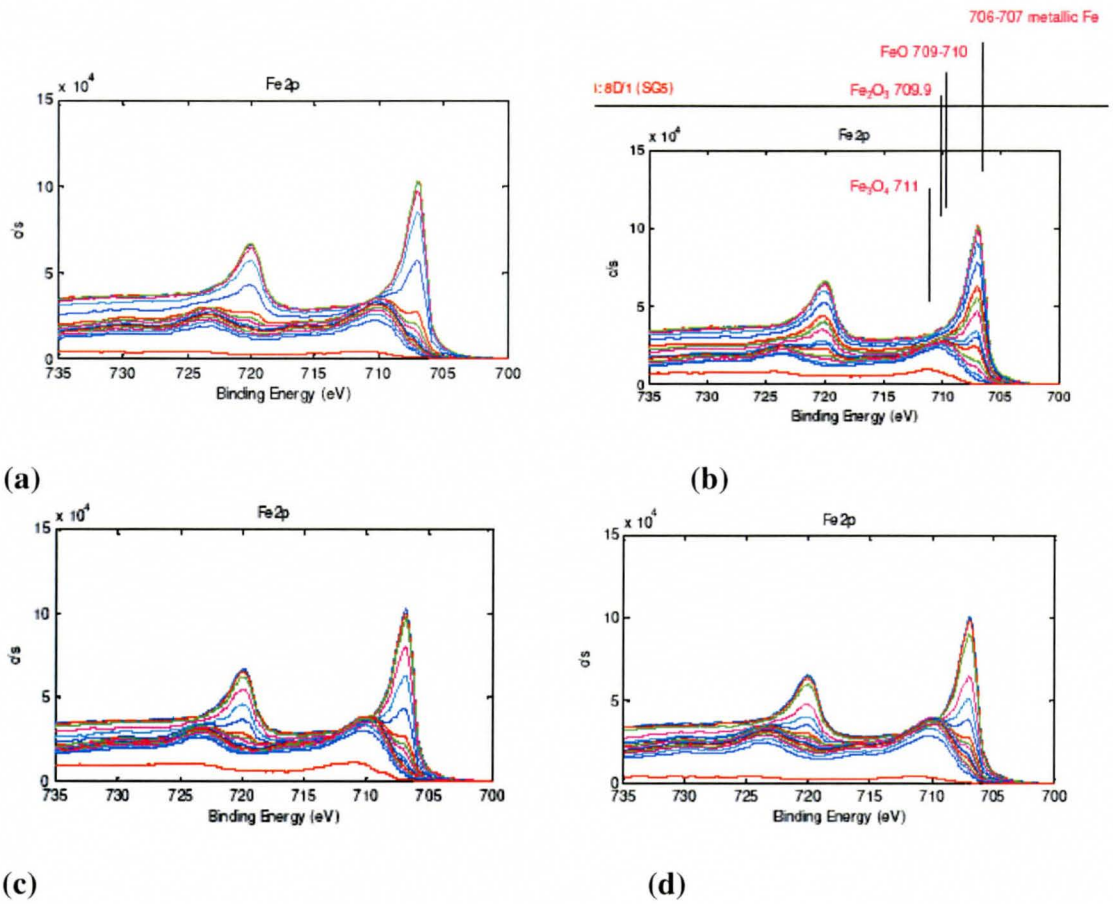

Figure 4.12: Oxidation state of Fe on the sample surface before dipping into the zinc bath at 460 °C. Experimental oxidation potential of the atmosphere was (a) pH_2O/pH_2=0.00211, (b) pH_2O/pH_2=0.00844, (c) pH_2O/pH_2=0.03451 and (d) pH_2O/pH_2=0.14180

4.3 Microstructure of the Surface before Dipping in the Zinc bath

The microstructure of the surface evolved before dipping into the zinc bath was observed under SEM and is shown in Figure 4.13. The SEM micrograph of the DP steel surface (processed at 5%H_2 and -30 °C dew point) shows distinct rolling marks on the surface.

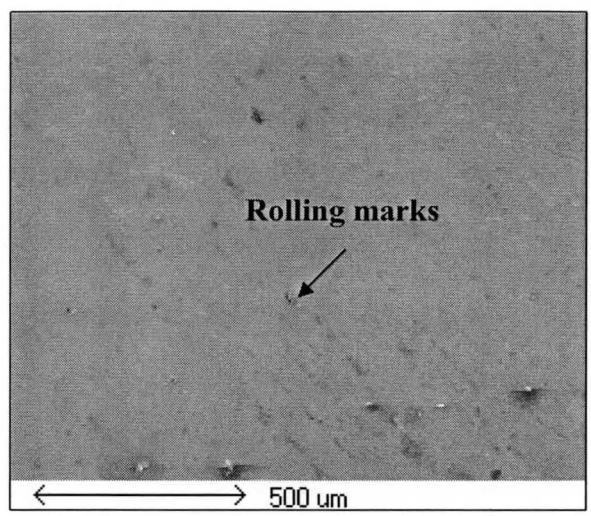

Figure 4.13: SEM image of the evolved surface, annealed in a atmosphere of 5% H2 and -30 °C dew point (pH_2O/pH_2=0.00844)

The Mn distribution on the annealed surface was observed by SEM (Figure 4.14). The micrograph showed a distribution of small Mn enriched islands along a ring (grain boundary). EDS spot analyses of the islands and inside the ring are shown in Table 4.1 (a) and (b) respectively which shows that the islands contain more Mn and O than inside of the grain.

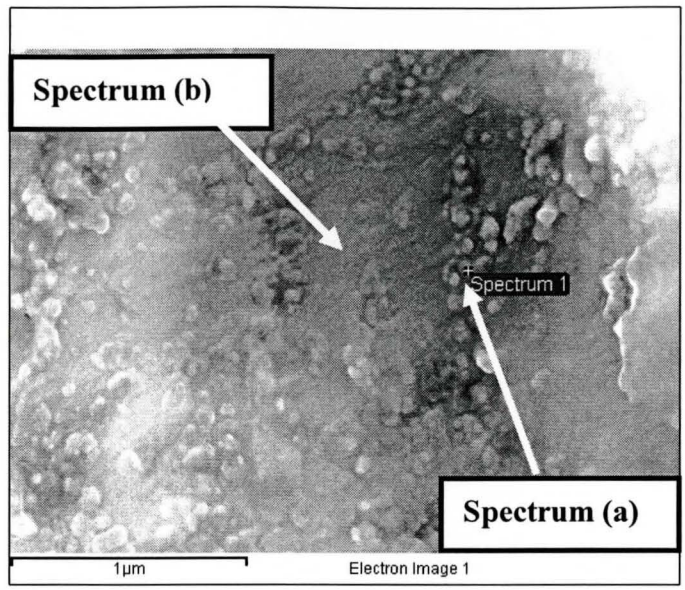

Figure 4.14: SEM image of the evolved surface (observed by JEOL 700F machine at X 70000), annealed in an atmosphere of 5% H_2 and -30 °C dew point (pH_2O/pH_2=0.00844).

Table 4.1: spot analysis of spectrum (a) of Figure 4.14

Element	Weight %	Atom %
O K	2.53	8.30
Mn K	3.53	3.37
Fe K	93.94	88.33
Totals	100	

Table 4.2: spot analysis of spectrum (b) of Figure 4.14

Element	Weight %	Atom %
O K	1.14	3.88
Mn K	1.71	1.69
Fe K	97.15	94.43
Totals	100	

The evidence supports the prediction of Marder [5] that due to relative low percentage of Mn compare to iron in the steel; the Mn oxides should appear as islands rather than uniformly distributed on the surface.

4.4 Coating Characterization

4.4.1 General Coating Observations

General observations of the coatings are shown in Figure 4.15. Figure 4.15(a) to (d) shows photograph of the galvanized samples processed with increasing oxidation potential of the annealing atmosphere.

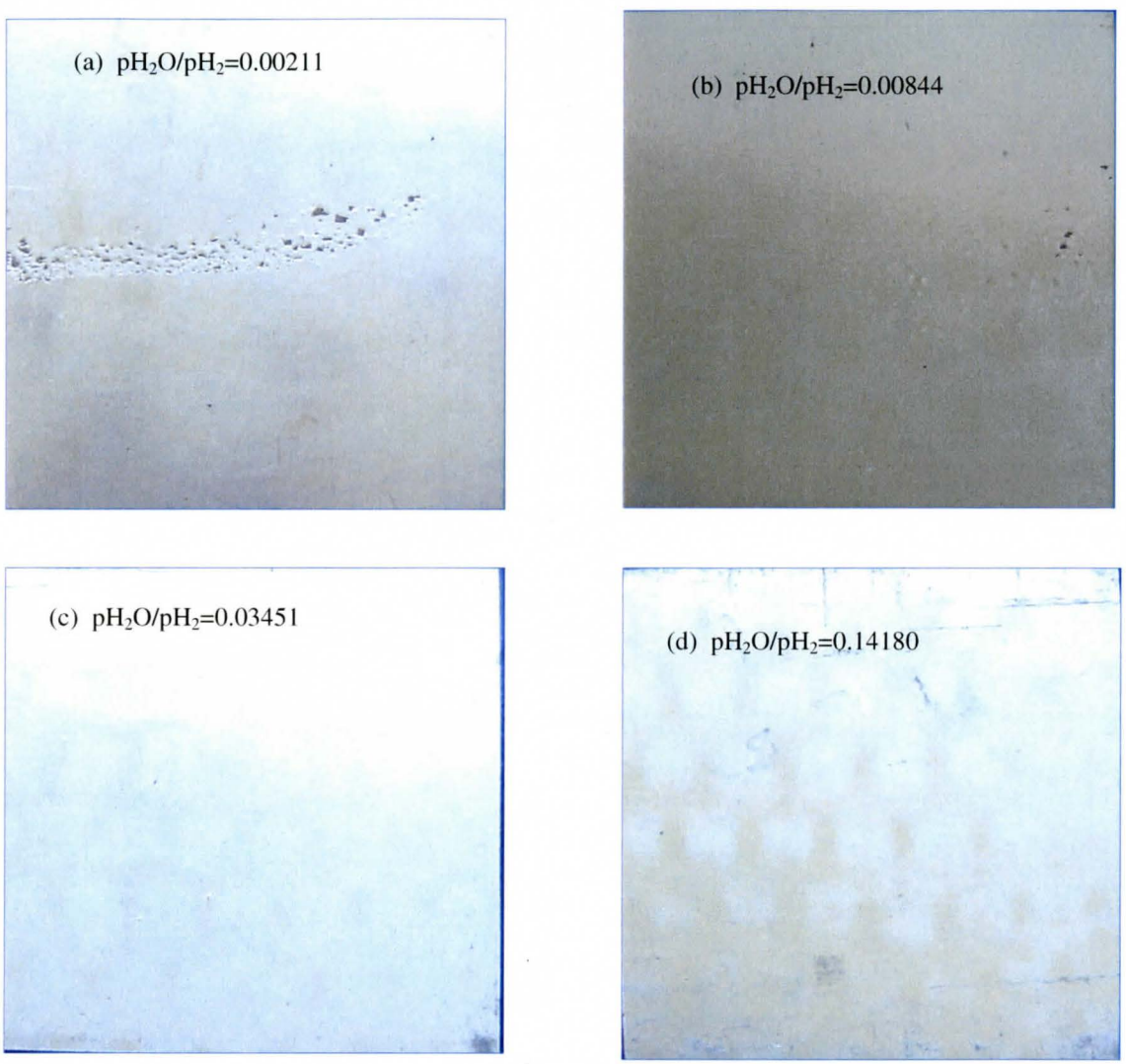

Figure 4.15: Photographs show the 90 mm x 90 mm uniform coating areas of the GI panels. Panels were processed at various annealing atmosphere. Oxidation potential was increased from (a) to (d).

Clearly the photographs indicate good wetting of the DP steel during galvanizing. It can also be observed that all of the panels exhibit good wetting. One can observe a series of bare spots for samples shown in Figure 4.15 (a) which may arise due to local defects e.g., deeper rolling marks (as evidenced in the Figure 4.13) or embedded inclusion, dross or from wiping and may be discounted.

4.4.2 Coating Adherence

Coating adherence was measured using the ASTM A653/A635M-04 180 ° bend test, the results of which are shown in Figure 4.16. It can be seen that under the most severe bending (180° and 1t) the adherence of zinc coating was excellent. The results did not show any evidence of splitting of the coating or edge cracking and the inner surface remained unbroken. These results suggest that the galvanizing of these steel resulted in good reactive wetting and a complete Fe_2Al_5 layer [23, 24]. These results also suggest that the coated sample did not have extensive Fe-Zn intermetallic compounds at the interface [24].

Iron has a higher affinity for aluminum than zinc and the Fe_2Al_5 layer should inhibit and control the inter diffusion of Fe and Zn [27]. Otherwise rapid growth of Fe-Zn intermetallic ($FeZn_7$) might create a thick, brittle layer. It is known that iron zinc bond is strong and presence of Fe-Zn intermetallic deteriorates the formability of the steel. The complete bending of the galvanized samples in the present case is indicative of the formation of Fe_2Al_5 layer in the interface of the material.

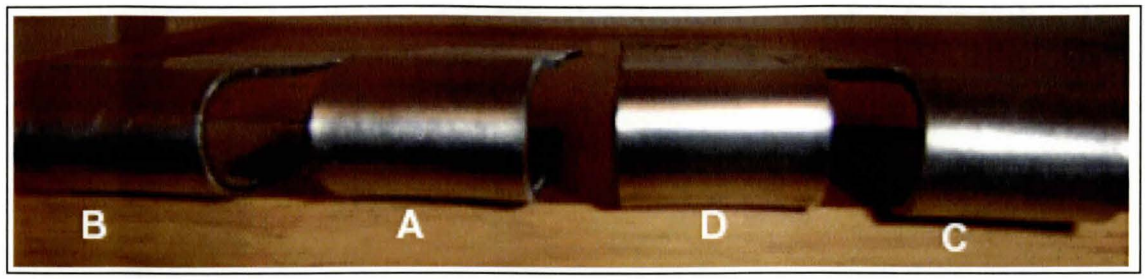

(a) >90 ^{o} bend test result (corners are intact).

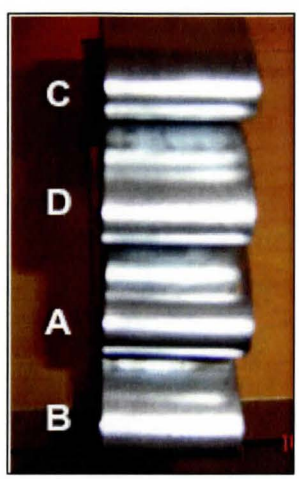

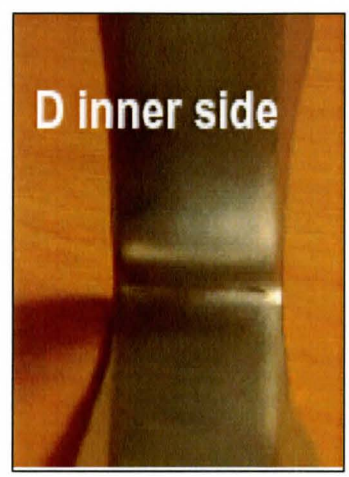

Table 4.3: atmosphere designation for samples in Figure 4.16

Atmosphere	pH_2O/pH_2
A	0.00211
B	0.00844
C	0.03451
D	0.14180

(b) >90 ^{o} bend test result edges are intact (c) > 90 ^{o} inner side is intact

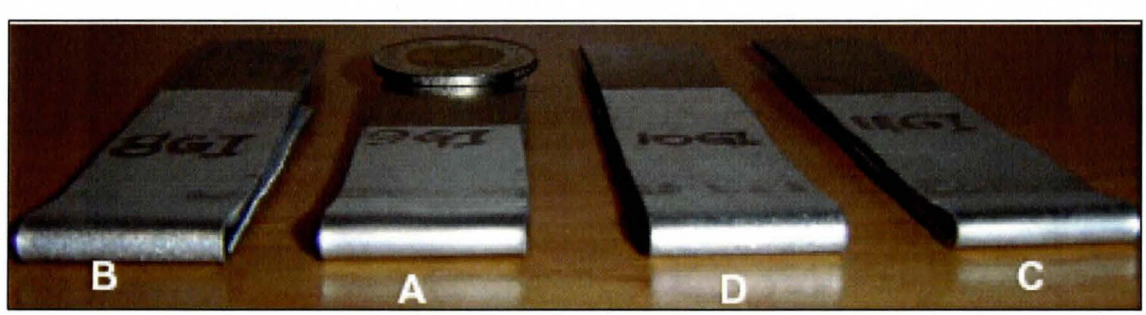

(d) 180 ^{o} and 1 t bend test result (edges and corners are intact)

Figure 4.16: Photograph of bend tested samples. No indication of cracking or splitting of the Zn coating was found.

4.4.3 GDOES Observations of the Coated Samples

The coating morphology was further investigated by GDOES measurements, shown in Figure 4.17.

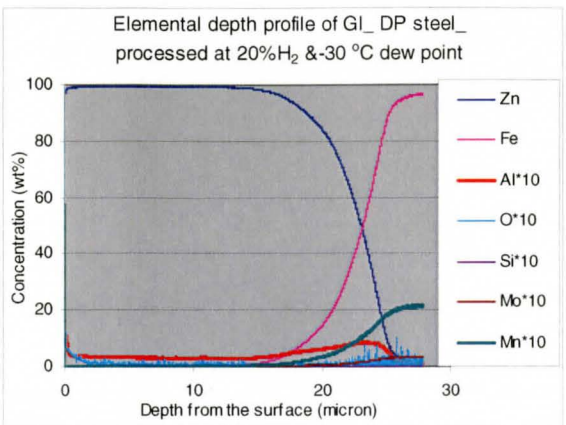

(a) pH_2O/pH_2=0.00211

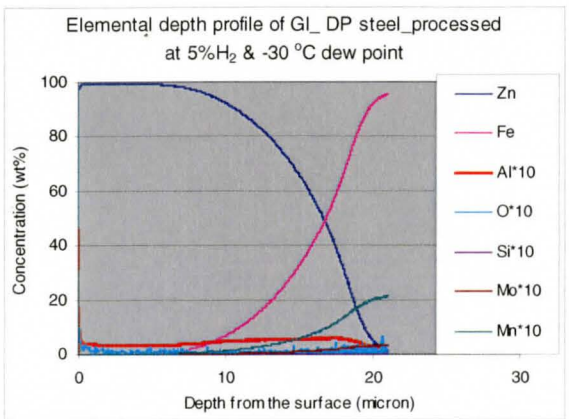

(b) pH_2O/pH_2=0.00844

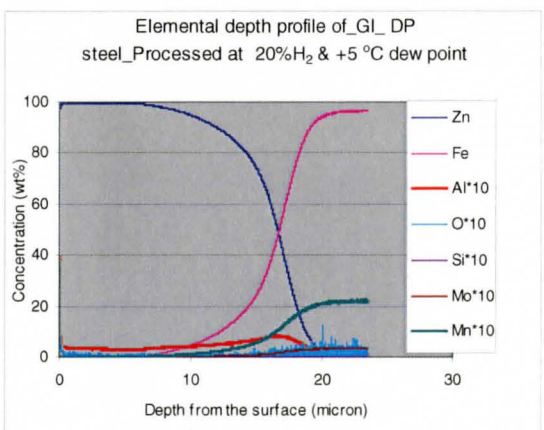

(c) pH_2O/pH_2=0.03451

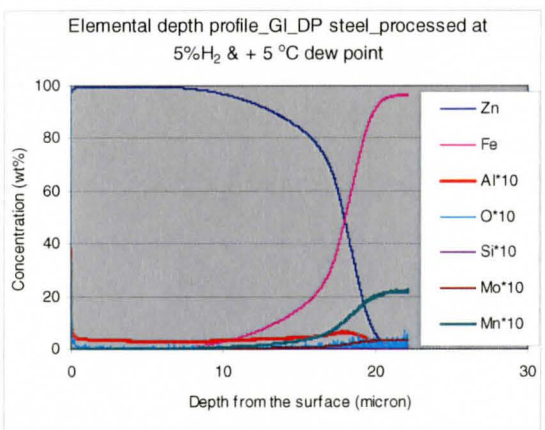

(d) pH_2O/pH_2=0.14180

Figure 4.17: GDOES profiles for GI panels processed at four different experimental annealing atmospheres. Oxidation potential increased from (a) to (d). Note that O, Mn, Si and Mo are multiplied by 10 versus true reading.

The results show that in all four experimental atmospheres, the sample consists of a 20-30 micron uniform zinc coated layer with a clearly defined interface. The observed Al enrichment at the interface is an indication that the Fe_2Al_5 inhibition layer has been formed in all cases. Results also show the presence of Mn at the interface.

It should be noted that Mn profiles have been changed comparing to those in Figure 4.4 (f) through 4.7 (f), i.e. the external Mn oxide film has been removed. This observation would imply that a reaction occurred within the bath to either reduce or alter the MnO film such that the Fe_2Al_5 layer could form. More details concerning possible mechanism to explain this observation will be examined later in the following section.

4.5 Structure of the Coating / Substrate Interface

4.5.1 SEM Observation of the Coating / Substrate Interface

Detailed analysis of the steel / coating interface was done by SEM observation. Analysis of the composition of the interface was carried out by EDS measurements of the zinc stripped surface which is shown in Figure 4.18. The micrographs show a plan view of the steel / coating interface. The oxidation potential of the prior annealing atmosphere was increased from Figure 4.18 (a) to (d). For all experimental conditions, EDS analysis of the interfacial crystals show 43-45 at% Al in their composition indicating the compound is Fe_2Al_5 [29]. Figure 4.18 (a) to (d) show the crystals are uniformly distributed on the surfaces, indicating that reactive wetting occurred over the interfaced area.

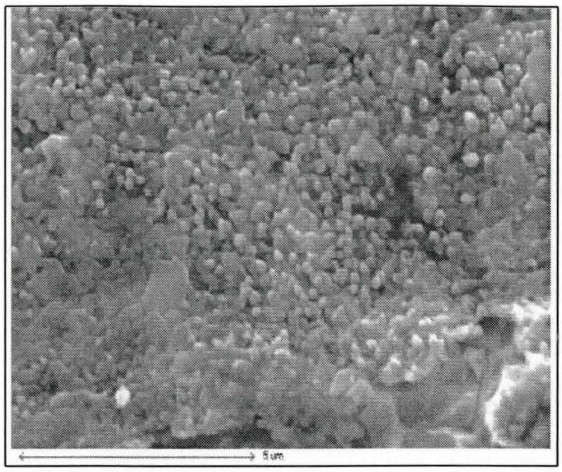

(a) pH_2O/pH_2=0.00211

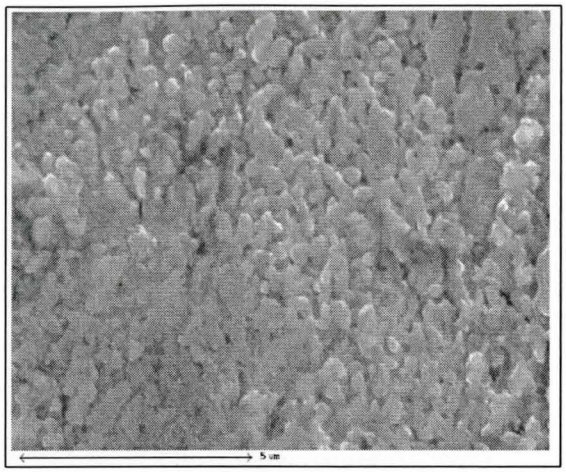

(b) pH_2O/pH_2=0.00844

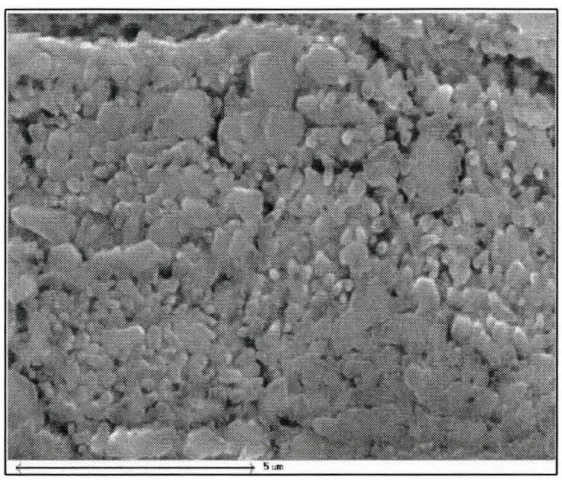

(c) pH_2O/pH_2=0.03451

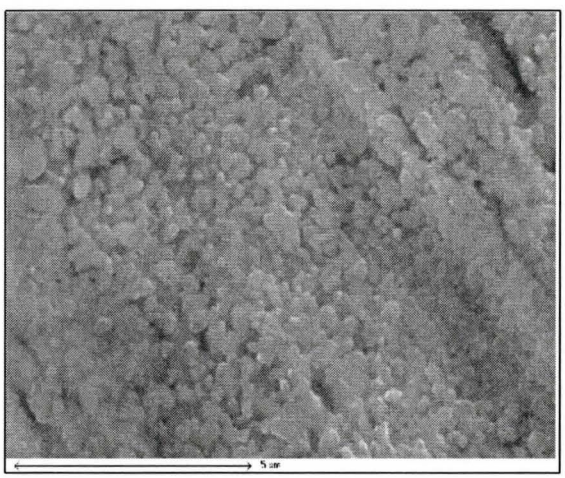

(d) pH_2O/pH_2=0.14180

Figure 4.18: Coating stripped to reveal the inhibition layer. Micrographs show the surface view of the $Fe_2Al_{5-X}Zn_X$ crystal. The oxidation potential of the prior annealing atmosphere increased from (a) to (d).

4.5.2 GDOES Observation of the Coating / Substrate Interface

The significant amounts of MnO or MnO_2 at the external surface (9-19 wt% Mn, shown in Figure. 4.4 (f) to 4.7 (f)) should result in dewetting of the experimental substrate by liquid zinc unless there was some reactive wetting mechanism at the

substrate / bath interface. Thus, we focused on reactive wetting and expected some change in the depth profile of Mn after galvanizing. To assess this, the Zn overlay was removed and the depth profiles of Mn through the interfacial layer analyzed, as shown in Figure 4.19 (a) – (d).

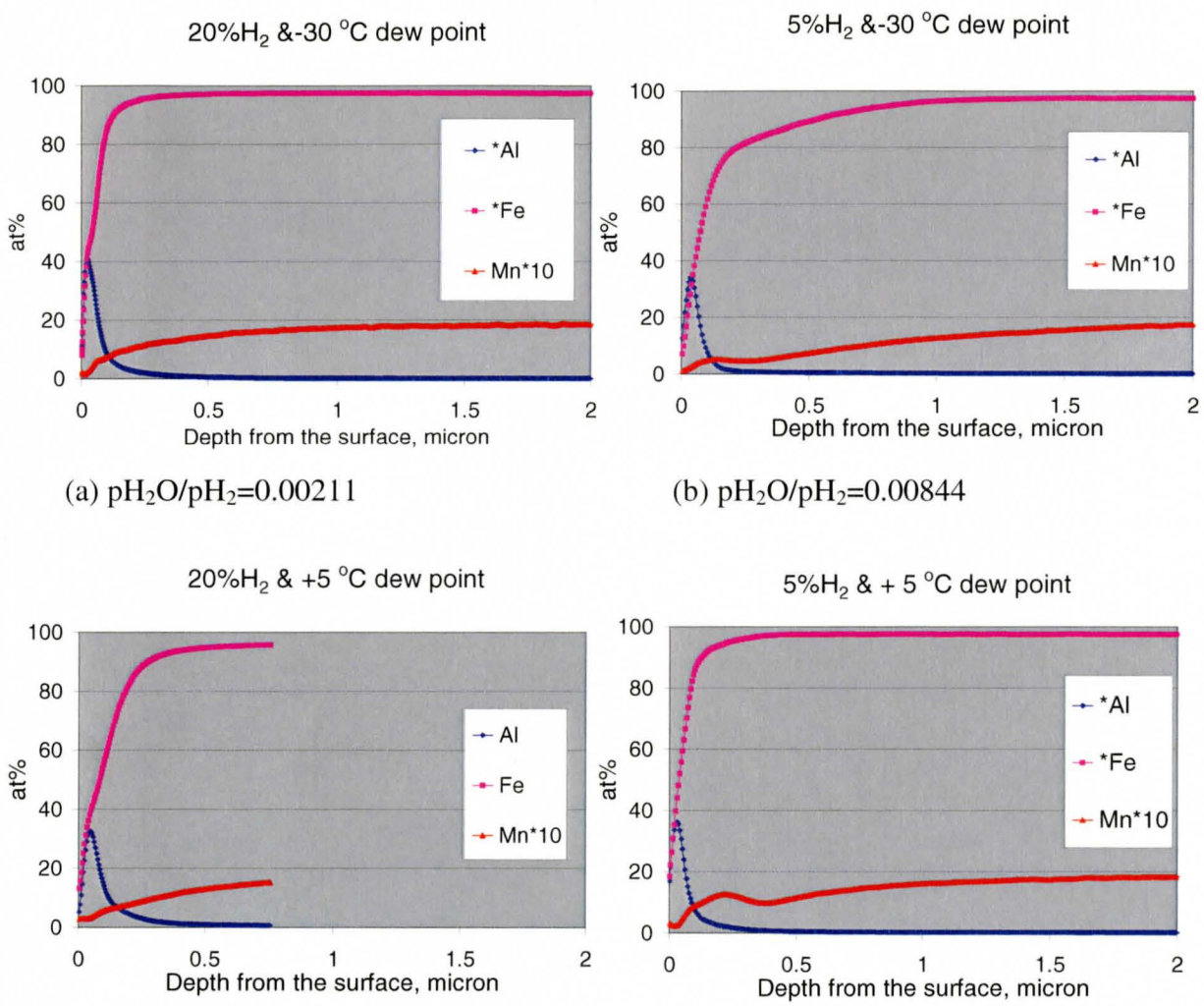

(a) pH_2O/pH_2=0.00211

(b) pH_2O/pH_2=0.00844

(c) pH_2O/pH_2=0.034561

(d) pH_2O/pH_2=0.14180

Figure 4.19: GDOES depth profile of the stripped samples processed at four different experimental annealing atmospheres. Note that Mn is multiplied by 10 versus true reading.

Comparison of Figure 4.19 (a) - (d) to Figures 4.4 (f) - 4.7 (f) clearly shows that the external Mn oxide was removed, which implies that reactive wetting had occurred. This result is also supported by the profiles of Figure 4.17 (a) – (d), where the interfacial Mn was determined to be approximately 2 wt%. It should be noted that the interfacial Al peak in Figure 4.19 (a) - (d) is due to the presence of the inhibition layer. It is also observed that the interfacial layer seems to have some Mn in it. This may be an artifact of sputtering geometry but may also indicate that there has been some substitution of Mn into the interfacial layer or $Fe_2Al_{5-x}Zn_x$ crystal structure.

4.5.3 TEM Observation at the Coating / Substrate Interface

TEM on a cross-section of the coating / substrate interface was performed to study the exact structure and position of Mn at the interface. Figure 4.20 shows the bright field image of the coating interface. A line scan was performed in the STEM mode across the interface which allowed determination of the elemental distribution across the interface. The elemental profiles of Fe, Zn, Al, Mn and O are shown in Figure 4.21.

The result clearly shows the presence of Mn at the interface. It is also observed that the MnO film dissociated (as evidenced by low O) and the inhibition layer formed (as evidenced by Al enrichment at the interface). The profile of Al shows that Al is present in the range of 400 to 600 nm. From this data, it can be roughly estimated that inhibition layer was approximately 200 nm thick.

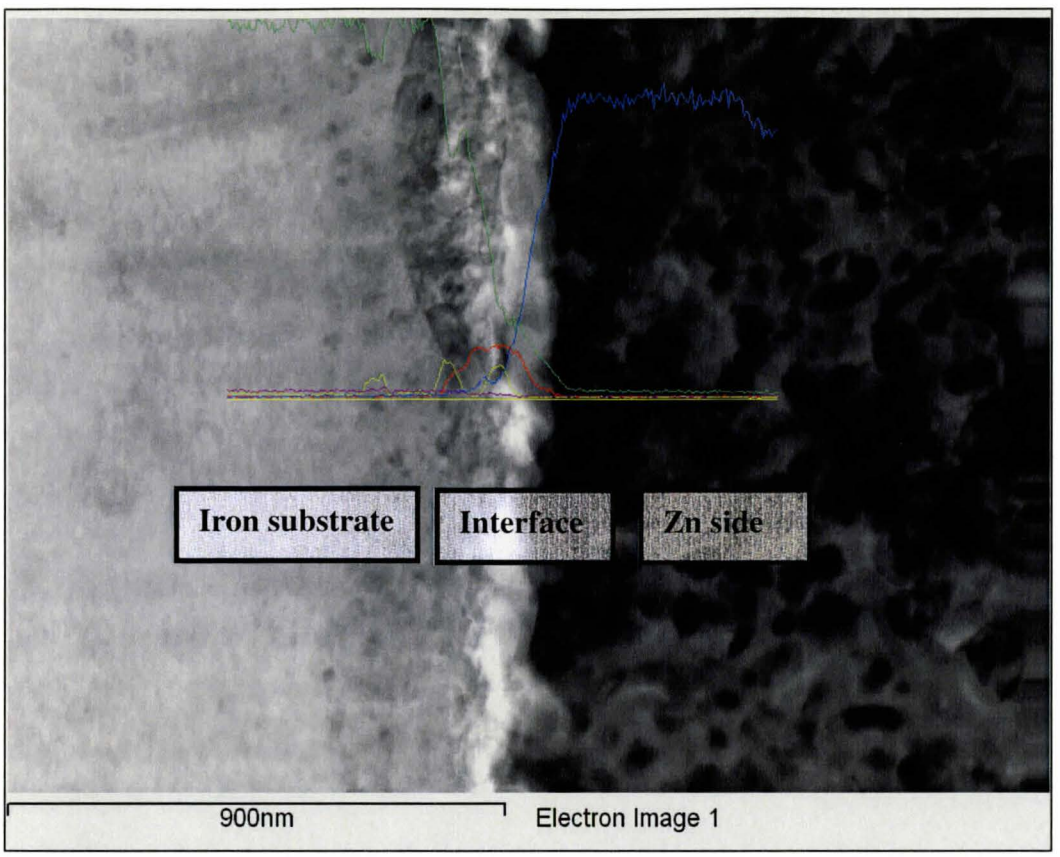

Figure 4.20: TEM micrograph and line scan observation at the Fe-Zn interface. Color code of the spectrum of the line scan: Yellow color refers to Mn, red refers to Al, green refers to Fe, blue refers to Zn and pink refers to O.

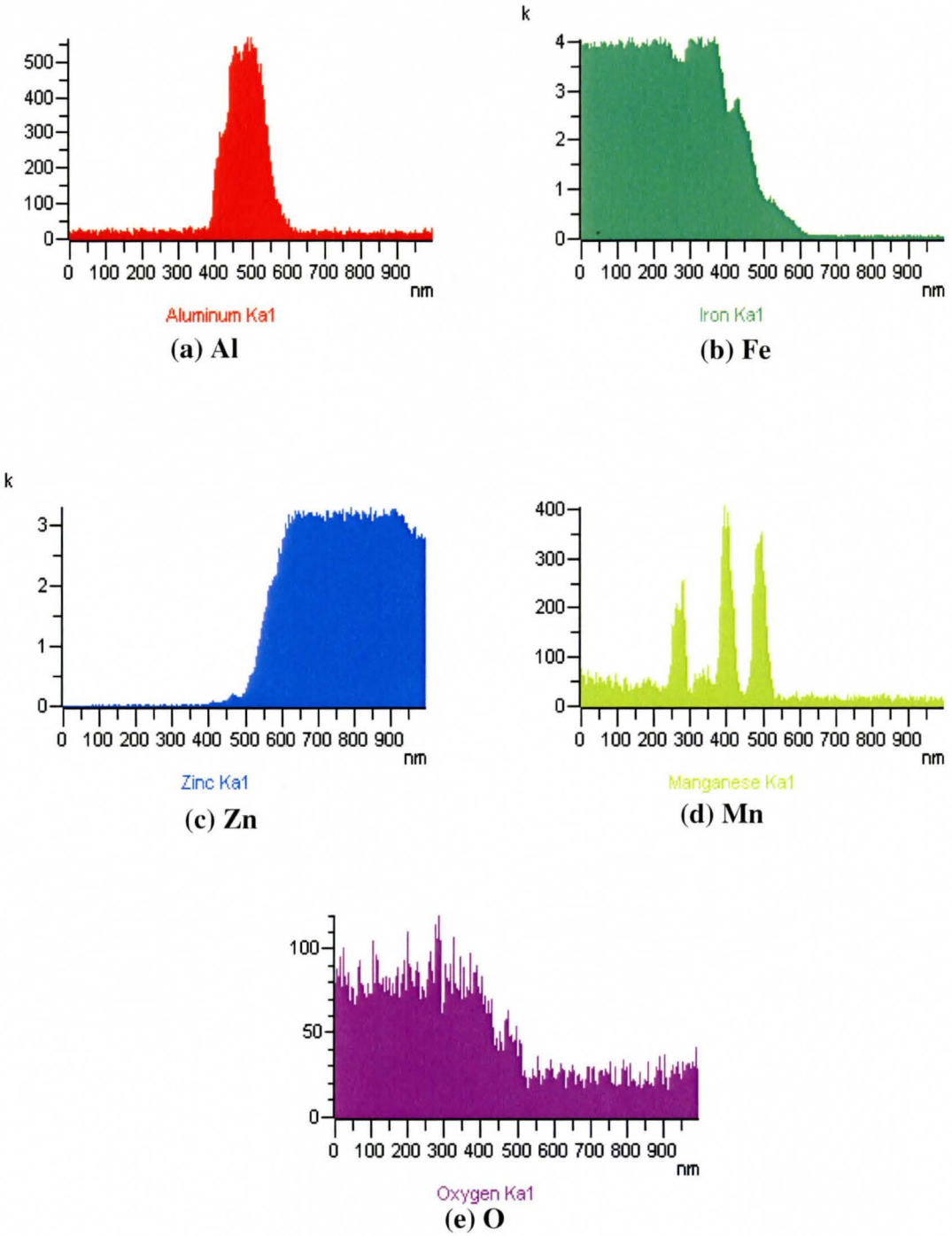

Figure 4.21: Elemental line scan spectra of (a) Al, (b) Fe, (c) Zn, (d) Mn and (e) O across the Fe-Zn interface shown in Figure 4.20

To understand the structure of the interface, High Resolution Transmission Electron Microscopy (HRTEM) was performed on the interface. A bright field image of the interface is shown in Figure 4.22. HRTEM observations of the interface were carried out and a series of lattice fringe patterns from the iron side to the zinc side of the interface were recorded to determine the crystal structure and identify the interfacial phases. From the lattice fringe patterns, shown in Figure 4.23, interplanar spacing were calculated and later matched with standard data sources [65, 66, 67] to determine the local crystal structure. The analysis of these data confirms the presence of the Fe_2Al_5 layer in the interface which is shown in Figure. 4.24 (a) and (b). Lattice fringe patterns also found the presence of Al $Mn_{0.75}Fe_{2.25}$ crystals at the interface which is shown in Figure. 4.24 (c). MnO was not detected in the analysis.

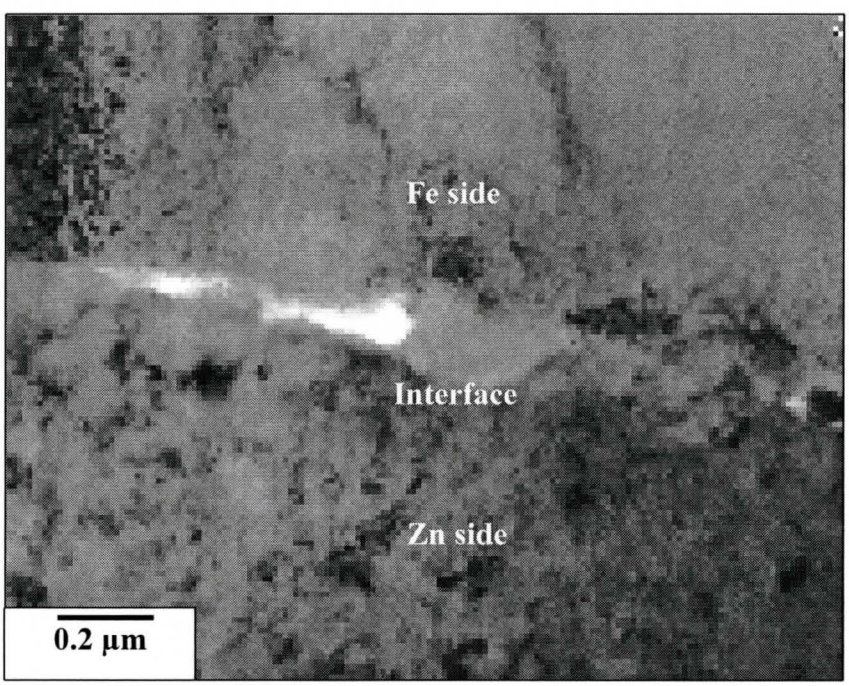

Figure 4.22: Bright Field TEM image of the Fe-Zn interface

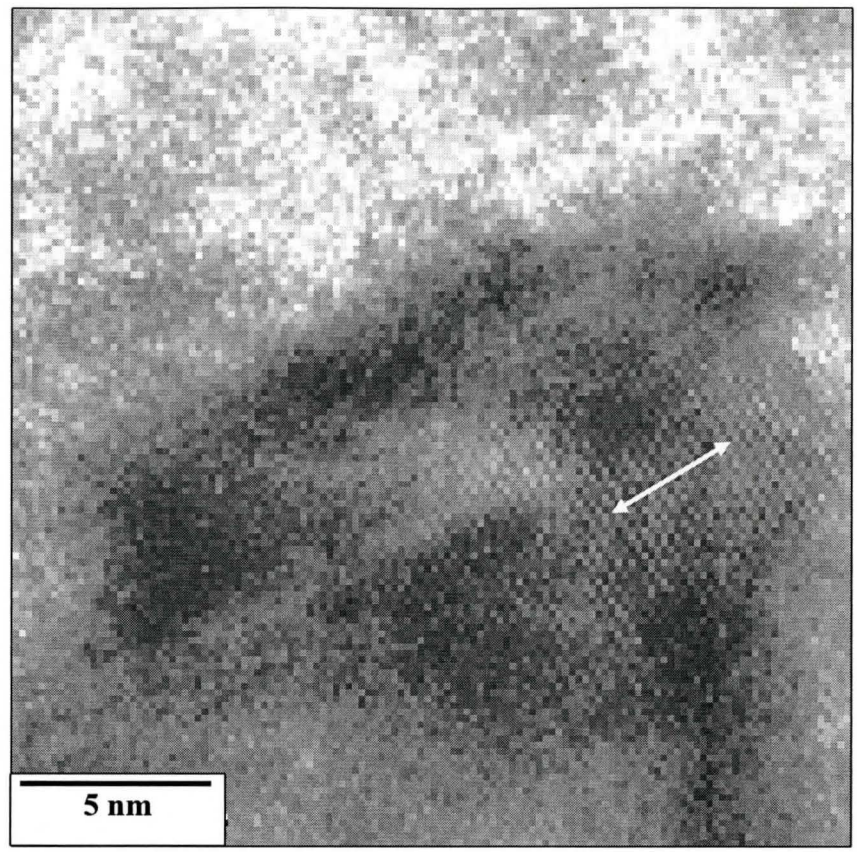

Figure 4.23: HRTEM lattice fringe pattern taken from the interface. Arrow mark shows the parallel lines of diffraction from where'd' spacing of the crystal could be calculated.

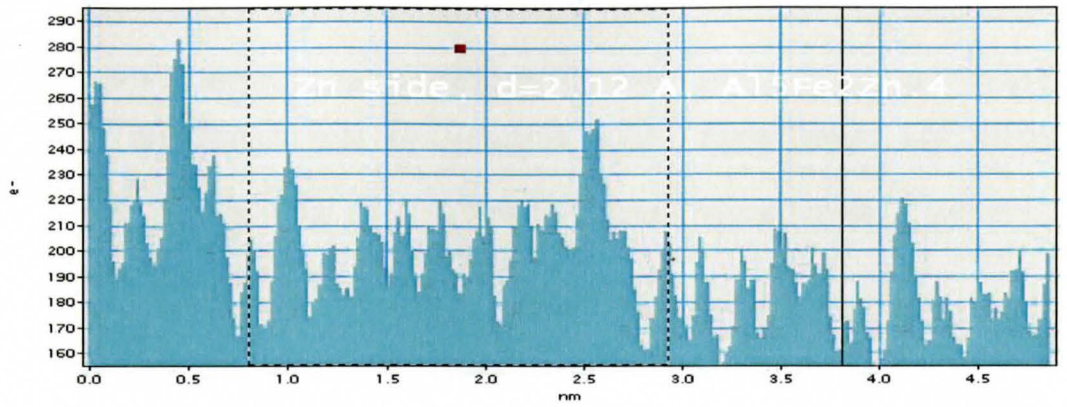

(a)

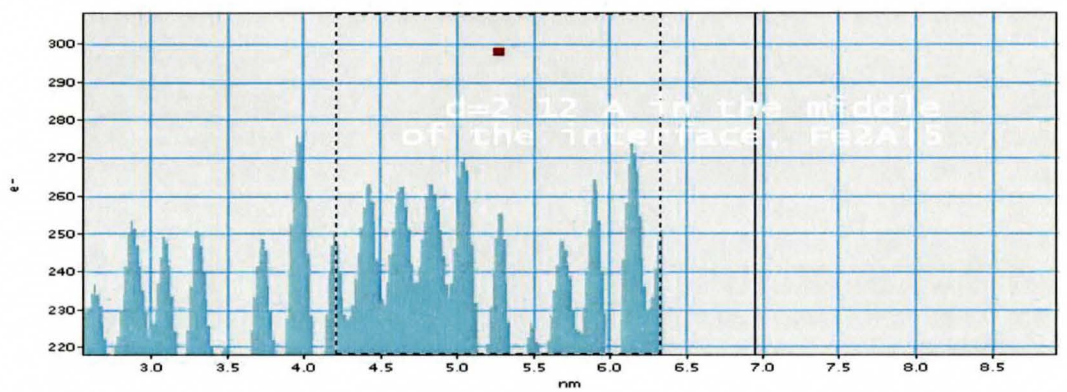

(b)

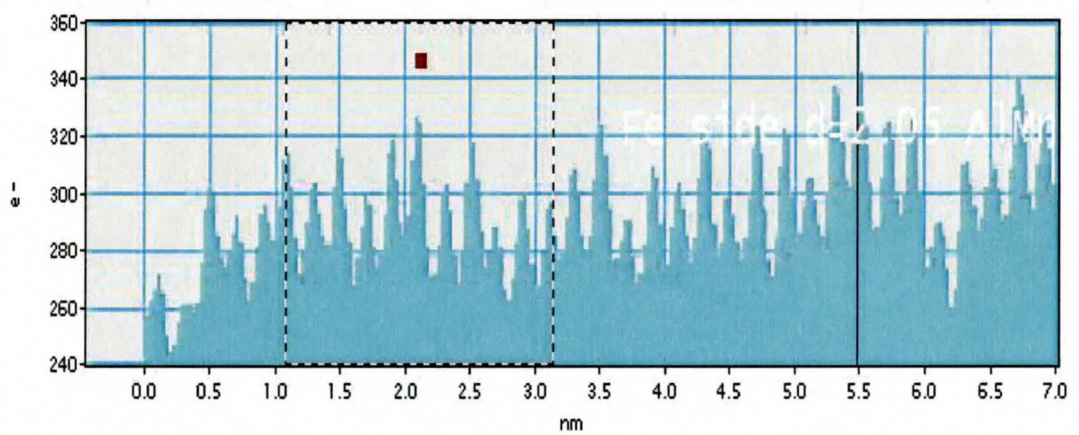

(c)

Figure 4.24: (a)'d' spacing = 2.12 A°, calculated from the zinc side of the interface. It corresponds to $Al_5Fe_2Zn_{0.4}$ [65], (b)'d' spacing = 2.12 A°, calculated from the middle of the interface. It corresponds to $Al_5Fe_2Zn_{0.4}$ crystal [65] or Fe_2Al_5 crystal [66] and (c)'d' spacing = 2.05 A°, calculated from the iron side of the interface. It corresponds to Al $Mn_{0.75}Fe_{2.25}$ crystal [67]

5. Discussion

The discussion chapter will consist of three sections. In the first section, the selective oxidation behaviour of the alloying elements in the experimental steel will be discussed. The classical Wagner selective oxidation model will be used to explain the results. It will be shown that the theoretical Wagner model can explain the oxidation behavior of Mn, the most important element in the experimental steel in this context. As predicted from the model, the experimental results showed selective external oxidation of Mn after annealing and before dipping the sample into the zinc bath. The distribution and chemical states of these oxides will be discussed in this section. The role of these oxides in the Zn bath will also be discussed. All of the above factors will be discussed as a function of the pre-dipping annealing cycle and the process atmospheres. In the second section, the quality of the coatings obtained with an emphasis on inhibition layer formation will be discussed. In the third section, a discussion of the structure of the interface will be discussed in the context of reactive wetting. Furthermore, it will be established that in-situ aluminothermic reduction of the surface Mn oxides in the galvanizing bath is the reactive wetting mechanism.

5.1 Behaviour of Steel Alloying Elements during Annealing

The effect of process atmosphere oxidation potential on the external-internal selective oxidation behaviour of solutes in the experimental DP steel was observed to determine an optimum annealing atmosphere. Initially, the objective was to promote

internal oxidation by increasing the oxidation potential of the annealing atmosphere and thus to find suitable process parameters for the CGL. It has already been established in the literature that promoting internal oxidation will improve the wettability [10]. The oxygen potential in the annealing atmosphere was increased through Figure 4.3 (b) to 4.3 (e) and the XPS depth profiling shows that Mn enrichment at the surface is decreased with an increase in oxidation potential. The profiles also show greater penetration of oxygen into the substrate material with increased oxidation potential, which indicates an increased tendency towards internal oxidation. This general trend is also supported by the GDOES observations shown in Figures 4.4 to 4.7. In particular, the Mn depth profiles obtained from Figure 4.4 to 4.7 show different selective oxidation behaviour in terms of internal and external oxidation. At relatively low oxygen potentials of the annealing atmosphere (Figure 4.4 and 4.5) only external oxidation of Mn occurred, whereas at higher oxygen potentials of the annealing atmosphere (Figure 4.6 and 4.7) internal oxidation along with external Mn oxidation was found.

Figure 5.1 (a) and (b) are drawn from the Figure 4.4 (f) through 4.7 (f) profiles to more closely examine this trend. The curves were drawn from the proposed schematic concentration profile for the internal oxidation of an A-B alloy by Rapp [33] which has been described earlier in Chapter 2.3.2.

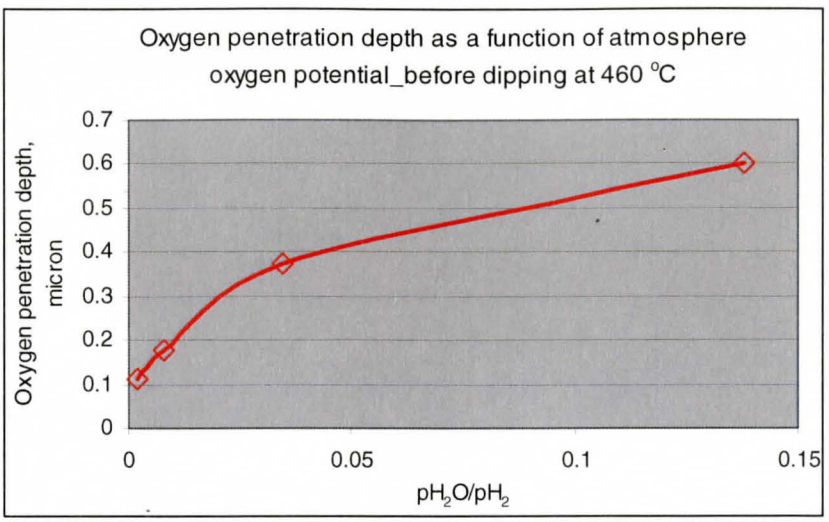

Figure 5.1 (a): Oxygen penetration depth as a function of oxygen potential of the annealing atmosphere.

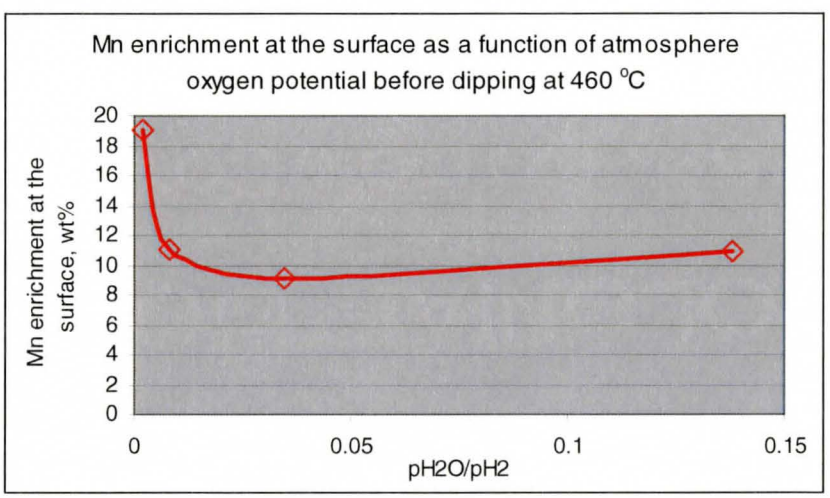

Figure 5.1 (b): Mn enrichment at the external surface as a function of oxygen potential of the annealing atmosphere.

In Figure 5.1 (a), one can clearly observe that the oxygen penetration depth has increased with increasing oxidation potential of the annealing atmosphere. Figure 5.1 (b) shows that there is a decreasing tendency for external Mn enrichment at the surface with

increasing oxidation potential. To explain the oxidation behavior of Mn, Wagner's selective oxidation model was exploited [33, 39, 52, 68]. Rapp [33] calculated the critical solute concentration to shift the oxidation mode from internal to external as a function of atmospheric oxidation potential. In the present research work, since the alloy composition is fixed, the only adjustable parameter in the model is N_O^S i.e., the mole fraction of oxygen at the external surface.

In its original version, the Wagner model can determine the critical molar fraction of the alloying element above which the selective oxidation will be external and below internal. In the present case, only Mn is considered for the modeling since it is alloying element which demonstrated the greatest degree of selective oxidation. The other major alloying element in the experimental steel is Mo. Mo is known not to segregate to the surface [10, 36, 59], as can be seen in Figures 4.8 and 4.9. Thus, Mo was not considered in the analysis.

The theoretical calculation of $N_{X,crit}^O$, which is the critical molar fraction of the alloying element to transition form external to internal oxidation, is given by the equation [7]:

$$N_{X,crit}^O = \left[\frac{\pi g^* V N_O^S D_O}{2nV_{XO_n} D_X} \right]^{1/2} \qquad (5.1)$$

Where, g* is the critical volume fraction of precipitated oxides required to block the inward diffusion paths for oxygen, n is the stoichiometric ratio between the oxygen and metal atoms in the oxide, V is the alloy molar volume, V_{XO_n} is the molar volume of

the oxide XO_n, N_O^S is the molar fraction of dissolved oxygen at the surface, D_O is the diffusion coefficient for oxygen given by:

$$D_O = D_O^{'} \exp[-Q_O / RT] \qquad (5.2)$$

Where, Q_O is the activation energy for oxygen in kJ / mol / K and T is the absolute temperature (in this case, the peak annealing temperature of 1073 K) and D_X is the diffusion coefficient of the alloying element, X, given by:

$$D_X = D_X^{'} \exp[-Q_X / RT] \qquad (5.3)$$

These values were determined for Mn from the literature for ferrite and austenite, such that:

g* = 0.3 [33]

n = 1 (i.e. MnO, from the XPS analysis which is shown in Figure 4.11 (a)-(d).

V_{MnO} = 13.221 [cm^3/mol] [69]

In ferrite:

V = 7.0918 [cm^3/mol] for ferrite [69],

$D_O^{'}$ = 0.00291 cm^2/s and Q_O = 89.5 kJ/mol [70]

$D_{Mn}^{'}$ = 1.49 cm^2/s and Q_{Mn} = 233.6 kJ/mol [71]

In austenite:

V = 7.299 [cm^3/mol] [72]

$D_O^{'}$ = 0.642 cm^2/s and Q_O = 159 kJ/mol [73]

$D_{Mn}^{'}$ = 0.16 cm^2/s and Q_{Mn} = 261.7 kJ/mol [71]

N_O^S was determined for the dew point and hydrogen contents in the experimental atmospheres using the equilibrium constant, K, determined by Swisher and Turkdogan for the reaction:

H_2 (g) + $O_{(\text{dissolved at the surface})}$ = H_2O (g) [74]

Where, the partial pressure of H_2O (g) is calculated from the thermodynamic data obtained from Fine and Geiger [75] and the value of N_O^S was obtained by equation 5.4 [74]:

$$N_O^S = (1/100).(56/16).(p_{H_2O} / p_{H_2}).(1/K) \qquad (5.4)$$

It should be noted that equation (5.1) was developed for a binary single crystal and therefore does not take into account grain boundary diffusion. $N_{X,crit}^O$ can also be calculated for grain boundary oxidation by dividing the diffusion coefficient and the activation energy by two and, therefore, the Wagner model for the transition between internal and external oxidation of grain boundaries is given by [39]:

$$N_{X,crit,GB}^O = \left[\frac{\pi g^* V N_O^S D_O' \exp(-Q_O/2RT)}{2nV_{XOn} D_X' \exp(-Q_X/2RT)}\right]^{1/2} \qquad (5.5)$$

In the present case, however, as the bulk composition of the steel is kept constant, the results of the calculation for $N_{X,crit}^O$ in the bulk alloy and at the grain boundaries are used to predict whether the investigated steel would be oxidized externally or internally under the experimental annealing atmospheres. These results are shown graphically in Figure 5.3 and in tabular form in Table 5.1.

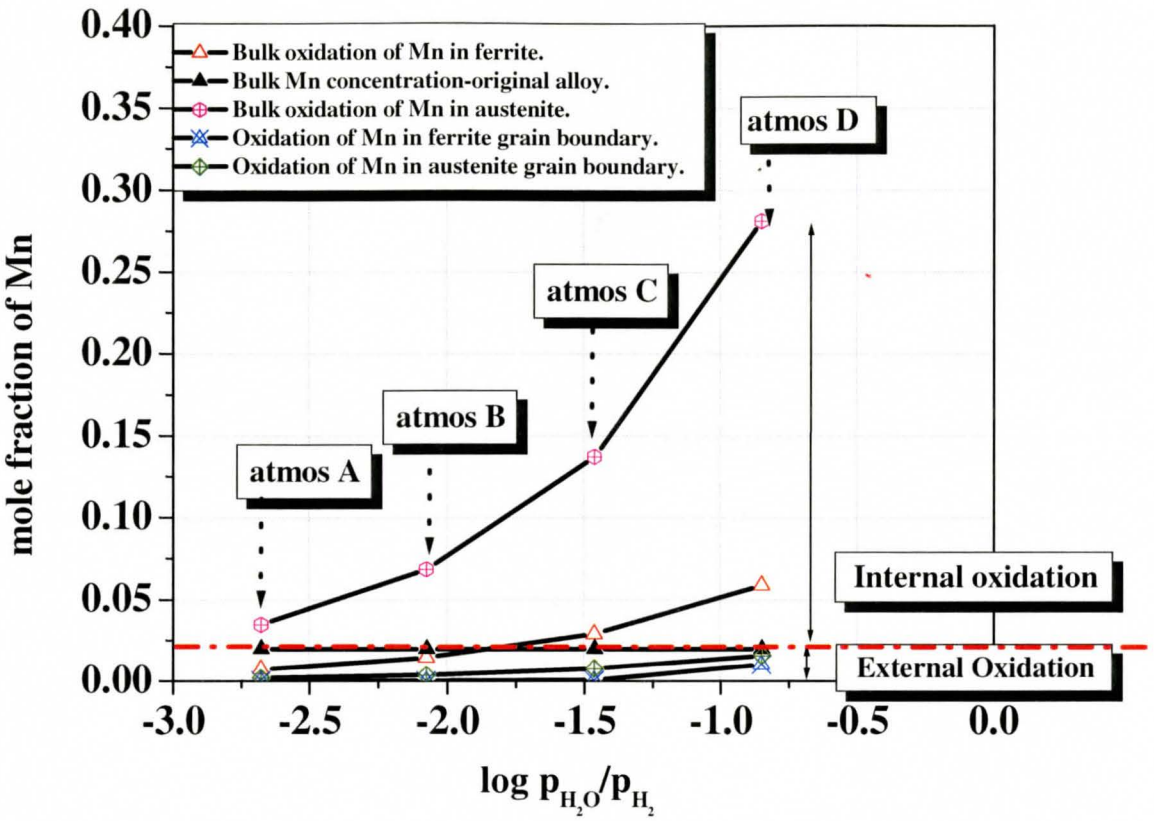

Figure 5.2: Theoretical prediction for internal / external oxidation of Mn at the peak annealing temperature (800 °C) in accordance with the Wagner oxidation model.

It should be mentioned that there are some limitations to using the Wagner model for commercial steels. It should be noted that this model was developed for a single crystal binary alloy and that the influence of the other alloying elements present in the steel is not accounted for. Furthermore, there are some uncertainties associated with a number of the parameters used in the calculations, possibly leading to a large accumulated overall uncertainty [39]. Among the above uncertainties are such factors as

non-stoichiometric compound formation, spinel formation, and the effect of stress due to volume change and the possibility of having some volatile species. As we have considered the present DP steel to be a dilute Fe-Mn alloy and ignored all other elements to calculate the selective oxidation behavior of Mn, it should be noted that this assumption may also introduce a bias into the analysis. Also, similarities between the Fe and Mn atom and the similar growth rate of FeO and MnO may again cause selective diffusion behaviour changes [50].

Table 5.1: Theoretical prediction for internal / external oxidation of Mn in the experimental DP steel at the peak annealing temperature (800 °C) in accordance with the Wagner oxidation model.

	Bulk Oxidation		**Grain Boundary Oxidation**	
Atmosphere Designation	N_{crit} Ferrite	N_{crit} Austenite	N_{crit} Ferrite	N_{crit} Austenite
A (pH_2O/pH_2=0.00211)	External	Internal	External	External
B (pH_2O/pH_2=0.00844)	External	Internal	External	External
C (pH_2O/pH_2=0.03451)	Internal	Internal	External	External
D (pH_2O/pH_2=0.14180)	Internal	Internal	External	External

Keeping mind of all the above mentioned limitations, it can be observed from the Figure 5.2 and Table 5.2 that the model predictions for bulk ferrite (the major phase in

the experimental material) are in good agreement with the experimental observations in that the investigated steel oxidizes only externally under atmospheres A and B (A: pH_2O/pH_2=0.00211, Figure 4.4; B: pH_2O/pH_2=0.00844, Figure 4.5) and internally under atmospheres C and D (C: pH_2O/pH_2=0.03451, Figure 4.6; D: pH_2O/pH_2=0.14180, Figure 4.7). The grain boundaries, on the other hand, are externally oxidized for all of the investigated annealing atmospheres, which are consistent with the SEM observations in Figure 4.14, which showed the preferential grain boundary oxides of MnO at the grain boundaries, as predicted by the model. From the above discussion we can conclude that the classical Wagner selective oxidation model can provide useful information about the transition between external-internal oxidation of these relatively simple dual-phase alloys in the present experimental atmospheres.

5.2 Coating Characterization

The XPS spectra shown in Figures 4.11 (a) – (d), elemental depth profile of Figure 4.3 (b) – (e) and GDOES observations in Figures 4.4 – 4.7 show the presence of MnO at the external surface and which can not be reduced under standard industrial annealing atmospheres [45, 46, 76, 77]. Mn oxides at the surface prior to dipping should prevent proper reactive wetting and formation of a well developed Fe_2Al_5 layer by preventing reaction between the steel substrate and the Al resident in the Zn bath. This is obviously not the case, as can be seen from the general observation of the coating chemistry and inhibition layer shown in Figures 4.15(a) – (d) and 4.18 (a) – (d).

Although there were a few bare spots in 4.15 (a) parallel to the rolling direction, we may ignore these as local surface defects as evidenced in Figure 4.13. There was a fully developed Fe_2Al_5 layer and this is shown by the SEM micrograph in Figure 4.18 (a) – (d) and supported by the GDOES profiles of the coating shown in Figure 4.17 (a) – (d). The coatings showed good adhesion which is seen in Figure 4.16 and is the further evidence that Fe_2Al_5 layer has been formed. These observations are consistent with the literature in that steels with 1.5 wt% Mn can be properly galvanized and give rise to the formation of a well developed inhibition layer [51, 78, 79]. It is common for 1.5 wt% Mn alloys to be successfully galvanized, but the reactive wetting mechanism has not been detailed or physical evidence of the industrial reaction mechanism found in the literature.

5.3 Mechanism of Reactive Wetting and Aluminothermic Reaction of Mn Oxides

All of the above results imply that there was likely reactive wetting between the steel substrate and liquid Zn bath. The change in the Mn depth profile prior and after dipping the samples into the Zn bath can be compared by GDOES observation between Figures 4.4 (f) – 4.7(f) and 4.17 (a) – (d). The change in Mn profile was further confirmed by stripping the Zn coating and analyzing the surface which is shown in Figure 4.19 (a) – (d). The comparison of these results certainly shows that there was physical removal of the oxide film during the dipping process, as evidenced by the TEM work in Chapter 4.5.3. These observations can be explained by the process of aluminothermic reduction of the surface Mn oxides by the Al resident in the Zn bath.

Dubois [80] showed the presence of Mn in the Zn bath following a campaign of galvanizing of Mn steels in the industrial setting. Recently, a thermodynamic model of the zinc rich corner of the Zn-Al-Fe phase system was proposed by Kaye et al. [31], including externally validated Al activity data for the Zn bath. Using this Al activity data, it can be determined whether or not Al in the bath can reduce the observed MnO film on the steel substrate as per the reaction:

$$3MnO_{(solid)} + 2Al_{(solution)} \xrightarrow{460^0 C} Al_2O_{3(solid)} + 3Mn_{(solution)} \qquad (5.6)$$

Considering the relative amounts of the MnO film and the Zn (Al, Fe) bath, there will be a large excess of bath metal in the galvanizing bath available to react with the MnO film. This result of a Gibbs Energy minimization for the above reaction between a Zn (Al, Fe) bath and MnO film on the steel strip, calculated [81]using the Facility for the Analysis of Chemical Thermodynamics (F.A.C.T) [82], are shown in Table 5.2 and steps followed (by F.A.C.T.) for the above calculations are given below:

Table 5.2: Thermodynamic calculation of the reduction of MnO by a 0.2 wt% Al and 0.02 wt% Fe in a galvanizing bath [81].

Input data: 99.780g Zn + 0.0200g Al + 0.02g Fe + 0.00002g MnO						
Phases	**Liquid bath**		**Dross**		**Oxide**	
Calculated wt for each phase (g)	99.976		0.24104E-01		0.95823E-5	
Physical state	Liquid		Solid		Solid	
Composition (wt%)	Zn	99.799	Fe_2Al_5	80.257		
	Al	0.18946	Zn	19.743	Al_2O_3	0.95823E-05
	Fe	0.11241E-01				
	Mn	0.15493E-04				

Steps of calculation (done by FACT):

1. Generation of equilibrium phase diagram from the input data.
2. Identifications of phases from equilibrium phase diagram and calculation of their compositions by using the lever rule.
3. Mass balance to calculate the composition of phases or elements to determine the system equilibrium compositions when activity of Al_2O_3 is 1. During this stage repeated iterations has been performed by the software to arrive at the proper configuration. Here the final solution was obtained with the help of phase diagram and free energy equations and the iterations were continued till the activity of the Al_2O_3 converged to 1.
4. At this stage equations (5.6) can be applied to calculate the activity of Al to reduced MnO, where it has been assumed that Al_2O_3 is formed due to the reduction MnO by Al.

This Gibbs Energy minimization also determined that the Al activity required to reduce the MnO film was $a_{Al} = 2.9069 \times 10^{-16}$; this is considerably lower than that the activity of Al in the Zn (Al, Fe) bath that was calculated using the thermodynamic model of Kaye et al. [31] where $a_{Al} = 0.024192$. As a consequence, direct contact is possible between the steel substrate and the Zn bath, allowing the formation of a well developed inhibition layer and accounting for experimentally observed interfacial structures. It also

explains the alteration of the Mn profile between Figure 4.4 (f) – 4.7 (f) and Figure 4.19 (a) – (d).

The elemental composition profiles measured in the TEM (Figure 4.20) bring further support for this hypothesis. Indeed, it can be seen that the Mn profile [Figure 4.21 (d)] exhibits only a few very small peaks that are localized in the steel substrate, while the O profile is very low through all the analyzed line. The O profile [Figure 4.21 (e)] shows a sharp decrease after 400 nm where the inhibition layer starts. The presence of inhibition layer can be observed from the Al profile [Figure 4.21 (a)]. This gives further evidence that a reactive wetting process took place between the steel substrate and the Zn bath, involving the aluminothermic reduction of Mn oxides and the dissolution of Mn into the bath, followed by the formation a well developed inhibition layer and the formation of high quality, adherent coatings. HRTEM analysis was further carried out to support this idea. Lattice fringe pattern obtained from HRTEM confirmed the presence of Fe_2Al_5 layer in the interface [65, 66] which is shown in Figure 4.24 (a) and (b). The lattice fringe pattern patterns also shows the presence of $AlMn_{0.75}Fe_{2.25}$ crystals [67] is as shown in Figure 4.24 (c).

6. Conclusions and Recommendations for Future Work

The purpose of the project was to study the evolution of surface morphology, including selective oxidation as a function of annealing atmosphere and determine the effect, if any, on reactive wetting, the formation of galvanized inhibition layer on an 2.0 wt % Mn dual phase steel.

6.1 Conclusions

1. Selective oxidation of Mn in the experimental DP 600 steel is a strong function of the oxidation potential of the annealing atmosphere.
2. A certain amount of Mn enrichment at the steel surface is unavoidable for all four experimental annealing atmospheres (i.e., pH_2O/pH_2 ratio of 0.00211 to 0.14180).
3. With increasing oxidation potential of the annealing atmosphere (i.e., pH_2O/pH_2 ratio of 0.00211 to 0.14180) the internal oxidation thickness increases (from 0.1 micron to 0.6 micron) and the external Mn segregation decreases (from 19 wt % to 09 wt %). A transition from external to internal occurs when the oxidation potential of the atmosphere increases from a pH_2O/pH_2 ratio of 0.00844 to a pH_2O/pH_2 ratio of 0.03451.
4. The selective oxidation of Mn is consistent with the Wagner classical oxidation model.
5. Mo does not show selective oxidation in the experimental alloy system.

6. All experimental atmospheres are capable of producing good galvanized coatings despite the presence of 9-19 wt% Mn segregation at the external surface as MnO. The coatings exhibit good coating adhesion and a well developed inhibition layer for all experimental annealing atmospheres due to reactive wetting.
7. Reactive wetting occurs in the Zn bath and for this reason the external MnO was reduced by the resident Al in the galvanizing bath via an aluminothermic reduction mechanism.

6.2 Recommendations for Future Work

1. Optimization of the thermal cycle to optimize the DP steel mechanical properties.
2. Explore the oxidation behavior of higher Mn content alloys to determine if there is a maximum alloy Mn content for which the aluminothermic reduction / reactive wetting mechanism is still operative.
3. Observe the reactive wetting in the Zn bath by contact angle measurement via the Welhelmy plate method.
4. Perform a detailed characterization of coating quality with reference to those steels which are well established as being galvanizable (e.g. IF steel).
5. Explore the Galvannealing of DP steels.
6. Measure the oxidation kinetics of DP steels at various stages of the annealing cycle with the objective of optimizing the oxidation potential of the annealing atmosphere i.e. to explore the benefits of oxidation-reduction or related techniques.

References

[1] B. Mintz, Intl. Mater. Rev., vol. 46, no. 4, 2001, p.169

[2] ULSAB-AVC Program, "Technical Transfer Dispatch #6", ULSAB-AVC Body Structures Materials, ULSAB-AVC Consortium, May 26, 2001, p.2

[3] H. Shirasawa, Y. Tanaka, M. Miyahara and Y. Baba, Transactions ISIJ, vol. 26, 1986, p. 310

[4] H. Sekine, Transactions ISIJ, vol. 25, 1985, p. 839

[5] A. R. Marder, Progr. Mater. Sci., vol. 45, 2000, p.191

[6] C. Wagner, J. Electrochem. Soc., vol. 99, 1952, p. 369

[7] C. Wagner, J. Electrochem. Soc., vol.103, 1956, p. 627

[8] C. Wagner, Z Elektrochem., vol. 63, 1959, p. 773

[9] I. Olefjord, W. Leijon and U. Jelvestam, Applied Surface Science, vol. 6, 1980, p. 241

[10] R. Bode, M. Meurer, T. W. Schaumann, W. Warnecke, 'Selection and Use of Coated Advanced High-Strength Steels for Automotive Applications', Conference Proceedings Galvatech, 2004, p. 107

[11] S. Frenznick, M. Stratmann, M. Rohwerder, 'Galvanizing of Defined Model Samples: On the Road to a Fundamental Physical Understanding of Hot-dip Galvanizing', Conference Proceedings Galvatech, 2004, p. 411

[12] J. R. Shaw, B. K. Zuidema, SAE Transactions: Journal of Materials & Manufacturing (USA), vol. 110, 2001, p. 976

[13] M. F. Shi, G. H. Thomas, M. X. Chen and J. R. Fekete, 'Formability Performance Comparison Between Dual Phase and HSLA Steels', Iron and Steelmaker (USA), vol. 29, no. 3, 2002, p. 27

[14] K. Hulka, Mater. Sci. Forum, vols. 414-415, 2003, p. 101

[15] C.L. Magee, SAE Reprint 820147, 1982.

[16] H. K. D. H. Bhadeshia and D. V. Edmonds: Met. Sci., vol. 14, 1980, p. 41

[17] H. K. D. H. Bhadeshia, ISIJ International, vol. 42, no. 9, 2002, p. 1059

[18] R.O. Rocha, T.M.F. Melo, E.V. Pereloma, D.B. Santos, Mater. Sci. Engng. A, vol. 391, 2005, p. 296

[19] T. Ohtsubo, Bull. Japan Inst. Metals, vol. 21, 1982, p. 529

[20] T. Sendzmier, U.S. Patent No. 2,110.893, 1938

[21] T. Le and M. Gagne, 'Materials Balance in the Zn bath at Dofasco No. 4 CGL', 5 th International conference on Zn and Zn alloy coated Steel Sheet, CRM, Galvatech 2001, p. 533

[22] C. E. Jordan, A. R. Marder, J Mater. Sci, vol. 32, 1997, p. 5593

[23] C. E. Jordan, A. R. Marder, J Mater Sci, vol. 32, 1997, p. 5603

[24] M. Guttman, Mater. Sci. Forum, vol.155–156, 1994, p. 527

[25] P. Perrot, J. C. Tissier and J. Y. Dauphin, Z. Metallk., vol. 83, 1992, p. 786

[26] Z.W. Chen, R.M. Sharp and J. T. Gregory, Mater. Sci. Technol., vol. 6, 1990, p. 1173

[27] S.E. Price, 'Formation and development of aluminum inhibition layers during galvanizing/galvannealing', La Revue de Metallurgie-CIT, Mars 1999, p. 381

[28] N Tang, Modelling of enrichment in galvanized coatings, Met. Mater. Trans, vol. 26A, 1995, p.1669.

[29] E. Baril and G. L'esperance, Met. Mater. Trans A, vol. 30A, 1999, p. 681

[30] N. Tang and G. R. Adams, The Physical Metallurgy of Zinc Coated Steel, San Francisco, CA, TMS, Warrendale, PA, 1994, p. 41

[31] M.H. Kaye, W.T. Thompson, J.R. McDermid, 'The Zn-rich corner of the Zn-Al-Fe Phase Diagram for Use in Continuous Galvanizing', Materials Science and Technology, Pittsburgh, Pennsylvania, 2005, p. 199

[32] P. Kofstad, High Temperature Oxidation of Metals, John Willey & Sons, Inc., 1966, p. 113

[33] R. A. Rapp, Kinetics, 'Microstructure and Mechanism of Internal Oxidation-Its effect and Prevention in High Temperature Alloy Oxidation', Corrosion, National, Association of Corrosion Engineers, vol. 21, 1965, p. 382

[34] N. Birks and G H Meier, Introduction to High Temperature Oxidation of Metals, Publisher: Edward Arnold, London, 1983, p. 104

[35] D. R. Gaskel, Introduction to the Thermodynamics of Materials, Fourth Ed., Publisher Taylor & Francis, 2003, p. 359 (based on F. D. Richardson and J. H. E. Jeffes, Iron and Steel Inst., Vol.163, 1949, pp. 397-420 and Vol. 171, 1952, pp. 165-175)

[36] R. Rapp. Trans. Amer. Inst. Min. (Metall.) Engrs., vol. 227, 1963, p. 371

[37] T. Ichida: in International Galvatech '95, Warrendale, PA, ISS , 1995, p.359

[38] C. Flinchim et al.: 'Method of coating low alloy steels', US Patent 3,925,579, 1975

[39] J.M. Mataigne, M. Lamberigts, V. Leroy, Selective Oxidation of Cold- Rolled Steel During Recrystallization annealing, Developments in the Annealing of Sheet Steels: proceedings of an International Symposium by the TMS Ferrous Metallurgy Committee and held at the 1991 Fall Meeting in Cincinnati, Ohio, October 22-24, R. Pradhan and I.Gupta (Eds), 1992, p. 511

[40] P. Drillet, Z. Zermout, D. Bouleau, J.M. Mataigne, 'Selective oxidation of IFTi stabilized steels during recrystallization annealing, and steel/Zn reactivity', Proc. of Galvatech, 2001, p. 195

[41] X. Vanden Eynde, J. P. Servais, M. Lamberigts, Surface and Interface Analysis, vol. 35, 2003, p. 1004

[42] I. Hertveld, S. Claessens, B.C. De Cooman, Met. Sci. Tech., vol. 17, 2001, p. 1508

[43] J. Mahieu, S. Claessens, B.C. De Cooman, Met. Mat. Trans. A, vol. 32A, 2001, p. 2905

[44] X. V. Eynde, J.P. Servais and M. Lamberigts, 'Surface oxide maturation and self-reduction: a new process to ensure TRIP steel hot dip galvanizing', Conference Proceedings Galvatech '04, 2004, p. 361

[45] P. Drillet, Z. Zermout, D. Bouleau, J.Mataigne, S.Claessens, 'Selective oxidation of high Si, Mn and Al steel grade during Recrystallization Annealing, and Steel/Zn reactivity', Galvatech, 2004, Chicago, IL, p. 1123

[46] J. Mahieu, S. Claessens, B.C. De Cooman, F. Goodwin, 'Surface and Sub-surface Characterization of Si-, Al- and P-alloyed TRIP-aided Steel', Galvatech, 2004, Chicago, IL, 2004, p. 529

[47] W. Black and D. Beste, Conference Proceedings Galvatech, 2004, p. 359

[48] L. Zhang and T. R. Bensinger, Conference proceedings Galvatech '95, Warrendale, PA, ISS., 1995, p. 115

[49] J. Yoon and S. Jang, Proc. 19th ATS Journe'es Siderurgique, Paris, France, 1988; Rev. Metall., to be published

[50] L. Shi, 'On the Possibility of Improving Hot-dip Galvanisability of Steels Strengthened with Mn through Pre-oxidation', Galvatech Conference Proceedings, 2004, p. 242

[51] J. Maki, J. Mahieu, S. Claessens and B.C. De Cooman, Hot-dip Galvanising of Si-free CMnAl-TRIP Steels, 5th International Conference on Zinc and Zinc Alloy Coated Steel Sheet, Galvatech, 2001, p. 623

[52] H. J. Grabke, V. Leroy and H. Viefhaus, ISIJ International, vol. 35, no. 2, 1995, p. 95

[53] R. Asthana and N. Sobczak, 'Wettability, Spreading, and, Interfacial Phenomena in High-Temperature Coatings', JOM-e, 52 (1), 2000

[54] Reference for dynamic wetting, url: www.kvinc.com/wilhelmy_plate.htm, downloaded on April 30, 2006

[55] R. Avtar, B.K. Jha, A. Saxena, V. S. Dwivedi, B.B. Patnaik, B. Banerjee and S. Srinivasan, Transactions ISIJ, vol. 26, 1986, p. 822

[56] B. Chapman, Glow Discharge Process, John Willey, New York, 1980, pp 44, 77-79, 115-132.

[57] R. Payling, Mater. Forum, vol.18, 1994, p. 200

[58] R. Playing, D. G. Jones and S. A. Gower, Surf. Interf. Anal., vol.20, 1993, p. 959

[59] J. Chipman, Pure and Appl. Chem., vol. 5, 1962, p. 361

[60] H. K. Hu, J. W. Rabalais, Surf. Sci., vol. 107, 1981, p. 376

[61] B. R. Strohmeier, D. M. Hercules, J. Phys. Chem., vol. 88, 1984, p. 4922

[62] B. N. Ivanov- Emin, N. A. Nevskaya, B. E. Zaitsev and T. M. Ivanova, Zh. Neorg. Khimii, vol. 27, 1982, p. 3101

[63] H. Konno, M. Nagayama, J. Electron Spectrosc., Relat. Phenom., vol. 18, 1980, p. 341

[64] E. Paparazzo, J. Phys., vol. D. 20, 1987, p. 1091

[65] Z. Chen, J. Gregory, R. Sharp, Metall. Trans. A, vol. 23, 1993, p. 2393

[66] M. Ellner, J., Scripta Metall. Mater., vol.26, 1992, p. 501

[67] A. S. Ilyushin, W. E. Wallace, J. Solid State Chem., vol.17, 1976, p. 385

[68] A.S. Khanna, 'Introduction to High Temperature Oxidation and Corrosion', ASM International, Materials Park, OH, 2002

[69] R. C. Weast, Editor. CRC Handbook of Chemistry and Physics.59th Ed., CRC Press Inc., West Palm Beach, Florida, 1978

[70] J. Takada, M. Adachi, J. Mater. Sci., vol. 21, 1986, p. 2133

[71] S. Sun and M. Pugh, Mater. Sci. Engng. A, vol. 276, 2000, p. 167

[72] D. R. Lide, Editor. CRC Handbook of Chemistry and Physics, 83rdEd, CRC Press, Inc.: Boca Raton, Florida, 2002

[73] J. Takada, K. Kashiwagi and M. Adachi, J. Mater. Sci., vol.19, 1984, p. 3451

[74] J. H. Swisher, E. T. Turkdogan, Trans. Metall. Soc. AIME, vol. 239, 1967, p. 426

[75] H. A. Fine and G. H. Geiger, Handbook on Material and Energy Balance Calculations in Metallurgical Processes, The Metallurgical Society of AIME, Warrendale, Pennsylvania (Pa), 1979

[76] D. Loison, D. Huin, V. Lanteri, J.P. Servais, R. Cremier, 'Selective oxidation of Fe-Mn alloys: surface characterization and modelling', Galvatech'01, Brussels, Belgium, 2001, p. 203

[77] I. Parezanovic, M. Spiegel, 'Influence of B, S, P, Si and C Segregation on the Selective Oxidation of Dual-Phase and Interstitial Free Steels', Galvatech'04, Chicago, IL, 2004, p. 401

[78] E.M. Bellhouse, A.I.M. Mertens and J.R. McDermid, 'Development of the Surface Structure of TRIP Steels Prior to Hot-Dip Galvanizing', submitted for publication in the Proceedings for the Mukherjee Symposium, TMS 2006, San Antonio, TX, 2006

[79] J. Mahieu, S. Claessens, B.C. De Cooman, 'Influence of the surface state of TRIP steels on their galvanizability', Galvatech'01, Brussels, Belgium, 2001, p. 644

[80] M. Dubois, 'Mn in the galvanised coating', Zn-based Steel Coating Systems: Production and Performance, Proceedings at the International Symposium held at the TMS annual meeting, San Antonio, TX, 1998, p. 39

[81] M. H. Kaye, private communication, Royal Military College of Canada, Kingston, Ontario, Canada, 2006

[82] C.W. Bale, A.D. Pelton, W.T. Thompson. Facility for the Analysis of chemical Thermodynamics (F.A.C.T.), Ecole Polytechnique de Montreal, Montreal, Canada, 2002